



HAL
open science

A mid-infrared imaging catalogue of post-asymptotic giant branch stars

Eric Lagadec, T. Verhoelst, D. Mékarnia, O. Suárez, A. Zijlstra, P. Bendjoya, R. Szczerba, O. Chesneau, H. van Winckel, M. Barlow, et al.

► **To cite this version:**

Eric Lagadec, T. Verhoelst, D. Mékarnia, O. Suárez, A. Zijlstra, et al.. A mid-infrared imaging catalogue of post-asymptotic giant branch stars. *Monthly Notices of the Royal Astronomical Society*, 2011, 417, Issue 1, pp.32-92. 10.1111/j.1365-2966.2011.18557.x . hal-00722178

HAL Id: hal-00722178

<https://hal.science/hal-00722178>

Submitted on 30 Nov 2021

HAL is a multi-disciplinary open access archive for the deposit and dissemination of scientific research documents, whether they are published or not. The documents may come from teaching and research institutions in France or abroad, or from public or private research centers.

L'archive ouverte pluridisciplinaire **HAL**, est destinée au dépôt et à la diffusion de documents scientifiques de niveau recherche, publiés ou non, émanant des établissements d'enseignement et de recherche français ou étrangers, des laboratoires publics ou privés.



Distributed under a Creative Commons Attribution 4.0 International License

A mid-infrared imaging catalogue of post-asymptotic giant branch stars[★]

Eric Lagadec,^{1†} Tijl Verhoelst,² Djamel Mékarnia,³ Olga Suárez,^{3,4} Albert A. Zijlstra,⁵ Philippe Bendjoya,³ Ryszard Szczerba,⁶ Olivier Chesneau,³ Hans Van Winckel,² Michael J. Barlow,⁷ Mikako Matsuura,^{7,8} Janet E. Bowey,⁷ Silvia Lorenz-Martins⁹ and Tim Gledhill¹⁰

¹European Southern Observatory, Karl Schwarzschildstrasse 2, Garching 85748, Germany

²Instituut voor Sterrenkunde, Katholieke Universiteit Leuven, Celestijnenlaan 200D, 3001 Leuven, Belgium

³Laboratoire Fizeau, OCA/UNS/CNRS UMR6525, 06304 Nice Cedex 4, France

⁴Instituto de Astrofísica de Andalucía, CSIC, Apartado 3004, 18080 Granada, Spain

⁵Jodrell Bank Centre for Astrophysics, School of Physics & Astronomy, University of Manchester, Oxford Road, Manchester M13 9PL

⁶N. Copernicus Astronomical Center, Rabianska 8, 87-100 Torun, Poland

⁷Department of Physics and Astronomy, University College London, Gower Street, London WC1E 6BT

⁸Mullard Space Science Laboratory, University College London, Holmbury St Mary, Dorking, Surrey RH5 6NT

⁹Observatorio do Valongo, UFRJ, Ladeira do Pedro Antonio 43, 20080-090 Saude, Rio de Janeiro, Brazil

¹⁰Science and Technology Research Institute, University of Hertfordshire, College Lane, Hatfield AL10 9AB

Accepted 2011 February 17. Received 2011 February 9; in original form 2010 December 10

ABSTRACT

Post-asymptotic giant branch (post-AGB) stars are key objects for the study of the dramatic morphological changes of low- to intermediate-mass stars on their evolution from the AGB towards the planetary nebula stage. There is growing evidence that binary interaction processes may very well have a determining role in the shaping process of many objects, but so far direct evidence is still weak. We aim at a systematic study of the dust distribution around a large sample of post-AGB stars as a probe of the symmetry breaking in the nebulae around these systems. We used imaging in the mid-infrared to study the inner part of these evolved stars to probe direct emission from dusty structures in the core of post-AGB stars in order to better understand their shaping mechanisms. We imaged a sample of 93 evolved stars and nebulae in the mid-infrared using VLT spectrometer and imager for the mid-infrared (VISIR)/VLT, T-Recs/Gemini-South and Michelle/Gemini-North. We found that all the proto-planetary nebulae we resolved show a clear departure from spherical symmetry. 59 out of the 93 observed targets appear to be non-resolved. The resolved targets can be divided into two categories. (i) The nebulae with a dense central core, that are either bipolar and multipolar and (ii) the nebulae with no central core, with an elliptical morphology. The dense central torus observed likely hosts binary systems which triggered fast outflows that shaped the nebulae.

Key words: circumstellar matter – infrared: stars.

1 INTRODUCTION

According to our current understanding of stellar evolution, all stars with main-sequence mass in the range $1\text{--}8M_{\odot}$ evolve via the asymptotic giant branch (AGB) phase to the planetary nebula (PN) stage. As they ascend the AGB, their mass-loss rate increases from solar-like values ($10^{-14}M_{\odot}\text{yr}^{-1}$) to $10^{-4}M_{\odot}\text{yr}^{-1}$. This mass loss

is an essential component of galactic evolution, as these are the main sources of s-process elements in the Universe (Gustafsson & Ryde 1996) and are the main producers of carbon. AGB stars are also the main contributors to the dust phase of the interstellar medium, which is important for the energy balance in Galaxies. During the last stages of the AGB, the remains of the convective hydrogen envelope are ejected during final violent and sporadic mass-loss events. Dust grains and molecules, predominantly CO, condense in their winds, forming substantial circumstellar envelopes detectable in the infrared and millimetric domains.

A departure from spherically symmetric mass-loss is observed in a substantial fraction of suspected transition objects. In particular,

[★]Based on observations made at the Very Large Telescope at Paranal Observatory under the programme 081D.0630.

†E-mail: elagadec@eso.org

multipolar structures are often associated with proto-planetary nebulae (PPNe) sources (Sahai 2002). The observed morphology of these objects is projected on the sky, making it difficult to know what is the intrinsic morphology of PPNe and PNe. But it is estimated that around 80 per cent of all PNe show aspherical morphologies (e.g. Machado 1997). *Hubble Space Telescope (HST)* observations of PNe, for example, show a large range of morphologies, including elliptical, bipolar, multipolar or round nebulae (e.g. Sahai & Trauger 1998). Hydrodynamical models explain many of the observed structures from a structure-magnification mechanism, where a fast wind from the central star of the PN ploughs into the earlier slow AGB wind (Kwok, Purton & Fitzgerald 1978), amplifying any density asymmetry already present (Balick, Preston & Icke 1987; Frank & Mellema 1994): the Generalized Interacting Stellar Wind model or GISW. Another model has also been proposed by Sahai & Trauger (1998) to explain the shaping of PNe. In their model the shaping of the PNe occurs at the end of the AGB phase when fast collimated jets are triggered and shape a bipolar nebula. If the direction of the jets changes with time, then multipolar nebulae can be formed. Such jets could be formed through interaction with a companion, e.g. in an accretion disc (for a review see Balick & Frank 2002).

Much of PN and PPN shaping theory relies on the presence of circumstellar material in either a dusty torus or disc. Our team has discovered some discs/tori in the heart of PNe (Lagadec et al. 2006; Chesneau et al. 2006; Matsuura et al. 2006; Chesneau et al. 2007) using adaptive optics on the Very Large Telescope (VLT) and mid-infrared interferometry at the Very Large Telescope Interferometer (VLTI). But the role of these discs/tori for the shaping of the nebula is still unclear as we do not know which fraction of the total dusty mass is present in these central cores, nor the fraction of objects exhibiting such a disc/torus.

These equatorial structures are likely due to the interaction of the central star with a binary companion. But observation wise, there are yet no strong direct observational evidence for this in the PPN phase (Hrivnak et al. 2010). Miszalski et al. (2009, 2011) discovered some central binary systems in PNe, but no clear connection between the binaries and morphological class. Some binary post-AGB stars are known and they have very compact discs, not resolvable with direct imaging but only with interferometry. These discs are likely Keplerian and the binary orbits revealed so far indicate that strong interaction must have taken place on the AGB or even RGB. The spectral energy distributions (SEDs) of these objects are specific, and RV Tauri stars with dust are mainly found in this category [see e.g. Deroo et al. (2006) for the interferometry; De Ruyter et al. (2006) for the SED; Van Winckel et al. (2009) for the binarity; De Ruyter et al. (2005) and Gielen et al. 2009 for the RV Tauri stars].

To observe the inner part of post-AGB stars, we need mid-infrared observations, as the dust optical depth is smaller at longer wavelengths. Mid-infrared is indeed the only wavelengths range at which we can observe the inner morphology of stars from the AGB to the PPN phase. Furthermore, the main source of radiation for these sources in the mid-infrared is direct emission from dust, while at shorter wavelengths this is scattered light. Mid-infrared imaging is thus the best way to study the dusty structures inside these evolved stars.

Many mid-infrared imaging observations of AGB and PPNe have been made in the past. But the only mid-infrared imaging survey has been made with 3-m class telescopes (Meixner et al. 1999) and present a lack of angular resolution for the morphological study of the observed objects, a selection bias as they observed known bipolar nebulae and consists of only 17 resolved sources. Some work

has been done using 8-m class telescopes, but always focusing on particular individual bright well-known objects (e.g. Miyata et al. 2004).

We observed 86 evolved stars (two observed twice, using different modes) using VISIR at the VLT, five using T-Recs (two also observed with VISIR) on *Gemini-South* and five using Michelle (one also observed with VISIR) on *Gemini-North*. Taking into account that some objects were observed twice with different instrument, our total list of targets includes 93 objects. Here we present this mid-infrared *N*-band imaging survey of a large number of post-AGB stars. We aim at a systematic survey to probe the inner dusty regions of post-AGB stars.

2 TARGET SELECTION

The large sample of observations presented here comes from five distinct observing runs [three VISIR/VLT runs: 380.D-0630 (normal mode), 081.D-0130 (burst mode), 081.D-0616 (normal mode); one Michelle/*Gemini-North*: GN-2005B-Q-16 and one T-Recs/*Gemini-South* run: GS-2005A-Q-34] and the target selection was done in a slightly different way for the different programs. The targets of the VISIR normal mode programs were selected from the previous mid-infrared catalogue by Meixner et al. (1999) and the millimetre observations compiled by Bujarrabal et al. (2001). We removed the AGB stars and young PNe and observed all the stars observable with the VLT.

Most of the stars observed in burst mode were selected from the Torun post-AGB stars catalogue (Szczerba et al. 2007), which lists 326 known post-AGB stars. We selected all the post-AGB stars observable in July from the European Southern Observatory (ESO) Cerro Paranal observatory with an *InfraRed Astronomical Satellite (IRAS)* 12 μm flux larger than 10 Jy (the burst mode works only for bright stars). These post-AGB stars include PPNe, R CrB stars and RV Tauri stars. R CrB are hydrogen-deficient post-AGB stars with known obscuration events (Clayton 1996). RV Tauri are pulsating post-AGB stars, located in the high-luminosity end of the Population II Cepheid instability strip (Wallerstein 2002). These RV Tauri stars are likely to harbour compact dusty discs (Van Winckel 2003).

In addition to that, we observed the brightest water fountains, and AGB stars observable during this period. Water fountains are oxygen-rich PPNe characterized by the presence of blue and red-shifted OH and H₂O masers (Likkell & Morris 1988). The stars observed with *Gemini* were selected from their infrared spectral properties. We selected stars with double chemistry (characterized by the presence of polycyclic aromatic hydrocarbons (PAHs) and crystalline silicates in their infrared spectra), the unidentified 21 μm features or hints of the presence of an equatorial dusty disc/torus.

We observed 93 targets: 52 PPNe, 10 water fountains, 11 AGB stars, eight RV Tauri stars, four PNe, four Massive Evolved Stars, two R CrB stars, one Be and one H II regions.

3 OBSERVATIONS AND DATA REDUCTION

3.1 VISIR/VLT observations

Most of the observations presented here were obtained with the mid-infrared instrument VISIR on the VLT (Lagage et al. 2004). All the stars were observed with three filters: PAH1 (8.59 μm , half band width 0.42 μm), SiC (11.85 μm , 2.34 μm) and Ne II (12.81 μm , 0.21 μm). The PAH1 and Ne II filters were chosen for their good

sensitivities and their location at the blue and red edge of the mid-infrared N band. They also avoid the large opacities of the SiC or silicate features and provide information on the dust continuum for both oxygen and carbon-rich stars. The broad SiC filter was chosen to provide a general N -band view. Images obtained with the SiC filter generally have a higher signal-to-noise ratio due to the better sensitivity of this broad-band filter. As all our selected targets are bright, we used the minimum integration time of 30 s for all the filters in all our observations.

We used the imager in normal and burst mode, using a pixel scale of 0.075 arcsec and a field of view of 19.2×19.2 arcsec². We used the standard chopping/nodding technique to remove the noise from the sky. With the burst mode, all the single chopping and nodding images are recorded, allowing the reconstruction of quality-enhanced images using shift and add techniques and lucky imaging.

We used the standard chopping/nodding technique to remove the background, with a perpendicular chop throw, a chopping frequency of 0.25 Hz and an amplitude of 8 arcsec. We shifted and added the images using a maximum of correlation algorithm, after removing the bad images, selected as the one for which the measured flux was smaller than the mean flux of all the images minus one sigma. The great observing conditions during our run (0.43 mm of water in the atmosphere) allowed us to obtain great quality diffraction-limited images.

The normal mode data were reduced using the VISIR ESO pipeline. The pipeline first detects the bad pixels, and cleans them using an interpolation with neighbouring pixels. Nodding images are then created by averaging the images in the two positions of the chopper. The nodded images are then shifted and added to form the final combined image.

3.2 T-Recs/*Gemini*-South observations

Images were obtained using T-Recs/*Gemini*-South and filters centred at 11.3 μm (PAH, $\Delta\lambda = 0.61$ μm) and 18.3 μm (Qa, $\Delta\lambda = 1.51$ μm). The chop throw was set to 15 arcsec.

The IRAF MIDIR data reduction package MIREDUCE command was used to combine the different nod images. The resulting registered images were averaged together using the IRAF MISTACK routine. The pixel scale of the obtained images was 0.09 arcsec and the field of view was 28.8×21.6 arcsec².

3.3 Michelle/*Gemini* observations

The observations were made with the mid-infrared camera Michelle on the 8-m *Gemini*-North telescope (Hawaii, USA) in queue mode in different nights spread between 2005 August 26 and 2006 January 8. We observed BD +30 3639, IRAS 21282+5050, OH 231.8 and the Red Rectangle with three N -band filters [centred at 7.9 ($\Delta\lambda = 0.7$ μm), 8.8 ($\Delta\lambda = 0.9$ μm), 9.7 ($\Delta\lambda = 1.0$ μm) and 11.6 μm ($\Delta\lambda = 1.1$ μm)] and the Qa filter (centred at 18.5 μm , $\Delta\lambda = 1.9$ μm). HD 56126 was observed with the same filters and the N -band 7.9 μm filter. The N - and Q -band observations were made at different dates due to the more stringent weather requirements at Q band. The standard chopping–nodding technique was used to remove the sky, with a chop throw of 15 arcsec. The spatial resolution measured from standard stars was typically ~ 0.4 arcsec at 10 μm and ~ 0.6 arcsec at 18.5 μm . The field of view was 32×24 arcsec² and the pixel scale 0.099 arcsec.

Michelle data files contain planes consisting of the difference for each chopped pair for each nod-set. Using the *Gemini* IRAF

package, these difference images were combined to create a single frame.

We thus observed in a quasi-uniform way 93 evolved stars in the mid-infrared. The names, coordinates, observing modes used and generally accepted type classification of all the stars are presented in Table A1. Table A2 presents photometric measurements from the stars from Two Microns All Sky Survey (2MASS) and the *IRAS*.

3.4 Flux calibration, deconvolution and artefacts

The VISIR mid-infrared detector used for most of the observations suffers from striping and the appearance of ghosts for bright stars. The stripes are horizontal and repeated every 16 pixels, while the ghosts are distributed vertically every 16 columns. This produces artefacts that could cause confusion for the image morphology classification.

For all the targets, we observed standard stars just after or before the observations. These standard stars were selected to have a similar airmass to our targets. These observations were reduced in a similar way as the science targets. They were used as a measurement of the point spread function (PSF) and for flux calibration purposes. The flux calibration was performed using standard aperture photometry methods, applied to the program and reference stars. All the resolved targets were deconvolved using a Richardson–Lucy algorithm and ~ 30 iterations, depending on the quality of the images.

4 RESULTS

4.1 Measurements

For each star and each filter observation, we estimated the ellipticity of the obtained image using an ellipse fitting procedure to all the signal larger than three times the standard deviation of the distribution. This gives us an orientation of the object, as well as its dimensions along its major axis and the axis perpendicular to this axis. To estimate whether the objects were resolved or not, we fitted a Gaussian to the observed radial profiles for the objects (on the non-deconvolved images) and their associated PSF standard for the different filters. Given the seeing stability due to the exceptionally good weather condition for the VISIR burst mode run, it is straightforward to estimate whether an object is extended or not for objects observed in burst mode. For objects observed in service mode, we estimated that the objects were extended when the object was 50 per cent more extended than its associated PSF. For some dubious cases, where there were hints of an extension in a given direction, we also checked the literature for similar structures observed at different wavelengths.

4.2 Observed morphologies

We observed 93 objects, and according to our measurements, 59 are point sources. A brief description of the properties of the resolved targets is presented in Table A8. Among these extended targets, we resolved a wealth of different structures, such as resolved central cores, dark central lanes, detached shells, S-shaped outflows. The asymmetrical object (IRAS 12405–6219) was misclassified as a post-AGB star and is in fact an H II region (Suárez et al. 2009). One object (IRAS 18184–1302) appears a square-shaped object and is also a misclassified post-AGB. It is a Be star (Tuthill & Lloyd 2007).

If we consider only the PPNe from our sample, we end up with a sample of 52 detected objects. 29 of these objects are not resolved and six are marginally resolved. Among the 17 clearly resolved objects, we find three ellipticals, 10 bipolars and four multipolars.

The 11 AGB stars we observed are unresolved, as well as the eight RV Tau stars. This seems to indicate that no dust shell is present around these stars or at least no large and bright shells. Half of the 10 water fountains we observed are resolved. None of the resolved ones is spherical. We observed four bipolar water fountains, most of them with a dark equatorial lane, and one multipolar. For the RCrB stars, one (IRAS 14316–3920) appears unresolved, and the other (IRAS 19132–3336) appears to be an unresolved central source with a more or less spherical dust shell around (very weak).

The morphologies of the clearly resolved objects are summarized in Table A8.

5 RESOLVED OBJECTS

5.1 Proto-planetary nebulae

5.1.1 IRAS 06176–1036

This object, dubbed the Red Rectangle (AFGL 915, HD 44179), has been well studied since its discovery by Cohen et al. (1975). It certainly harbours a binary system and exhibits a dual dust chemistry, with the presence of PAHs and crystalline silicates, as revealed by its *ISO* spectrum (Waters et al. 1998). CO observations reveal the presence of a Keplerian disc in the equatorial plane (Bujarrabal et al. 2005). Observations in the optical and the near-infrared of the Red Rectangle reveal an X-shaped nebula, projection of a bicone (Osterbart, Langer & Weigelt 1997; M ekarnia et al. 1998; Tuthill et al. 2002). *HST* images of the nebula reveal a very complex morphology, with a ladder-like structure inside the X-shaped nebula (Cohen et al. 2004). The central star is not seen in these images, as it is obscured by a dark lane, certainly due to a dusty disc. The rung of the ladder shows a quasi-periodic spacing, indicating a periodic mass-loss from the central star.

Hora et al. (1996) observed the Red Rectangle in the mid-infrared with United Kingdom Infrared Telescope (UKIRT). Their multi-wavelength images (between 8 and 20 μm) show a bright core surrounded by a rectangular-shaped nebula. Lagadec, de Freitas Pacheco & M ekarnia (2004) obtained Thermal Infrared Multimode Instrument (TIMMI)/ESO 3.6 m images of the Red Rectangle in the *N* band. The observations reveal an extended ($6 \times 8 \text{ arcsec}^2$) rectangular-shaped nebula elongated along the north-east/south-west direction and symmetrical along this direction. The central core appears unresolved. The X-shape seen at shorter wavelengths is clearly seen at 8.4 μm and is less clear at longer wavelengths. The Red Rectangle was also imaged with the SUBARU telescope (Miyata et al. 2004). A similar morphology is revealed, and their 8.8 μm image reveals a similar morphology as the one observed in the near-infrared (M ekarnia et al. 1998). The *N*-band emission is dominated by UIR emission, attributed to PAHs, while the central bicone seen at the shortest wavelengths is predominantly due to emission from hot dust and/or from stochastically heated nanoparticles (Gledhill et al. 2009).

Our Michelle images of the Red Rectangle at 7.9, 8.8, 11.6, 12.5 and 18.1 μm are displayed in Fig. B1. The images at 7.9, 8.8, 11.6 and 12.5 μm are quite similar and display the well-known rectangular shape of the Red Rectangle, with dimensions $3.3 \times 5.9 \text{ arcsec}^2$.

The X-shape is clearly seen in our deconvolved images up to 11.6 μm . At 18.1 μm , the emission is dominated by an unresolved point source.

5.1.2 IRAS 07134+1005

HD 56126 is a well-studied post-AGB star exhibiting the unidentified 21 μm dust feature (Kwok, Volk & Hrivnak 1989). It is a carbon-rich post-AGB star and its envelope has been already resolved in the mid-infrared with TIMMI2 on the ESO 3.6-m telescope (Hony et al. 2003) and OSCIR on *Gemini-North* (Kwok, Volk & Hrivnak 2002). They clearly detected the central star at 10.3 μm and marginally at 11.7 and 12.5 μm . They resolved a shell-like envelope of $\sim 5 \text{ arcsec}$ in diameter, clearly elongated towards the south-west. The shell is not complete and shows an opening in the direction of its elongation.

The VISIR images of IRAS 07134 at 8.59, 11.85 and 12.81 μm are displayed in Fig. B2. Our Michelle/*Gemini* images of HD 56126 at 8.8, 11.6, 12.5 and 18.1 μm are displayed in Fig. B3. The images have a similar morphology and dimensions of $4.4 \times 4.8 \text{ arcsec}^2$ at all the observed wavelengths. The envelope has a roughly elliptical shell with a position angle (PA) of $\sim 25^\circ$, that is wider at the north. The brightest part of the nebula is a U-shaped structure located in the inner part of this elliptical envelope. This U-shaped structure shows a decrease in emission in the north-west. The central star is clearly detected from 8.6 to 11.9 μm weakly at 12.8 μm and not at longer wavelengths. Its relative brightness clearly decreases with increasing wavelength. Our images are very similar to those obtained previously, but are certainly sharper. This is clear in our deconvolved images that show the presence of filamentary structures and holes that are very similar in the three filters. We thus clearly see a hole in emission $\sim 1.4 \text{ arcsec}$ south of the central star, which could be due to a decrease in the dust density, or to the presence of a cold dusty blob.

5.1.3 IRAS 07399–1435

OH 231.8+4.2 is a remarkable bipolar nebula with a central star (QX Pup) still on the AGB with probably an A0 main-sequence companion (S anchez Contreras, Gil de Paz & Sahai 2004). Its circumstellar envelope has already been imaged at 11.7 and 17.9 μm using the Keck telescope (Jura, Chen & Plavchan 2002), showing it to be elongated along the same direction as the bipolar outflows observed at shorter wavelengths with PA $\sim 22^\circ$ and a full length $> 3 \text{ arcsec}$, the nebula being wider towards the north-east. Our Michelle images of OH 231.8 at 8.8, 9.7, 11.6 and 18.1 μm are displayed in Fig. B4. The vertical stripe at the east of the image is a detector artefact, amplified in our deconvolved images. Some artefacts are also seen in the 8.8 μm image, seen as ‘holes’ north and south of the central source. The four images are extended along PA $\sim 22^\circ$. The dimensions of the images are $4.1 \times 6.1 \text{ arcsec}$, $2.6 \times 4.3 \text{ arcsec}$, $4.3 \times 6.7 \text{ arcsec}$ and $5.4 \times 9.9 \text{ arcsec}$ at 8.8, 9.7, 11.6 and 18.1 μm , respectively. All the images show the presence of a bright unresolved core and a diffuse halo. This halo is larger towards the south-east, in contradiction with observations by Jura et al. (2002). This is, however, in agreement with previous *N*-band observations of this object with TIMMI on the ESO 3.6-m telescope (Lagadec 2005).

The central core appears resolved at 9.7 μm (its full width at half-maximum (FWHM) is $\sim 0.6 \text{ arcsec}$ while its PSF standard has an FWHM of $\sim 0.6 \text{ arcsec}$) and 18.5 μm (FWHM of 0.8 and 0.6 arcsec

for the object and its PSF, respectively). These are the wavelength of silicates stretching and bending modes.

Mid-infrared spectro-interferometric observations of OH 231.8+4.2 have resolved the central core (Matsuura et al. 2006). This core was overresolved by the interferometer near the deep silicate absorption feature they observed around $9.7 \mu\text{m}$. This indicates the presence of a large silicate dust structure in the equatorial plane of OH 231.8+4.2.

5.1.4 IRAS 10197–5750

Roberts 22 is a well-studied PPN with dual dust chemistry (Sahai et al. 1999). Its envelope has been resolved in the mid-infrared with TIMMI observation on the ESO 3.6-m telescope (Lagadec et al. 2005). They obtained 8.39 and $11.65 \mu\text{m}$ images of this object. Both images show an envelope elongated in the direction north-east/south-west along $\text{PA} \sim 45^\circ$.

Images of the envelopes have also been obtained at shorter wavelengths by the *HST* (Sahai et al. 1999; Ueta, Murakawa & Meixner 2007) or using the adaptive optics on the VLT (Lagadec et al. 2007). These images revealed the presence of an S-shaped envelope, embedded in a larger bipolar envelope.

Our VISIR and T-Recs images (Figs B5 and B6) clearly show the presence of a large-scale S-shaped envelope. An asymmetric torus is resolved in the core of this envelope from 8 to $18 \mu\text{m}$. The torus is brighter along the equator, which is more or less perpendicular to the bipolar nebula. We obtained VISIR observations of Roberts 22 with the same filters as the present observations in 2006 November. The orientation of the torus appears exactly the same as the one we present here. The observed S-shaped structure of the nebula is thus certainly not due to precession from this torus. Note that the orientation of the torus appears to be wavelength dependent, as indicated by the *Gemini Q*-band image. This is a radiative transfer effect.

5.1.5 IRAS 15103–5754

This is a candidate PN with H_2O maser emission (Suárez et al. 2009). The images presented in Fig. B7 are the first ever of this object. We clearly resolved a bipolar nebula with a narrow waist, probably due to a dense equatorial dusty structure. The nebula is elongated along a north-east/west direction along $\text{PA} \sim 35^\circ$. Some spurs are observed at the edges of the bipolar structure and are more prominent in the north-west lobe. This could be due to the presence of the high-velocity jets inferred by the water masers.

5.1.6 IRAS 15445–5449

IRAS 15445–5449 is a water fountain nebula (Deacon et al. 2007). We obtained the first ever images of this source. We resolved a compact ($1.5 \times 2.3 \text{ arcsec}^2$) bipolar structure (Fig. B8), with a dark equatorial waist, indicating the presence of a dense equatorial structure. This equatorial lane is perpendicular to the bipolar lobes that are elongated along $\text{PA} \sim 5^\circ$. The edges of these lobes are terminated by spurs, which are probably the projection of a biconical structure on the plane of the sky.

5.1.7 IRAS 15553–5230

IRAS 15553–5230 is a poorly studied PPN. It was resolved using optical *HST* observations (Sahai et al. 2007; Siódmiak et al. 2008).

Their observations revealed a small ($2.5 \times 1.1 \text{ arcsec}^2$) bipolar nebula, seen nearly edge-on, elongated along the east/west direction with a dense equatorial waist, similar to a hourglass. The lobes differ in shape and size, which is probably due to the fact that the east lobe is pointing in our direction. A small feature is observed in this lobe and could be a faint outflow or jet.

Fig. B9 presents our VISIR images of this source. We resolved the nebula, with a point source in its core, and it appears to be elongated along the east/west direction.

5.1.8 IRAS 16279–4757

IRAS 16279–4757 object is a PPN star with both carbon (PAHs) and oxygen-rich (crystalline silicates) material in its envelope. This envelope was well studied by Matsuura et al. (2004) using TIMMI2/ESO 3.6-m telescope mid-infrared images. They resolved the envelope and classified it as bipolar. Our VISIR observations (Fig. B10) show that the envelope of IRAS 16279-4757 has a much more complex morphology. A large-scale S-shaped structure is clearly seen in the two filters, with some large-scale horn-like structures towards the north-west and the south-west. The central star is clearly seen in all images, surrounded by Airy rings. On the deconvolved images we can see that the dust is organized in filamentary structures with many holes representing underdensities in the dust distribution. The big hole seen on the deconvolved PAH1 just north of the central star is an artefact due to the detector.

5.1.9 IRAS 16342–3814

IRAS 16342–3814 is the prototypical object of the water fountain class (Likkell & Morris 1988). It has been observed by Verhoelst et al. (2009). They resolved a bipolar nebula, separated by a waist dark even in the mid-infrared. They find that this dark waist is mostly made of amorphous silicates and that its filling angle is fairly large and this structure is thus not a disc. Our two observations show the same bipolar morphologies, one of our filters being the same as the one used by Verhoelst et al. (2009). But, due to the use of the burst mode on VISIR our deconvolved images (Fig. B11) are sharper than the ones obtained earlier.

5.1.10 IRAS 16594–4656

The Water-Lily nebula PPN has been observed in the mid-infrared (*N* and *Q* bands) with T-Recs on *Gemini* (Volk et al. 2006) and with TIMMI2 on the ESO 3.6-m telescope (García-Hernández et al. 2006). A bright equatorial torus, seen nearly edge-on, is clearly resolved in their images. No sign of the point symmetry observed in the optical images is seen in the mid-infrared ones. The nebula has an overall elliptical shape and is elongated along the east-west direction ($\text{PA} \sim 80^\circ$). Our mid-infrared images (Fig. B12) show a similar morphology, but the larger dynamic range allows us to see some more diffuse dust emission beyond the lobes.

5.1.11 IRAS 17106–3046

Optical *HST* images of the PPN IRAS 17106–3046 (the spindle nebula) indicate the presence of a collimated outflow emerging from a visible disc, embedded in a lower density elliptical halo (Kwok, Hrivnak & Su 2000). The pair of lobes is collinear, orientated along a PA of 128° , and the disc is perpendicular to these lobes with

PA $\sim 42^\circ$. Our images (Fig. B13) reveal the presence of a dense central structure along PA $\sim 42^\circ$.

5.1.12 IRAS 17150–3224

The Cotton Candy nebula is a well-studied bipolar PPN. It has been observed in the optical and in the near-infrared by the *HST* (Kwok, Su & Hrivnak 1998, Su et al. 2003). The central star is visible in the near-infrared images, but not in the optical where it is obscured by a dark lane. This dark lane separates two lobes that form an extended bipolar nebula along a PA of $\sim 112^\circ$. Near-infrared spectroscopic observations provide evidence for the presence of an expanding torus in the core of IRAS 17150 (Weintraub et al. 1998).

Our VISIR and T-Recs images of IRAS 17150 are displayed in Figs B14 and B15. The central star is not seen in our images between 8 and 20 μm . These images reveal an unresolved central peak, located at the position of the dark lane observed at shorter wavelengths. The nebula is elongated along PA $\sim 108^\circ$, similar to the bipolar nebula observed in the optical. An elongation is also seen in a direction roughly perpendicular to this bipolar nebula, more clearly in the 8.59 μm deconvolved image.

5.1.13 IRAS 17311–4924

IRAS 17311–4924 is a carbon-rich PPN (Hony, Waters & Tielens 2002). Its *ISO* spectrum reveals the presence of PAHs, SiC and a 30 μm feature usually associated with MgS in its envelope (Hony et al. 2002). The images we present here are the first ever obtained for this object. The images reveal a bipolar nebula seen edge-on with two bright lobes on both sides of the polar direction. This is the projection of an equatorial torus, aligned with the bipolar structure.

5.1.14 IRAS 17441–2411

The Silkworm Nebula is a PPN with a multipolar envelope (Ueta et al. 2007). It has been imaged at high angular resolution with the *HST* (Ueta et al. 2007) in the optical and near-infrared, and with *Gemini* in the mid-infrared (Volk, Kwok & Hrivnak 2007), which resolved a torus, tilted by 23° with respect to the bipolar nebula observed in the optical. They raised the possibility that this torus is precessing at a rate of 1 deg yr^{-1} , which could lead to the precession of the outflows. This is supported by the possible S-shape of the nebula, which can be seen in the near-infrared, and guessed in the mid-infrared *Gemini* images. This S-shaped structure is clearly seen in our VISIR image (Fig. B17), more particularly in the 11.65 μm deconvolved image. Our images are also deeper and reveal the presence of cooler dust around this structure as it in the case of Roberts 22.

5.1.15 IRAS 18276–1431

IRAS 18276–1431 is a star in the short transition phase between the OH/IR phase and the PN phase, as indicated by the progressive disappearance of H₂O maser (Engels 2002). Near-infrared images obtained with adaptive optics on the Keck (Sánchez-Contreras et al. 2007) show that the envelope of IRAS 18276 displays a clear bipolar morphology (PA $\sim 23^\circ$) with two lobes separated by a dark waist. Some strong OH masers activity is observed in the dense equatorial region, approximately perpendicular to the bipolar lobes (Bains et al. 2003). Our images show a bipolar structure with a PA of $\sim 9^\circ$,

embedded in a larger dusty structure (more visible at 11.65 μm , as this filter is more sensitive).

5.1.16 IRAS 18450–0148

W43A is a water fountain source (Imai et al. 2002). Water maser observations of this source revealed the presence of a collimated and precessing jet of molecular gas. The H₂O maser spots are concentrated in two clusters, one receding (north-east) and one approaching (south-west side) (Imai et al. 2002). The two clusters are separated by $\sim 0.65 \text{ arcsec}$. The jets have a position angle of $62:7 \pm 0:5$. Our VISIR observations allowed us to resolve a compact ($1.2 \times 1.6 \text{ arcsec}$) bipolar dust shell in W43A, orientated along PA $\sim 62^\circ$. The molecular jets have thus certainly shaped the dusty bipolar structure we resolved.

5.1.17 IRAS 19016–2330

IRAS 19016–2330 is a PPN (García-Lario et al. 1997). Our images of IRAS 19016–2330 are the first ever obtained for this object. They show a compact structure elongated along PA $\sim 25^\circ$, embedded in a structure elongated along the east/west direction.

5.1.18 IRAS 19374+2359

This PPN has been observed in the optical with the *HST* (Ueta, Meixner & Bobrowsky 2000) and in the near-infrared with UKIRT, in imaging and polarimetry (Gledhill 2005). In the optical, IRAS 19374+2359 appears bipolar, with its central star partially visible and limb-brightened bipolar lobes along PA $\sim 6^\circ$. The near-infrared polarimetric maps indicate scattering and emission from an optically thin axisymmetric dust shell. The nebula appears to be brighter in the north than in the south and two brightness peaks can be seen east and west of the central star.

Our observations (Fig. B21) show a more or less elliptical nebula along PA $\sim 11^\circ$. The detached shell predicted from the polarimetric observations is clearly resolved, and we confirm that the nebula is brighter towards the north. An opening in the shell is actually observed towards the south, and this object looks very similar to IRAS 07134+1005.

5.1.19 IRAS 19386+0155

IRAS 19386+0155 was observed in the near-infrared imaging polarimetric survey by Gledhill (2005). Its degree of polarization is low but there is some evidence for scattering. The core of the polarized intensity image is elongated along an approximately north/south direction, while the outer region has a north-east/south-west orientation. They suggest that this object has a bipolar morphology. Our images (Fig. B22) are the first to resolve this object in the mid-infrared. We can see that the nebula is elongated in the south-east/north-west direction, perpendicular to the extension observed in the near-infrared.

5.1.20 IRAS 19454+2920

This object is not very well studied. The only study of its morphology was done in the near-infrared imaging polarimetric survey performed by Gledhill et al. (2001). Their observations show that this object is unresolved and unpolarized. Our VISIR images (Fig. B23) reveal the presence of a bipolar nebula, elongated along a direction

roughly east/west, with a central structure elongated in a direction perpendicular to the bipolar nebula.

5.1.21 IRAS 19500–1709

IRAS 19500–1709 is a carbon-rich PPN, with 21 and 30 μm features in its mid-infrared spectrum (Justtanont et al. 1996). It has been imaged in the mid-infrared with OSCIR/*Gemini*-North (Clube & Gledhill 2004). An extended circumstellar envelope is detected, and there are some indications that this envelope is elongated along the north-east/south-west direction. Using radiative transfer modelling, Clube & Gledhill (2004) estimated the inner and outer radii of a detached dust shell around this object. They obtained an inner radius of 0.4 arcsec, not resolved with their OSCIR observations.

Our observations (Fig. B24) show that the envelope around 19500 is extended and elongated along two preferential direction, north-east/south-west as mentioned by Clube & Gledhill (2004) but also east/west. A detached shell is clearly resolved at all three wavelengths, with an inner radius of ~ 0.4 arcsec.

5.1.22 IRAS 20043+2653

IRAS 20043+2653 has been resolved in the near-infrared (*K* band) by Gledhill (2005) using polarimetric measurements. The polarization map suggests that the object is bipolar. This is supported by the polarized flux image, which shows an extension along PA $\sim 120^\circ$, while the polarization vectors are almost perpendicular to that direction. Our VISIR observations show that this object is slightly resolved and show an extension along PA $\sim 114^\circ$ in all three filters, in a similar direction as the polarization flux image.

5.2 Planetary Nebulae

5.2.1 IRAS 14562–5406

Hen 2–113 (He 1044) is a very young PN with a [WC] central star, and displays dual dust chemistry, with the presence of PAHs (carbon-rich) and crystalline silicates in its envelope (Waters et al. 1998). *HST* observations reveal a complex morphology for this very young PN (Sahai, Nyman & Wootten 2000), with the presence of a spherical halo, remnant of the AGB mass-loss. A bipolar structure is observed along PA $\sim 136^\circ$, with a globally elliptical morphology with other faint lobes, the brightest along PA $\sim 55^\circ$. A bright core is observed in this elliptical structure, showing the presence of two rings separated by a dark lane. This object was observed by Lagadec et al. (2006) in the near- and mid-infrared. Their observations are limited to the bright core and show that rings are the projection of a diabolo-like dusty structure (Lagadec et al. 2006). The central star is visible at short wavelength, up to 5 μm , but is not detected in the *N* band.

Our T-Recs mid-infrared images (Fig. B26) reveal a global structure similar to the one reported by Lagadec et al. (2006). But, the better resolution of the present observations allows us to clearly resolve the brightest ring in *N* and *Q* bands.

5.2.2 IRAS 16333–4807

IRAS 16333–4807 is an H₂O PN (Suarez et al. 2009). We present here the first resolved image of its envelope. We resolved a compact nebula. The envelope appears point symmetric, with an unresolved central core defining a very narrow equatorial waist. The holes

seen north and south of the central star (more clearly seen in the deconvolved image) could be artefacts due to the detector. The point symmetry of this source is an indication that it has been shaped by precessing jets.

5.2.3 IRAS 17047-5650

CPD-56°8032 is a young PN with a [WC] central star and is spectroscopically the twin of Hen 2–113. An edge-on disc in its core has been discovered by De Marco, Barlow & Cohen (2002) through *HST*/STIS spectroscopy. A study combining *HST* imaging and MID-infrared Interferometric Instrument (MIDI)/VLTI interferometry of CPD-56 revealed the complexity of this object (Chesneau et al. 2006). The *HST* image reveals the presence of several lobes, in a shape similar to the Starfish nebulae described by Sahai & Trauger (1998). The farthest structure is located 7 arcsec away from the central star. A well-defined lobe is observed along PA $\sim 53^\circ$. The mid-infrared environment of CPD-56°8032 is barely resolved with single dish VLT images obtained during the MIDI acquisition at 8.7 μm . It is elongated along a PA of $\sim 104^\circ$ and a dimension of $\sim 0.3 \times 0.4$ arcsec². This orientation corresponds to none of the observed lobes but is similar to that of a bow shock observed next to the central star in the *HST* image. The interferometric measurements reveal the presence of a dusty disc, with an orientation along a PA of $\sim 28^\circ$, corresponding to none of the structures observed.

Our T-Recs images (Fig. B28) reveal a bipolar nebula with a bright central structure elongated along PA $\sim 123^\circ$ and an overall bipolar structure almost perpendicular to this. This central structure seems to indicate the presence of a dusty disc in this direction, but puzzlingly, its orientation is almost perpendicular to the one inferred from the MIDI observations. Two bright structures are observed towards the north and south of these equatorial structures, and are separated by density gaps. The shape of the northern structure has the same orientation as the bow shock observed by the *HST*.

5.2.4 IRAS 17347–3139

IRAS 17347–3139 is a young PN with water masers. Its circumstellar envelope has been resolved by Sahai et al. (2007), using *HST* optical and near-infrared observations. These reveal the presence of bipolar collimated outflows separated by a dark waist. The lobes are asymmetric in shape and size, the north-west lobe being larger and the morphologies of these lobes seem to indicate that the jets shaping the nebula are precessing. A faint spherical halo can be observed at shorter wavelengths, up to a radius of 2 arcsec. VLA observations (Tafoya et al. 2009) reveal that the ionized shell consists of two structures. An extended (1.5 arcsec) bipolar structure with PA $\sim -30^\circ$, similar to the one observed by the *HST*. The other structure is a central compact structure (~ 0.25 arcsec) elongated in a direction perpendicular to the bipolar structure, similar to the dark lane observed in the *HST* image. IRAS 17347 appears slightly extended in the mid-infrared images published by Meixner et al. (1999). Our VISIR observations clearly resolved the bipolar structure with an unresolved central core. The deconvolved images reveal that the nebula is not bipolar, but multipolar. This indicates that the nebula has been shaped by precessing jets.

5.2.5 IRAS 19327+3024

BD+30°3639 is one of the best studied dual dust chemistry PN. It is a dense, young PN with a [WC9] central star. The *HST* imaging

has shown that this nebula has a remarkable elliptical ‘squared off’ morphology (Harrington et al. 1997). Kinematic studies of this object indicate that its nebula is seen nearly pole-on, with the rotational symmetry axis at about PA 30° – 60° in the plane of sky and an inclination of about 20° (Bryce & Mellema 1999).

Our Michelle images of BD+30°3639 at 8.8, 9.7, 11.6 and 18.5 μm are displayed in Fig. B30. The morphology of these images is remarkably similar to the optical ones obtained by the *HST*, displaying an elliptical-rectangular shape. The images are very similar at the four observed wavelengths with dimension 6.8×8.0 arcsec². The elliptical ring appears to be very clumpy, what is best seen on the deconvolved images. Note that the clumpy structures are observed at similar location in different images and are thus not deconvolution artefacts. The north east of the ring appears to be the brightest, while the south-east is weaker, displaying a kind of hole. This ring structure is surrounded by a faint elliptical halo. Some filamentary structures are also observed inside the ring, with a decreasing intensity towards the location of the central star that is not detected in any of our MIR images.

5.2.6 IRAS 21282+5050

This is a young carbon-rich PN with a [WC 11] central star and is located at ~ 2 kpc (Shibata et al. 1989). Michelle images of IRAS 21282+5050 at 8.8, 9.7, 11.6 and 18.1 μm are displayed in Fig. B31. As already mentioned by Meixner et al. (1993) using MIR observations and the NASA 3-m Infrared Telescope Facility (IRTF) telescope, the structure of the nebula appears the same in all the images, with an elliptical nebula having a major axis at PA $\sim 165^{\circ}$ and two peaks lying almost east/west. The dimension of this extended structure is 5.4×3.6 arcsec². The central star is not detected in all our images. The two observed lobes can be interpreted as the projection of a dusty torus seen roughly edge on.

5.3 Evolved massive objects

5.3.1 IRAS 10215–5916

AFGL 4106 is a post-red supergiant binary (Molster et al. 1999). Optical observations with the ESO/NTT telescope revealed the shape of the ionized region in its circumstellar envelope through the $H\alpha$ line (van Loon et al. 1999). An arc, extending from roughly north-east to south-west clockwise, is seen. The TIMMI/ESO mid-infrared images of AFGL 4106 show that the dust has an oval to box shaped distribution, with a bright unresolved peak centred on the central objects (Molster et al. 1999). The dust distribution shows some indications of clumpiness. The north-west part of the nebula is fainter compared to the rest and seems slightly more extended, while the $H\alpha$ shows a clear anti-correlation with the MIR emission.

Our T-Recs images of AFGL 4106 (Fig. B32) show a similar overall morphology of the dust distribution as the one observed by Molster et al. (1999). But the higher angular resolution of our observations allows us to resolve structure inside the envelope of AFGL 4106. The arc seen in $H\alpha$ is clearly resolved, but larger, extending from east to west clockwise. A smaller arc is clearly seen, extending from north to west anticlockwise. Many other clumps and underdensities are clearly seen. The central parts of the nebula show a bright clump, extended in a direction perpendicular to the elliptical nebula. The arcs seen could form a spiral structure, similar to the pinwheel nebula observed around WR 104 (Tuthill et al. 2008). The pinwheel structure observed in WR 104 is due to dust formation triggered by the interaction of the wind from the mass-losing star

and the orbiting companion. AFGL 4106 is known to be a binary system, and it is thus very likely that the spiral structure we observe is also due to a wind–binary companion interaction.

5.3.2 IRAS 17163–3907

IRAS 17163–3907 (Hen 1379) was discovered by Henize in 1976 (Henize 1976). Despite being one of the brightest mid-infrared objects in the sky, it remains poorly studied. From near-infrared imaging, Epchtein et al. (1987) classified it as a PPN candidate. Its *IRAS* spectrum indicates the presence of silicate dust and it is unresolved in the optical by the *HST* (Siódmiak et al.), while speckle observations in the *L* band (3.6 μm) indicate an angular dimension of 1.11 ± 0.23 arcsec (Starck et al. 1994). We present here the first mid-infrared images of this target. It shows the presence of two concentric, almost circular, detached shells with an angular diameter of ~ 5.5 arcsec. A point source is clearly seen in all the images, and is brighter at shorter wavelengths. The deconvolved images show that the overall spherical shells are made of smaller patchy structures.

5.3.3 IRAS 19114+0002

IRAS 19114+0002 is classified as a yellow hypergiant or a post-AGB star, depending on the adopted distance. It was imaged in the mid-infrared with the Keck 1 telescope to resolve a detached shell around this object (Jura & Werner 1999). This shell has an inner diameter of ~ 3.3 arcsec and an outer diameter of at least 5.7 arcsec. They noted that the central star is offset from the centre of the shell by ~ 0.35 arcsec. This central star appears asymmetric in the east-west direction. They explained this by imperfect chop/nod motion. They also noted that the northern part of the almost circular shell is brighter and present some departure from spherical symmetry. Gledhill & Takami (2001) modelled the dust shell around IRAS 19114 seen in their polarimetric observations (Gledhill et al. 2001). They found that the observations are well reproduced with a spherically symmetric dust distribution and an r^{-2} density law. This is an indication that during the mass-loss phase, the mass-loss rate was constant. They estimated the dust mass of the shell to be $0.08 M_{\odot}$. In our images we observe a similar detached shell at all wavelengths, but also an east/west extension in the central object at 8 μm . As the PSF observations associated with all our observations are perfectly circular and we used the same settings for these observations, this structure cannot be due to chop/nod motion and is real. A weaker dusty structure seems to connect this central source to the detached shell. Some warmer dust is thus certainly present close to the central star.

5.3.4 IRAS 19244+1115

IRC +10420 is an F red supergiant with a dusty circumstellar envelope. This star is certainly in the short transition phase between RSG and Wolf–Rayet stars. It might be the only object in this transition phase (Blöcker et al. 1999). It is one of the brightest source in *N* and *Q* bands and has an intrinsic luminosity $L \sim 5 \times 10^5 L_{\odot}$ for a distance estimated to 5 kpc. IRC +10420 is thus very close to the Humphreys–Davidson limit, upper limit to the luminosity of stars. *HST* observations (Humphreys et al. 1997) show that the nebula around IRC +10420 is extended (~ 15 arcsec) with a bright core ~ 3 arcsec in diameter. This core has a very complex morphology. It has been observed in the *N* band (Humphreys et al. 1997;

Meixner et al. 1999). These images in the mid-infrared show that it contains two lobes separated by 1 arcsec. This core has a dimension $\sim 2 \times 2$ arcsec. *HST* observations show the presence of an elongation in the envelope with PA $\sim 215^\circ$. Recent radial motion studies (Tiffany et al. 2010) indicate that we are viewing IRC +10420 nearly pole-on. The extension they observe towards the south-west is likely to be the equatorial plane, with the south-west side pointing towards us.

Our VISIR images reveal the presence of an extended envelope, with an extension towards the south-west along a PA of $\sim 223^\circ$. It presents a more or less asymmetric morphology along that direction, as revealed by *HST* observations. The high dynamic range in our image also reveals the presence of complex structures inside the nebula.

5.4 Other objects

5.4.1 IRAS 12405–6219

IRAS 12405–6219 has been classified as a possible PN, based on its *IRAS* colours (van de Steene & Pottasch 1993). Suárez et al. (2009) noted that its near-infrared colours were very similar to those of H II regions. Our images show a morphology very unusual for a post-AGB star or a PN, but common to H II regions. IRAS 12405–6219 is thus very certainly an H II region.

5.4.2 IRAS 18184–1302

MWC 922 (a.k.a. the Red Square nebula) is a dust-enshrouded Be star (Tuthill & Lloyd 2007). Near-infrared Palomar adaptive optics images reveal a regular and symmetric structure around that object (Tuthill & Lloyd 2007). The images show a square-like structure, as the projection of biconal lobes, crossed by a series of rungs and an equatorial dark band crossing the core, with a PA of 46° . Our mid-infrared images show the same square-like structure, even if it is not fully clear due to striping that affected the whole right part of all our images. Our deconvolved images clearly reveal the presence of a core with a similar orientation as the one assessed from near-infrared imaging.

6 DISCUSSION

6.1 Two kinds of objects: resolved cores and detached shells

For the largest objects that are clearly resolved, we can notice that the PPNs observed can be divided into two categories: on one side the objects with a dense central core, in the form of a bright central source, resolved or not (IRAS 06176, IRAS 07399, IRAS 10197, IRAS 15103, IRAS 16279, IRAS 16594, IRAS 17150, IRAS 17311, IRAS 17441), or a dark lane, resolved or not, with most of the emission coming from the poles (IRAS 15445, IRAS 16342, IRAS 18276) indicating the presence of a large amount of dust, making the central regions optically thick even in the mid-infrared. On the other side, some objects do not have such a central core, and we can observe either a detached shell or the central star (IRAS 07134, IRAS 19374 and IRAS 19500). The objects without a central core all have an elliptical morphology, while the objects with a central core are either bipolar or multipolar. This can be seen in their SED, as the objects with a dense central core (Fig. 1) or an equatorial dark lane (Fig. 2) have a rather flat SED in the near-infrared wavelength

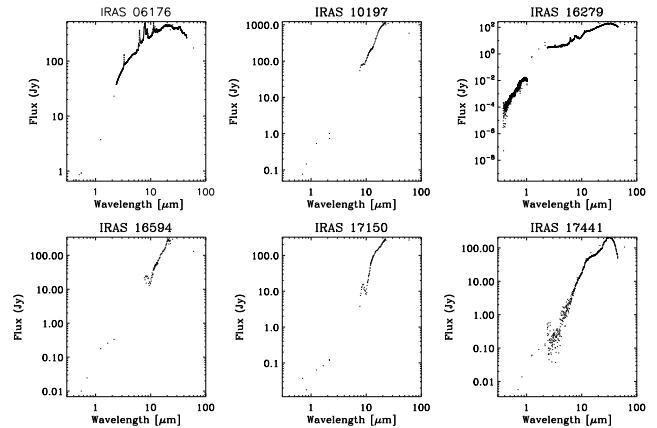


Figure 1. SED of the resolved objects with a bright central source.

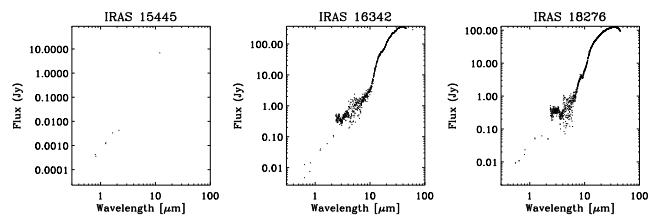


Figure 2. SED of the resolved objects with an equatorial dark lane.

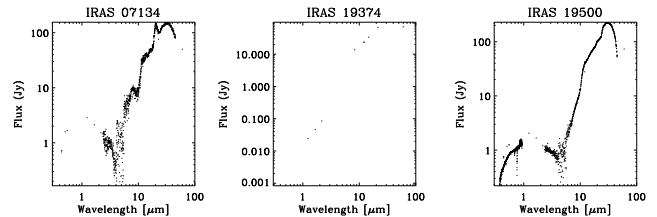


Figure 3. SED of the resolved objects with a detached shell.

range, due to the presence of hot dust close to the central star. The SED of the objects with detached shells are characterized by the presence of a clear double-peaked distribution (Fig. 3), with a first peak shorter than $1 \mu\text{m}$ due to the central star, and a second peak due to the cool dust in the shell. The flux is much lower in the near-IR due to the absence of dust close to the central star.

The shape of the SED can be affected by the orientation of the nebula too. The orientation of the nebula affects the ratio between the photospheric and the dust peaks of the SED (Su, Hrivnak & Kwok 2001), and only if the optic depth is significant. The presence/absence of infrared excess observed in our sources is different and thus not related to orientation effects. This infrared excess due to hot dust is an indication that the dense cores play a role in the shaping of the nebulae. Two main classes of models have been proposed to explain the shaping of nebulae. The first class of models is based on the Generalized Interacting Winds models described by Balick (1987). In these models, a fast wind from the central star of a PPN or PN interacts with a slower wind, remnant of the AGB phase, assumed to be toroidal.

In the second class of models, the primary shaping agents are high-speed collimated outflows or jets that are created at the end of the AGB phase or at the beginning of the PPN phase (Sahai &

Trauger 1998). The interaction of these jets with a spherical AGB wind will create lobes that are in fact cavities. If the direction of the jets changes with time, multipolar nebulae can be shaped.

Both models require the presence of a central torus/disc in the core of the nebulae. Our observations clearly indicate that the bipolar and multipolar nebulae have such a central structure in their core.

6.2 Departure from circular symmetry

We resolved 25 PPNe in our survey. All these nebulae show a clear departure from circular symmetry. Some circular shells are resolved in our survey, but only around massive evolved stars such as IRAS 17163 and IRAS 19114. A dramatic change in the distribution of the circumstellar material is often observed when a star evolves from the AGB phase to the PN phase (Balick & Frank 2002). Most AGB stars have a large-scale circularly symmetric morphology (Mauron & Huggins 2006), while PNe display a variety of morphologies from elliptical to bipolar or multipolar. Parker et al. (2006), from a large optical imaging survey of PNe, found that 80 per cent of the PNe show a clear sign of departure from circular symmetry, and thus that ~ 20 per cent of the PNe are spherical. The shaping of the PNe is thought to occur at the very end of the AGB phase or the beginning of the PPN phase. It is thus surprising that in our sample of 25 resolved PPN we do not find any circular ones.

The fact that we do not observe any circular PPNe could be a sample selection effect. We selected our targets as bright *IRAS* 12 μm sources. To be a bright emitter at these wavelengths, an object needs to have some dust hot enough (~ 300 K), and thus not far from the central star. This is the case for the stars with a central core, which are aspherical, as mentioned before. The spherical PPNe are fainter than the non-spherical ones in the mid-infrared, due to the lack of central torus/disc emitting in this wavelength range. At the end of the AGB phase, the envelope of the AGB progenitors of circular PPNe is ejected and rapidly cools down while expanding. There are thus very few spherical PPNe that are bright in the mid-infrared. Furthermore, those bright PPNe are compact and thus difficult to spatially resolve. The best way to detect such spherical envelopes is thus at longer wavelengths. Such detached shells are actually observed in the far-infrared with the *Herschel Space Observatory* (Kerschbaum et al. 2010).

6.3 Formation of S-shaped structures

As we mentioned in Section 5.1.14, for IRAS 17441 a tilt is observed between the orientation of the central dusty torus we resolved and the tips of the observed S-shaped structure. Such a tilt was observed by Volk et al. (2007), and measured to be almost 90° . They suggested that a precession of the dusty torus could explain the observed S-shaped structure of the nebula. They estimated the dynamical age of the envelope, assuming a distance of 1 kpc and an expansion velocity of 100 km s^{-1} , to be ~ 100 yr. According to this, the torus should thus precess with a rate of $\sim 1 \text{ deg yr}^{-1}$. As our observations were made 4 years after the observations presented by Volk et al. (2007), we should see a tilt of the torus of 4° between the two observations. The images provided by these authors show that the orientation of the torus they observed is exactly the same as the one we observed. The torus in the core of IRAS 17441 is thus not precessing at such a high rate. When we compare the images we obtained of IRAS 17441 and IRAS 10197, one can see some very striking similarities. Both images reveal the presence of an S-shaped envelope with a resolved central dusty torus. The central

torus of IRAS 10197 is also tilted with respect to the tips of the S-shaped structure, as noted by Ueta et al. (2007). These authors estimated the tilt to be $\sim 46^\circ$. Some images of IRAS 10197 were obtained with VISIR in 2005 December, two-and-a-half years prior to our observations. We retrieved and reduced these data to analyse them. The orientation of the torus appears to be exactly the same as the one we observed. Assuming a distance to IRAS 10197 of 2 kpc, an angular extension of the S-shaped structure of ~ 2.5 arcsec and an expansion of 30 km s^{-1} (Sahai et al. 1999), the dynamical age of this structure is ~ 800 yr. The torus would thus need to precess with a rate of $\sim 0.06 \text{ deg yr}^{-1}$ to explain the S-shaped structure. Such a precession rate is almost impossible to detect with the observations we have.

It thus appears that we cannot explain the observed S-shaped structures with a precession of the central tori. This could be due to the fact that either we underestimated the dynamical age of the nebula or another mechanism is responsible for the S-shaped structure. A more plausible explanation is that the S-shaped structure is not due to the precession of the torus itself, but to precessing outflows inside this torus. The presence of such outflows has been observed in the PN NGC 6302 (Meaburn et al. 2008), which has a morphology very similar to those of IRAS 10197 and IRAS 17441. These outflows are Hubble-type, which means that their velocity is proportional to the distance from the source. A torus similar to the ones observed in the core of these objects is also seen in the core of NGC 6302 (Peretto et al. 2007). The properties of such outflows can be theoretically described by a sudden ejection of material, a ‘bullet’ as described by Dennis et al. (2008). Such bullets naturally account for multipolar flows, that could arise naturally from the fragmentation of an explosively driven polar directed shell. It is thus likely that the S-shaped observed in IRAS 17441 and IRAS 10197 is due to high-speed outflows triggered at the end of the AGB phase or the beginning of the PPN phase, likely during an explosive event.

6.4 Chemistry and morphology

Amongst the PPNe and water fountains clearly resolved in our survey, 18 have a known dust chemistry: oxygen, carbon-rich or a dual dust chemistry with both carbonaceous and oxygenous dust grains in their envelopes. For the oxygen-rich sources, we find that 10 out of 11 are bipolar or multipolar, while the remaining one is elliptical. For the carbon-rich sources, we find that two are bipolar or multipolar and two elliptical. The three objects with a dual dust chemistry are multipolar or bipolar. This is in agreement with the recent work by Guzman-Ramirez et al. (2011), which shows a strong correlation between dual dust chemistry and the presence of an equatorial overdensity. The dual dust chemistry could be due either to the formation of PAHs in an oxygen-rich torus after CO photodissociation or to the presence of a long-lived O-rich disc formed before the star turned carbon-rich due to the third dredge-up.

In their mid-infrared catalogue, Meixner et al. (1999) used a different morphological classification and found that most of the elliptical source they resolved are O-rich, while the toroidal ones tend to be C-rich. Stanghellini et al. (2007) also studied the correlation between dust composition and morphologies. They determined, from a study of 41 Magellanic Clouds PNe, that all PNe with O-rich dust are bipolar or highly asymmetric. Our study agrees with this last finding, and it seems that O-rich PPNe appear to be bipolar or multipolar. As discussed by De Marco (2009), the low C/O ratio of these bipolar nebulae could be due to the interaction with

a binary companion during a common envelope phase or, in the case of single star evolution, results from conversion of carbon to nitrogen. The common phase interaction will lead to the ejection of the envelope earlier than in the single star evolution scenario, leading to a less efficient dredge-up of carbon, and thus a lower C/O ratio (Izzard et al. 2006). The conversion of carbon to nitrogen occurs for massive AGB stars with the hot bottom burning process. It is thus likely that the bipolar PPNe have progenitor with larger masses than the elliptical ones. This is in agreement with the work by Corradi & Schwartz (1995), who showed that bipolar PNe tend to have a higher progenitor mass. Soker (1998) proposed that this could be explained in the paradigm of binary system progenitors, as primaries that undergo a common envelope phase, and thus become bipolar, tend to have a higher mass.

7 CONCLUSIONS

We imaged 93 evolved stars and nebulae in the mid-infrared using VISIR/VLT, T-Recs/*Gemini-South* and Michelle/*Gemini-North*. Our observed sample contains all the post-AGB stars observable from Paranal with an *IRAS* 12 μm flux density larger than 10 Jy, including PPNe, RCrB, RV Tauri stars and water fountains. The sample also includes some 10 AGB stars, four PNe, four massive evolved stars, one H II region and a Be star.

These observations allowed us to resolve 34 objects, displaying a wealth of different structures, such as resolved central cores, dark central lanes, detached shells, S-shaped outflows. None of the AGB and RV Tauri stars appears to be resolved, indicating that no bright mid-infrared extended dust shells are present around these objects. Circular detached shells are resolved around two massive evolved stars.

We observed two kind of PPNe.

(i) PPNe with a dense central core, in the form of a bright central source or a dark lane, resolved or not. All these objects are bipolar or multipolar and their SEDs display a near-infrared excess due to hot dust from a dense structure in the core of the object.

(ii) PPNe with a detached shell or a visible central star. These objects are all elliptical and have a two peaked SED.

None of the PPNe appears to be circular, while a significant fraction of PNe, the evolutionary phase after the PPN phase, are known to be spherical. This is certainly a sample bias, as we selected bright mid-infrared stars. Spherical PPNe have no central torus/disc emitting in this wavelength range. At the end of the AGB phase, their envelope is ejected and rapidly cools down while expanding, and thus starts emitting at longer wavelengths and becomes brighter at longer wavelengths. Such detached shells are actually observed in the far-infrared with the *Herschel Space Observatory*.

Precession of the central torii has been proposed to explain the S-shaped morphology of two of the objects we observed, IRAS 10197 and IRAS 17441. Using observations from different epochs, we do not see any sign of such a precession. We propose that the multipolar structures observed in the envelopes of these objects are due to outflows inside the torii, in a scenario similar to the one proposed by Sahai & Trauger (1998).

A large fraction of the dust in galaxies may be produced during the late stages of the evolution of low- and intermediate-mass stars. This dust is ejected to the ISM during the PPN phase. Our observations show the existence of two paths for this dust ejection, via a detached shell or an expanding torus. To better understand the importance of PPNe for the life cycle of dust, it would be interesting to study how the dust production by these objects is affected by these different

paths. Spatially resolved mid-infrared spectra of these sources will allow us to study the dust composition at different locations in these PPNe and thus to better understand the dust evolution during the PPNe phase.

ACKNOWLEDGMENTS

EL thanks the ESO staff in Paranal, who helped in making these observations successful. MM acknowledges an Origin Fellowship. RSz acknowledges support from grant N203 511838 from Polish MNiSW. Fits and postscript images of the nebula will be made available publically via the Torun post-AGB catalogue data base at <http://www.ncac.torun.pl/postagb2>.

REFERENCES

- Bains I., Gledhill T. M., Yates J. A., Richards A. M. S., 2003, *MNRAS*, 338, 287
- Balick B., 1987, *AJ*, 94, 671
- Balick B., Frank A., 2002, *ARA&A*, 40, 439
- Balick B., Preston H. L., Icke V., 1987, *AJ*, 94, 1641
- Blöcker T., Balega Y., Hofmann K.-H., Lichtenthaler J., Osterbart R., Weigelt G., 1999, *A&A*, 348, 805
- Bryce M., Mellema G., 1999, *MNRAS*, 309, 731
- Bujarrabal V., Castro-Carrizo A., Alcolea J., Sánchez Contreras C., 2001, *A&A*, 377, 868
- Bujarrabal V., Castro-Carrizo A., Alcolea J., Neri R., 2005, *A&A*, 441, 1031
- Chesneau O. et al., 2006, *A&A*, 455, 1009
- Chesneau O. et al., 2007, *A&A*, 473, L29
- Clayton G. C., 1996, *PASP*, 108, 225
- Clube K. L., Gledhill T. M., 2004, *MNRAS*, 355, L17
- Cohen M. et al., 1975, *ApJ*, 196, 179
- Cohen M., Van Winckel H., Bond H. E., Gull T. R., 2004, *AJ*, 127, 2362
- Corradi R. L. M., Schwartz H. E., 1995, *A&A*, 293, 871
- De Marco O., 2009, *PASP*, 121, 316
- De Marco O., Barlow M. J., Cohen M., 2002, *ApJ*, 574, L83
- de Ruyter S., van Winckel H., Dominik C., Waters L. B. F. M., Dejonghe H., 2005, *A&A*, 435, 161
- de Ruyter S., van Winckel H., Maas T., Lloyd Evans T., Waters L. B. F. M., Dejonghe H., 2006, *A&A*, 448, 641
- Deacon R. M., Chapman J. M., Green A. J., Sevenster M. N., 2007, *ApJ*, 658, 1096
- Dennis T. J., Cunningham A. J., Frank A., Balick B., Blackman E. G., Mitran S., 2008, *ApJ*, 679, 1327
- Deroo P. et al., 2006, *A&A*, 450, 181
- Engels D., 2002, *A&A*, 388, 252
- Epchtein N., Le Bertre T., Lepine J. R. D., Marques Dos Santos P., Matsuura O. T., Picazzio E., 1987, *A&AS*, 71, 39
- Frank A., Mellema G., 1994, *ApJ*, 430, 800
- García-Hernández D. A., Manchado A., García-Lario P., Cañete A. B., Acosta-Pulido J. A., García A. M., 2006, *ApJ*, 640, 829
- García-Lario P., Manchado A., Pych W., Pottasch S. R., 1997, *A&AS*, 126, 479
- Gielen C. et al., 2009, *A&A*, 508, 1391
- Gledhill T. M., 2005, *MNRAS*, 356, 883
- Gledhill T. M., Takami M., 2001, *MNRAS*, 328, 266
- Gledhill T. M., Chrysostomou A., Hough J. H., Yates J. A., 2001, *MNRAS*, 322, 321
- Gledhill T. M., Witt A. N., Vijn U. P., Davis C. J., 2009, *MNRAS*, 392, 1217
- Gustafsson B., Ryde N., 1996, preprint (arXiv:astro-ph/9610261)
- Guzman-Ramirez L., Zijlstra A. A., Níchuimín R., Gesicki K., Lagadec E., Miller T. J., Woods P. M., 2011, *MNRAS*, 414, 1667
- Harrington J. P., Lane N. J., White S. M., Borkowski K. J., 1997, *AJ*, 113, 2147
- Henize K. G., 1976, *ApJS*, 30, 491

- Hony S., Waters L. B. F. M., Tielens A. G. G. M., 2002, *A&A*, 390, 533
 Hony S., Tielens A. G. G. M., Waters L. B. F. M., de Koter A., 2003, *A&A*, 402, 211
 Hora J. L., Deutsch L. K., Hoffmann W. F., Fazio G. G., 1996, *AJ*, 112, 2064
 Hrivnak B. J., Lu W., Loewe K., Woodsworth A. W., Morris S. C., Bohlender D., Scarfe C. D., 2010, *BAAS*, 42, 471
 Humphreys R. M. et al., 1997, *AJ*, 114, 2778
 Imai H., Obara K., Diamond P. J., Omodaka T., Sasao T., 2002, *Nat*, 417, 829
 Izzard R. G., Dray L. M., Karakas A. I., Lugaro M., Tout C. A., 2006, *A&A*, 460, 565
 Jura M., Werner M. W., 1999, *ApJ*, 525, L113
 Jura M., Chen C., Plavchan P., 2002, *ApJ*, 574, 963
 Justanont K., Barlow M. J., Skinner C. J., Roche P. F., Aitken D. K., Smith C. H., 1996, *A&A*, 309, 612
 Kerschbaum F. et al., 2010, *A&A*, 518, L140
 Kwok S., Purton C. R., Fitzgerald P. M., 1978, *ApJ*, 219, L125
 Kwok S., Volk K. M., Hrivnak B. J., 1989, *ApJ*, 345, L51
 Kwok S., Su K. Y. L., Hrivnak B. J., 1998, *ApJ*, 501, L117
 Kwok S., Hrivnak B. J., Su K. Y. L., 2000, *ApJ*, 544, L149
 Kwok S., Volk K., Hrivnak B. J., 2002, *ApJ*, 573, 720
 Lagadec E., 2005, PhD thesis
 Lagadec E., de Freitas Pacheco J. A., Mékarnia D., 2004, in Meixner M., Kastner J. H., Balick B., Soker N., eds, *ASP Conf. Ser. Vol. 313, Asymmetrical Planetary Nebulae III*. Astron. Soc. Pac., San Francisco, p. 371
 Lagadec E., Mékarnia D., de Freitas Pacheco J. A., Dougados C., 2005, *A&A*, 433, 553
 Lagadec E. et al., 2006, *A&A*, 448, 203
 Lagadec E., Chesneau O., Zijlstra A. A., Matsuura M., Mékarnia D., 2007, *The Messenger*, 117, 12
 Lagage P. O. et al., 2004, *The Messenger*, 117, 123
 Likkell L., Morris M., 1988, *ApJ*, 329, 914
 Manchado A., 1997, *Planet. Nebulae*, 180, 184
 Matsuura M. et al., 2004, *ApJ*, 604, 791
 Matsuura M. et al., 2006, *ApJ*, 646, L123
 Maun N., Huggins P. J., 2006, *A&A*, 452, 257
 Meaburn J., Lloyd M., Vaytet N. M. H., López J. A., 2008, *MNRAS*, 385, 269
 Meixner M. et al., 1993, *ApJ*, 411, 266
 Meixner M. et al., 1999, *ApJS*, 122, 221
 Mékarnia D., Rouan D., Tessier E., Dougados C., Lefevre J., 1998, *A&A*, 336, 648
 Miszalski B., Acker A., Parker Q. A., Moffat A. F. J., 2009, *A&A*, 505, 249
 Miszalski B., Corradi R. L. M., Jones D., Santander García M., Rodríguez-Gil P., Rubio-Díez M. M., 2011, in Zijlstra A. A., Lykou F., McDonald I., Lagadec E., eds, *Asymmetric Planetary Nebulae 5 conf*. Jodrell Bank Centre for Astrophysics
 Miyata T., Katata H., Okamoto Y. K., Onaka T., Sako S., Honda M., Yamashita T., Murakawa K., 2004, *A&A*, 415, 179
 Molster F. J. et al., 1999, *A&A*, 350, 163
 Osterbart R., Langer N., Weigelt G., 1997, *A&A*, 325, 609
 Parker Q. A. et al., 2006, *MNRAS*, 373, 79
 Peretto N., Fuller G., Zijlstra A., Patel N., 2007, *A&A*, 473, 207
 Sahai R., 2002, *Rev. Mex. Astron. Astrofís. Conf. Ser.*, 13, 133
 Sahai R., Trauger J. T., 1998, *AJ*, 116, 1357
 Sahai R., Zijlstra A., Bujarrabal V., te Lintel Hekkert P., 1999, *AJ*, 117, 1408
 Sahai R., Nyman L.-Å., Wootten A., 2000, *ApJ*, 543, 880
 Sahai R., Morris M., Sánchez Contreras C., Claussen M., 2007, *AJ*, 134, 2200
 Sánchez Contreras C., Gil de Paz A., Sahai R., 2004, *ApJ*, 616, 519
 Sánchez Contreras C., Le Mignant D., Sahai R., Gil de Paz A., Morris M., 2007, *ApJ*, 656, 1150
 Shibata K. M., Tamura S., Deguchi S., Hirano N., Kameya O., Kasuga T., 1989, *ApJ*, 345, L55
 Siódmiak N., Meixner M., Ueta T., Sugerman B. E. K., Van de Steene G. C., Szczerba R., 2008, *ApJ*, 677, 382
 Soker N., 1998, *ApJ*, 496, 833
 Stanghellini L., García-Lario P., García-Hernández D. A., Perea-Calderón J. V., Davies J. E., Manchado A., Villaver E., Shaw R. A., 2007, *ApJ*, 671, 1669
 Starck J.-L., Bijaoui A., Lopez B., Perrier C., 1994, *A&A*, 283, 349
 Su K. Y. L., Hrivnak B. J., Kwok S., 2001, *AJ*, 122, 1525
 Su K. Y. L., Hrivnak B. J., Kwok S., Sahai R., 2003, *AJ*, 126, 848
 Suárez O., Gómez J. F., Miranda L. F., Torrelles J. M., Gómez Y., Anglada G., Morata O., 2009, *A&A*, 505, 217
 Szczerba R., Siódmiak N., Stasińska G., Borkowski J., 2007, *A&A*, 469, 799
 Tafoya D., Gómez Y., Patel N. A., Torrelles J. M., Gómez J. F., Anglada G., Miranda L. F., de Gregorio-Monsalvo I., 2009, *ApJ*, 691, 611
 Tiffany C., Humphreys R. M., Jones T. J., Davidson K., 2010, *AJ*, 140, 339
 Tuthill P. G., Lloyd J. P., 2007, *Sci*, 316, 247
 Tuthill P. G., Men'shchikov A. B., Schertl D., Monnier J. D., Danchi W. C., Weigelt G., 2002, *A&A*, 389, 889
 Tuthill P. G., Monnier J. D., Lawrance N., Danchi W. C., Owocicki S. P., Gayley K. G., 2008, *ApJ*, 675, 698
 Ueta T., Meixner M., Bobrowsky M., 2000, *ApJ*, 528, 861
 Ueta T., Murakawa K., Meixner M., 2007, *AJ*, 133, 1345
 van de Steene G. C. M., Pottasch S. R., 1993, *A&A*, 274, 895
 van Loon J. T., Molster F. J., Van Winckel H., Waters L. B. F. M., 1999, *A&A*, 350, 120
 van Winckel H., 2003, *ARA&A*, 41, 391
 van Winckel H. et al., 2009, *A&A*, 505, 1221
 Verhoelst T., Waters L. B. F. M., Verhoeff A., Dijkstra C., van Winckel H., Pel J. W., Peletier R. F., 2009, *A&A*, 503, 837
 Volk K., Hrivnak B. J., Su K. Y. L., Kwok S., 2006, *ApJ*, 651, 294
 Volk K., Kwok S., Hrivnak B. J., 2007, *ApJ*, 670, 1137
 Wallerstein G., 2002, *PASP*, 114, 689
 Waters L. B. F. M. et al., 1998a, *A&A*, 331, L61
 Waters L. B. F. M. et al., 1998b, *Nat*, 391, 868
 Weintraub D. A., Huard T., Kastner J. H., Gatley I., 1998, *ApJ*, 509, 728

APPENDIX A: TABLES

Table A1. Log of the observation, with the object Right Ascension, Declination, Date of the observations, telescope used (VLT = Very Large Telescope, GN = *Gemini-North*, GS = *Gemini-South*), instrument used (B = VISIR burst mode, N = VISIR normal mode, M = Michelle, T = T-Recs), wavelength of the observations in μm , equivalent width of the filter used in μm , and properties of the object (PPN = proto-planetary nebula, WF = water fountain, MES = Massive Evolved Star, RV Tau = RV Tauri star, PN = planetary nebula).

IRAS name	RA	Dec.	Date. telescope, instrument	λ ($\Delta\lambda$)	Properties
IRAS 00245–0652	00 27 06.4	−06 36 16.9	01 Jul 08, VLT, B	8.59 (0.42)	AGB
			01 Jul 08, VLT, B	11.85 (2.34)	
			01 Jul 08, VLT, B	12.81 (0.21)	
IRAS 00477–4900	00 50 02.5	−48 43 47.0	01 Jul 08, VLT, B	8.59 (0.42)	AGB
			01 Jul 08, VLT, B	11.85 (2.34)	
			01 Jul 08, VLT, B	12.81 (0.21)	
IRAS 01037+1219 (CIT 3)	01 06 26.0	+12 35 53.0	29 Jun 08, VLT, B	8.59 (0.42)	AGB
			29 Jun 08, VLT, B	11.85 (2.34)	
			29 Jun 08, VLT, B	12.81 (0.21)	
IRAS 01246–3248 (R Scl)	01 26 58.1	−32 32 35.5	29 Jun 08, VLT, B	8.59 (0.42)	AGB
			29 Jun 08, VLT, B	11.85 (2.34)	
			29 Jun 08, VLT, B	12.81 (0.21)	
IRAS 01438+1850	01 46 35.3	+19 05 03.7	01 Jul 08, VLT, B	8.59 (0.42)	AGB
			01 Jul 08, VLT, B	11.85 (2.34)	
			01 Jul 08, VLT, B	12.81 (0.21)	
IRAS 02270–2619 (R For)	02 29 15.3	−26 05 55.7	29 Jun 10, VLT, B	8.59 (0.42)	AGB
			29 Jun 10, VLT, B	11.85 (2.34)	
			29 Jun 10, VLT, B	12.81 (0.21)	
IRAS 05113+1347 (GLMP 88)	05 14 07.8	+13 50 28.3	09 Oct 07, VLT, N	8.59 (0.42)	PPN
			09 Oct 07, VLT, N	11.85 (2.34)	
			09 Oct 07, VLT, N	12.81 (0.21)	
IRAS 05341+0852	05 36 55.1	+08 54 08.7	17 Nov 07, VLT, N	8.59 (0.42)	PPN
			17 Nov 07, VLT, N	11.85 (2.34)	
			17 Nov 07, VLT, N	12.81 (0.21)	
IRAS 06176–1036 (Red Rectangle)	06 19 58.2	−10 38 14.7	27 Dec 05, GN, M	7.90 (0.42)	PPN
			27 Dec 05, GN, M	8.80 (2.34)	
			27 Dec 05, GN, M	11.60 (0.21)	
			27 Dec 05, GN, M	12.50 (0.21)	
			27 Dec 05, GN, M	18.10 (0.21)	
IRAS 06530–0213	06 55 31.8	−02 17 28.3	17 Nov 07, VLT, N	8.59 (0.42)	PPN
			17 Nov 07, VLT, N	11.85 (2.34)	
			17 Nov 07, VLT, N	12.81 (0.21)	
IRAS 07134+1005	07 16 10.3	+09 59 48.0	11 Dec 07, VLT, N	8.59 (0.42)	PPN
			11 Dec 07, VLT, N	11.85 (2.34)	
			11 Dec 07, VLT, N	12.81 (0.21)	
			19 Dec 05, GN, M	8.80 (0.42)	PPN
			19 Dec 05, GN, M	11.60 (2.34)	
			19 Dec 05, GN, M	12.50 (0.21)	
IRAS 07284–0940 (RAFGL 1135)	07 30 47.5	−09 46 36.8	14 Feb 08, VLT, N	8.59 (0.42)	RV Tau
			14 Feb 08, VLT, N	11.85 (2.34)	
			14 Feb 08, VLT, N	12.81 (0.21)	
IRAS 07331+0021	07 35 41.2	+00 14 58.0	11 Mar 08, VLT, N	8.59 (0.42)	PPN
			11 Mar 08, VLT, N	11.85 (2.34)	
			11 Mar 08, VLT, N	12.81 (0.21)	
IRAS 07399–1435 (OH 231.8 +4.2)	07 42 16.8	−14 42 52.1	08 Jan 06, GN, M	8.80 (0.42)	PPN
			08 Jan 06, GN, M	9.70 (2.34)	
			08 Jan 06, GN, M	11.60 (0.21)	
			08 Jan 06, GN, M	18.10 (0.21)	
IRAS 07430+1115	07 45 51.4	+11 08 19.6	15 Mar 08, VLT, N	8.59 (0.42)	PPN
			15 Mar 08, VLT, N	11.85 (2.34)	
			15 Mar 08, VLT, N	12.81 (0.21)	
IRAS 08005–2356	08 02 40.7	−24 04 42.7	23 Dec 07, VLT, N	8.59 (0.42)	PPN
			23 Dec 07, VLT, N	11.85 (2.34)	
			23 Dec 07, VLT, N	12.81 (0.21)	

Table A1 – continued

IRAS name	RA	Dec.	Date, telescope, instrument	λ ($\Delta\lambda$)	properties
IRAS 10197–5750 (Roberts 22)	10 21 33.8	–58 05 48.3	21 Mar 08, VLT, N	8.59 (0.42)	PPN
			21 Mar 08, VLT, N	11.85 (2.34)	
			21 Mar 08, VLT, N	12.81 (0.21)	
			07 Apr 04, GS, T	11.30 (0.42)	PPN
IRAS 10215–5916 (AFGL 4106)	10 23 19.5	–59 32 04.8	07 Apr 04, GS, T	18.30 (2.34)	
			18 Apr 05, GS, T	11.30 (0.42)	MES
IRAS 11385–5517	11 40 58.8	–55 34 25.8	18 Apr 05, GS, T	18.30 (2.34)	
			21 Mar 08, VLT, N	8.59 (0.42)	PPN
IRAS 11472–0800	11 49 48.0	–08 17 20.4	21 Mar 08, VLT, N	11.85 (2.34)	
			21 Mar 08, VLT, N	12.81 (0.21)	
			19 Feb 08, VLT, N	8.59 (0.42)	PPN
IRAS 12222–4652 (CD–46 7908)	12 24 53.5	–47 09 07.5	19 Feb 08, VLT, N	11.85 (2.34)	
			19 Feb 08, VLT, N	12.81 (0.21)	
			30 Jun 08, VLT, B	8.59 (0.42)	RV Tau
IRAS 12405–6219	12 43 32.1	–62 36 13.0	30 Jun 08, VLT, B	11.85 (2.34)	
			30 Jun 08, VLT, B	12.81 (0.21)	
			30 Jun 08, VLT, B	8.59 (0.42)	H II
			30 Jun 08, VLT, B	11.85 (2.34)	
IRAS 12584–4837 (V1028 Cen)	13 01 17.8	–48 53 18.7	30 Jun 08, VLT, B	12.81 (0.21)	
			30 Jun 08, VLT, B	8.59 (0.42)	PPN
			30 Jun 08, VLT, B	11.85 (2.34)	
			30 Jun 08, VLT, B	12.81 (0.21)	
IRAS 13462–2807 (WHya)	13 49 02.0	–28 22 03.5	01 Jul 08, VLT, B	8.59 (0.42)	AGB
			01 Jul 08, VLT, B	11.85 (2.34)	
			01 Jul 08, VLT, B	12.81 (0.21)	
IRAS 14316–3920 (V854 Cen)	14 34 49.4	–39 33 19.8	30 Jun 08, VLT, B	8.59 (0.42)	R CrB
			30 Jun 08, VLT, B	11.85 (2.34)	
			30 Jun 08, VLT, B	12.81 (0.21)	
IRAS 14429–4539	14 46 13.7	–45 52 07.8	30 Jun 08, VLT, B	8.59 (0.42)	PPN
			30 Jun 08, VLT, B	11.85 (2.34)	
			30 Jun 08, VLT, B	12.81 (0.21)	
			09 May 04, GS, T	11.30 (0.42)	PN
IRAS 14562–5406 (Hen 2–113)	14 59 53.5	–54 18 07.5	09 May 04, GS, T	18.30 (2.34)	
			29 Jun 08, VLT, B	8.59 (0.42)	WF
IRAS 15103–5754 (GLMP 405)	15 14 18.9	–58 05 20.0	29 Jun 08, VLT, B	11.85 (2.34)	
			29 Jun 08, VLT, B	12.81 (0.21)	
IRAS 15373–5308	15 41 07.4	–53 18 15.0	29 Jun 08, VLT, B	8.59 (0.42)	PPN
			30 Jun 08, VLT, B	11.85 (2.34)	
IRAS 15445–5449	15 48 23.5	–54 58 33.0	01 Jul 08, VLT, B	11.85 (2.34)	WF
			01 Jul 08, VLT, B	12.81 (0.21)	
IRAS 15452–5459	15 49 11.5	–55 08 52.0	01 Jul 08, VLT, B	8.59 (0.42)	PPN
			01 Jul 08, VLT, B	11.85 (2.34)	
IRAS 15469–5311	15 50 43.8	–53 20 43.3	01 Jul 08, VLT, B	8.59 (0.42)	RV Tau
			01 Jul 08, VLT, B	11.85 (2.34)	
			01 Jul 08, VLT, B	12.81 (0.21)	
			29 Jun 08, VLT, B	11.85 (2.34)	PPN
IRAS 15553–5230 (GLMP 440)	15 59 11.4	–52 38 41.0	29 Jun 08, VLT, B	12.81 (0.21)	
			29 Jun 08, VLT, B	8.59 (0.42)	AGB
IRAS 16239–1218 (VOph)	16 26 43.7	–12 25 35.8	01 Jul 08, VLT, B	11.85 (2.34)	
			01 Jul 08, VLT, B	12.81 (0.21)	
			01 Jul 08, VLT, B	8.59 (0.42)	PPN
IRAS 16279–4757	16 31 38.1	–48 04 04.0	29 Jun 08, VLT, B	12.81 (0.21)	
			29 Jun 08, VLT, B	8.59 (0.42)	WF
IRAS 16333–4807	16 37 06.1	–48 13 42.0	29 Jun 08, VLT, B	11.85 (2.34)	
			29 Jun 08, VLT, B	12.81 (0.21)	
			29 Jun 08, VLT, B	8.59 (0.42)	WF
			29 Jun 08, VLT, B	11.85 (2.34)	
IRAS 16342–3814 (Water fountain nebula)	16 37 40.1	–38 20 17.0	29 Jun 08, VLT, B	12.81 (0.21)	
			29 Jun 08, VLT, B	8.59 (0.42)	PPN
IRAS 16559–2957	16 59 08.2	–30 01 40.3	15 Apr 08, VLT, N	11.85 (2.34)	
			15 Apr 08, VLT, N	8.59 (0.42)	PPN
			15 Apr 08, VLT, N	12.81 (0.21)	

Table A1 – *continued*

IRAS name	RA	Dec	Date, telescope, instrument	λ ($\Delta\lambda$)	properties
IRAS 16594–4656 (Water-Lily nebula)	17 03 10.0	–47 00 27.0	01 Jul 08, VLT, B	8.59 (0.42)	PPN
			01 Jul 08, VLT, B	11.85 (2.34)	
			01 Jul 08, VLT, B	12.81 (0.21)	
IRAS 17028–1004 (M2–9)	17 05 37.9	–10 08 34.6	18 Apr 08, VLT, N	8.59 (0.42)	PPN
			18 Apr 08, VLT, N	11.85 (2.34)	
			18 Apr 08, VLT, N	12.81 (0.21)	
IRAS 17047–5650 CPD-56°8032	17 09 00.9	–56 54 47.9	07 Jul 05, GS, T	11.30 (0.42)	PN
			07 Jul 05, GS, T	18.30 (2.34)	
IRAS 17088–4221 (GLMP 520)	17 12 22.6	–42 25 13.0	18 Apr 08, VLT, N	8.59 (0.42)	PPN
			18 Apr 08, VLT, N	11.85 (2.34)	
			18 Apr 08, VLT, N	12.81 (0.21)	
IRAS 17106–3046	17 13 51.8	–30 49 40.7	18 Apr 08, VLT, N	11.85 (2.34)	PPN
			18 Apr 08, VLT, N	12.81 (0.21)	
IRAS 17150–3224 (Cotton Candy nebula)	17 18 19.9	–32 27 21.6	15 Apr 08, VLT, N	8.59 (0.42)	PPN
			15 Apr 08, VLT, N	11.85 (2.34)	
			15 Apr 08, VLT, N	12.81 (0.21)	
			09 Apr 04, GS, T	11.30 (0.42)	
IRAS 17163–3907 Hen 3–1379	17 19 49.3	–39 10 37.9	09 Apr 04, GS, T	18.30 (2.34)	PPN
			29 Jun 08, VLT, B	8.59 (0.42)	
IRAS 17233–4330	17 26 58.6	–43 33 13.6	29 Jun 08, VLT, B	11.85 (2.34)	RV Tau
			29 Jun 08, VLT, B	12.81 (0.21)	
			30 Jun 08, VLT, B	11.85 (2.34)	
IRAS 17243–4348 (LR Sco)	17 27 53.6	–43 50 46.3	30 Jun 08, VLT, B	12.81 (0.21)	RV Tau
			01 Jul 08, VLT, B	8.59 (0.42)	
			01 Jul 08, VLT, B	11.85 (2.34)	
IRAS 17245–3951 (Walnut Nebula)	17 28 04.7	–39 53 44.3	01 Jul 08, VLT, B	12.81 (0.21)	PPN
			21 May 08, VLT, N	11.85 (2.34)	
IRAS 17311–4924 (LSE 76)	17 35 02.5	–49 26 26.3	21 May 08, VLT, N	12.81 (0.21)	PPN
			30 Jun 08, VLT, B	8.59 (0.42)	
			30 Jun 08, VLT, B	11.85 (2.34)	
IRAS 17347–3139 (GLMP 591)	17 38 01.3	–31 40 58.0	30 Jun 08, VLT, B	12.81 (0.21)	PPN
			26 May 08, VLT, N	8.59 (0.42)	
			26 May 08, VLT, N	11.85 (2.34)	
IRAS 17441–2411 (Silkworm nebula)	17 47 08.3	–24 12 59.9	26 May 08, VLT, N	12.81 (0.21)	PPN
			01 Jul 08, VLT, B	8.59 (0.42)	
			01 Jul 08, VLT, B	11.85 (2.34)	
			01 Jul 08, VLT, B	12.81 (0.21)	
			31 May 08, VLT, N	8.59 (0.42)	
			31 May 08, VLT, N	11.85 (2.34)	
IRAS 17516–2525	17 54 43.5	–25 26 27.0	31 May 08, VLT, N	12.81 (0.21)	PPN
			30 Jun 08, VLT, B	8.59 (0.42)	
			30 Jun 08, VLT, B	11.85 (2.34)	
			30 Jun 08, VLT, B	12.81 (0.21)	
IRAS 17530–3348 (AI Sco)	17 56 18.5	–33 48 43.3	30 Jun 08, VLT, B	8.59 (0.42)	RV Tau
			30 Jun 08, VLT, B	11.85 (2.34)	
			30 Jun 08, VLT, B	12.81 (0.21)	
			30 Jun 08, VLT, B	12.81 (0.21)	
IRAS 17534+2603	17 55 25.2	+26 03 59.9	30 Jun 08, VLT, B	11.85 (2.34)	PPN
			21 May 08, VLT, N	8.59 (0.42)	
			21 May 08, VLT, N	11.85 (2.34)	
IRAS 18043–2116	18 07 21.2	–21 16 14.0	21 May 08, VLT, N	12.81 (0.21)	WF
			29 Jun 08, VLT, B	12.81 (0.21)	
IRAS 18071–1727	18 10 06.1	–17 26 34.5	29 Jun 08, VLT, B	8.59 (0.42)	PPN
			21 Jun 08, VLT, N	11.85 (2.34)	
			21 Jun 08, VLT, N	12.81 (0.21)	
IRAS 18095+2704	18 11 30.7	+27 05 15.5	21 Jun 08, VLT, N	12.81 (0.21)	PPN
			22 May 08, VLT, N	8.59 (0.42)	
			22 May 08, VLT, N	11.85 (2.34)	
IRAS 18123+0511	18 14 49.4	+05 12 56.0	22 May 08, VLT, N	12.81 (0.21)	RV Tau
			29 Jun 08, VLT, B	8.59 (0.42)	
			29 Jun 08, VLT, B	11.85 (2.34)	
			29 Jun 08, VLT, B	12.81 (0.21)	

Table A1 – continued

IRAS name	RA	Dec	Date, telescope, instrument	λ ($\Delta\lambda$)	properties
IRAS 18135–1456	18 16 25.6	–14 55 15.0	29 Jun 08, VLT, B	8.59 (0.42)	PPN
			29 Jun 08, VLT, B	11.85 (2.34)	
			29 Jun 08, VLT, B	12.81 (0.21)	
OH 12.8–0.9	18 16 49.2	–18 15 01.8	29 Jun 08, VLT, B	8.59 (0.42)	WF
			29 Jun 08, VLT, B	11.85 (2.34)	
			29 Jun 08, VLT, B	12.81 (0.21)	
IRAS 18184–1302 (MWC 922)	18 21 15.9	–13 01 27.0	21 May 08, VLT, N	8.59 (0.42)	Be
			21 May 08, VLT, N	11.85 (2.34)	
			21 May 08, VLT, N	12.81 (0.21)	
IRAS 18184–1623	18 21 18.9	–16 22 29.0	21 May 08, VLT, N	8.59 (0.42)	PPN
			21 May 08, VLT, N	11.85 (2.34)	
IRAS 18276–1431 (V* V445 Sct)	18 30 30.6	–14 28 55.8	21 Jun 08, VLT, N	8.59 (0.42)	PPN
			21 Jun 08, VLT, N	11.85 (2.34)	
			21 Jun 08, VLT, N	12.81 (0.21)	
			01 Jul 08, VLT, B	8.59 (0.42)	
IRAS 18286–0959	18 31 22.7	–09 57 22.0	01 Jul 08, VLT, B	11.85 (2.34)	PPN
			01 Jul 08, VLT, B	12.81 (0.21)	
			30 Jun 08, VLT, B	8.59 (0.42)	
			30 Jun 08, VLT, B	11.85 (2.34)	
IRAS 18450–0148 (W43A)	18 47 40.8	–01 44 57.0	30 Jun 08, VLT, B	12.81 (0.21)	WF
			01 Jul 08, VLT, B	11.85 (2.34)	
			01 Jul 08, VLT, B	12.81 (0.21)	
IRAS 18460–0151	18 48 42.8	–01 48 40.0	01 Jul 08, VLT, B	8.59 (0.42)	WF
			01 Jul 08, VLT, B	11.85 (2.34)	
			01 Jul 08, VLT, B	12.81 (0.21)	
IRAS 19016–2330	19 04 43.5	–23 26 08.8	30 Jun 08, VLT, B	8.59 (0.42)	PPN
			30 Jun 08, VLT, B	11.85 (2.34)	
			30 Jun 08, VLT, B	12.81 (0.21)	
IRAS 19075+0921	19 09 57.1	+09 26 52.2	21 May 08, VLT, N	8.59 (0.42)	PPN
			21 May 08, VLT, N	11.85 (2.34)	
			21 May 08, VLT, N	12.81 (0.21)	
IRAS 19114+0002 (AFGL 2343)	19 13 58.6	+00 07 31.9	25 Apr 08, VLT, N	8.59 (0.42)	MES
			25 Apr 08, VLT, N	11.85 (2.34)	
			25 Apr 08, VLT, N	12.81 (0.21)	
IRAS 19125+0343 (BD+03 3950)	19 15 01.1	+03 48 42.7	29 Jun 08, VLT, B	8.59 (0.42)	RV Tau
			29 Jun 08, VLT, B	11.85 (2.34)	
			29 Jun 08, VLT, B	12.81 (0.21)	
IRAS 19126–0708 (W Aql)	19 15 23.4	–07 02 49.9	29 Jun 08, VLT, B	8.59 (0.42)	AGB
			29 Jun 08, VLT, B	11.85 (2.34)	
			29 Jun 08, VLT, B	12.81 (0.21)	
			29 Jun 08, VLT, B	12.81 (0.21)	
IRAS 19132–3336 (RY Sgr)	19 16 32.7	–33 31 20.3	29 Jun 08, VLT, B	8.59 (0.42)	R Cbr
			29 Jun 08, VLT, B	11.85 (2.34)	
			29 Jun 08, VLT, B	12.81 (0.21)	
IRAS 19134+2131	19 15 35.2	+21 36 34.0	01 Jul 08, VLT, B	11.85 (2.34)	WF
			01 Jul 08, VLT, B	12.81 (0.21)	
IRAS 19175–0807 (V1420 Aql)	19 20 18.0	–08 02 10.6	30 Jun 08, VLT, B	8.59 (0.42)	AGB
			30 Jun 08, VLT, B	11.85 (2.34)	
			30 Jun 08, VLT, B	12.81 (0.21)	
IRAS 19192+0922	19 21 36.5	+09 27 56.5	21 May 08, VLT, N	8.59 (0.42)	PPN
			21 May 08, VLT, N	11.85 (2.34)	
			21 May 08, VLT, N	12.81 (0.21)	
IRAS 19244+1115 (IRC +10420)	19 26 48.0	+11 21 16.7	21 May 08, VLT, N	8.59 (0.42)	MES
			21 May 08, VLT, N	11.85 (2.34)	
			21 May 08, VLT, N	12.81 (0.21)	
IRAS 19327+3024 (BD+30°3639)	19 34 45.2	+30 30 58.9	26 Aug 05, GN, M	8.80 (0.42)	PN
			26 Aug 05, GN, M	9.70 (2.34)	
			26 Aug 05, GN, M	11.60 (0.21)	
			26 Aug 05, GN, M	18.10 (0.21)	

Table A1 – *continued*

IRAS name	RA	Dec.	Date, telescope, instrument	λ ($\Delta\lambda$)	Properties
IRAS 19343+2926 (Min Footprint)	19 36 18.9	+29 32 50.0	21 May 08, VLT, N	8.59 (0.42)	PPN
			21 May 08, VLT, N	11.85 (2.34)	
			21 May 08, VLT, N	12.81 (0.21)	
IRAS 19374+2359	19 39 35.5	+24 06 27.1	24 Jul 08, VLT, N	8.59 (0.42)	PPN
			24 Jul 08, VLT, N	11.85 (2.34)	
			24 Jul 08, VLT, N	12.81 (0.21)	
IRAS 19386+0155 (V1648 Aql)	19 41 08.3	+02 02 31.3	26 May 08, VLT, N	8.59 (0.42)	PPN
			26 May 08, VLT, N	11.85 (2.34)	
			26 May 08, VLT, N	12.81 (0.21)	
IRAS 19454+2920	19 47 24.8	+29 28 10.8	24 Jul 08, VLT, N	8.59 (0.42)	PPN
			24 Jul 08, VLT, N	11.85 (2.34)	
			24 Jul 08, VLT, N	12.81 (0.21)	
IRAS 19477+2401 (Cloverleaf Nebula)	19 49 54.9	+24 08 53.3	19 Jul 08, VLT, N	8.59 (0.42)	PPN
			19 Jul 08, VLT, N	11.85 (2.34)	
			19 Jul 08, VLT, N	12.81 (0.21)	
IRAS 19480+2504	19 50 08.3	+25 12 00.9	17 Jul 08, VLT, N	8.59 (0.42)	PPN
			17 Jul 08, VLT, N	11.85 (2.34)	
			17 Jul 08, VLT, N	12.81 (0.21)	
IRAS 19500–1709 (V5112 Sgr)	19 52 52.7	–17 01 50.3	25 Apr 08, VLT, N	8.59 (0.42)	PPN
			25 Apr 08, VLT, N	11.85 (2.34)	
			25 Apr 08, VLT, N	12.81 (0.21)	
IRAS 20004+2955	20 02 27.4	+30 04 25.5	21 May 08, VLT, N	8.59 (0.42)	PPN
			21 May 08, VLT, N	11.85 (2.34)	
			21 May 08, VLT, N	12.81 (0.21)	
IRAS 20043+2653 (GLMP 972)	20 06 22.7	+27 02 10.6	17 Jul 08, VLT, N	8.59 (0.42)	PPN
			17 Jul 08, VLT, N	11.85 (2.34)	
			17 Jul 08, VLT, N	12.81 (0.21)	
IRAS 20077–0625	20 10 27.9	–06 16 13.6	25 Apr 08, VLT, N	8.59 (0.42)	PPN
			25 Apr 08, VLT, N	11.85 (2.34)	
			25 Apr 08, VLT, N	12.81 (0.21)	
IRAS 20547+0247 (U Equ)	20 57 16.4	+02 58 44.0	29 Jun 08, VLT, B	8.59 (0.42)	PPN
			29 Jun 08, VLT, B	11.85 (2.34)	
			29 Jun 08, VLT, B	12.81 (0.21)	
IRAS 21032–0024 (RV Aqr)	21 05 51.7	–00 12 40.3	29 Jun 08, VLT, B	8.59 (0.42)	AGB
			29 Jun 08, VLT, B	11.85 (2.34)	
			29 Jun 08, VLT, B	12.81 (0.21)	
IRAS 21282+5050	21 29 58.4	+51 03 59.8	03 Sept 05, GN, M	8.80 (0.42)	PPN
			03 Sept 05, GN, M	9.70 (2.34)	
			03 Sept 05, GN, M	11.60 (0.21)	
			03 Sept 05, GN, M	18.10 (0.21)	
IRAS 22196–4612 (π Gru)	22 22 44.2	–45 56 52.6	30 Jun 08, VLT, B	8.59 (0.42)	AGB
			30 Jun 08, VLT, B	11.85 (2.34)	
			30 Jun 08, VLT, B	12.81 (0.21)	
IRAS 22327–1731 (HM Aqr)	22 35 27.5	–17 15 26.9	30 Jun 08, VLT, B	8.59 (0.42)	PPN
			30 Jun 08, VLT, B	11.85 (2.34)	
			30 Jun 08, VLT, B	12.81 (0.21)	
IRAS 23166+1655 (RAFGL 3068)	23 19 12.4	+17 11 35.4	16 Jul 08, VLT, N	8.59 (0.42)	PPN
			16 Jul 08, VLT, N	11.85 (2.34)	
			16 Jul 08, VLT, N	12.81 (0.21)	

Table A2. MIR spectra: 1: IRAS, 2: ISO

IRAS name	<i>J</i>	<i>H</i>	<i>K_s</i>	<i>F</i> ₁₂	<i>F</i> ₂₅	<i>F</i> ₆₀	<i>F</i> ₁₀₀	MIR spectra
IRAS 00245–0652	1.581	0.621	0.236	1.16e+02	5.90e+01	1.15e+01	4.49e+00	1
IRAS 00477–4900	3.184	2.228	1.862	1.92e+01	1.01e+01	1.44e+00	1.14e+00	1
IRAS 01037+1219	7.437	4.641	2.217	1.16e+03	9.68e+02	2.15e+02	7.21e+01	1,2
IRAS 01246–3248	1.973	0.695	−0.117	1.62e+02	8.21e+01	5.48e+01	2.32e+01	1,2
IRAS 01438+1850	2.016	1.012	0.722	7.67e+01	3.99e+01	6.60e+00	2.80e+00	1
IRAS 02270–2619	4.230	2.537	1.349	2.54e+02	7.53e+01	1.60e+01	5.06e+00	1,2
IRAS 05113+1347	9.020	8.423	8.171	3.78e+00	1.53e+01	5.53e+00	1.67e+00	1
IRAS 05341+0852	10.009	9.405	9.108	4.51e+00	9.85e+00	3.96e+00	8.01e+00	2
IRAS 06176–1036	6.577	5.145	3.655	4.21e+02	4.56e+02	1.73e+01	6.62e+01	1,2
IRAS 06530–0213	9.651	8.909	8.512	6.11e+00	2.74e+01	1.51e+01	4.10e+00	1
IRAS 07134+1005	6.868	6.708	6.606	2.45e+01	1.17e+02	5.01e+01	1.87e+01	1,2
IRAS 07284–0940	4.925	4.269	4.042	1.24e+02	8.84e+01	2.66e+01	9.54e+00	1
IRAS 07331+0021	5.816	5.322	4.940	1.53e+01	6.81e+01	1.85e+01	3.68e+00	1
IRAS 07399–1435	9.863	8.281	6.546	1.90e+01	2.26e+02	5.48e+02	2.94e+01	1,2
IRAS 07430+1115	8.836	8.211	7.766	7.68e+00	2.99e+01	1.07e+01	2.53e+00	1
IRAS 08005–2356	7.974	6.923	5.685	1.80e+01	5.18e+01	2.98e+01	1.04e+01	1
IRAS 10197–5750	9.877	8.966	7.399	2.00e+02	1.09e+03	5.88e+02	2.73e+02	1,2
IRAS 10215–5916	4.406	3.432	2.970	2.01e+02	1.76e+03	8.51e+02	1.81e+02	1,2
IRAS 11385–5517	5.947	5.138	3.991	9.26e+01	1.38e+02	1.93e+02	1.04e+02	1,2
IRAS 11472–0800	9.657	9.047	8.630	1.14e+01	1.42e+01	1.78e+00	1.00e+00	1
IRAS 12222–4652	6.941	6.380	5.338	3.25e+01	3.32e+01	7.99e+00	2.41e+00	1
IRAS 12405–6219	16.689	13.928	11.689	1.66e+01	1.09e+02	2.51e+02	4.30e+02	1
IRAS 12584–4837	10.177	9.424	7.805	3.61e+01	4.88e+01	1.30e+01	3.31e+00	1,2
IRAS 13462–2807	−1.737	−2.689	−3.215	4.20e+03	1.19e+03	1.95e+02	7.22e+01	1,2
IRAS 14316–3920	6.106	5.695	4.875	2.30e+01	7.82e+00	1.51e+00	1.03e+00	1
IRAS 14429–4539	10.636	9.818	9.133	1.46e+01	3.33e+01	1.36e+01	2.91e+00	1
IRAS 14562–5406	9.821	8.934	7.531	9.24e+01	3.10e+02	1.77e+02	7.13e+01	1,2
IRAS 15103–5754	15.191	12.718	10.643	1.08e+01	1.02e+02	1.26e+02	1.03e+02	1
IRAS 15373–5308	15.037	11.664	8.756	3.80e+01	5.62e+01	4.25e+01	1.18e+02	1
IRAS 15445–5449	15.315	13.723	12.982	6.88e+00	8.72e+01	1.13e+03	2.18e+03	1
IRAS 15452–5459	11.034	8.837	6.973	8.71e+01	2.43e+02	2.74e+02	4.01e+02	1,2
IRAS 15469–5311	7.190	6.235	4.967	4.88e+01	4.21e+01	1.55e+01	2.78e+02	1
IRAS 15553–5230	13.380	11.534	9.859	9.99e+00	7.00e+01	4.96e+01	2.83e+02	1,2
IRAS 16239–1218	3.972	2.566	1.731	2.90e+01	8.35e+00	1.99e+00	1.66e+00	1
IRAS 16279–4757	8.660	6.605	5.490	4.30e+01	2.68e+02	1.63e+02	2.65e+02	1,2
IRAS 16333–4807	11.353	10.504	10.184	9.33e+00	4.30e+01	8.93e+01	1.13e+02	1
IRAS 16342–3814	11.608	10.589	9.569	1.62e+01	2.00e+02	2.90e+02	1.39e+02	1,2
IRAS 16559–2957	11.596	10.713	9.347	9.17e+00	3.24e+01	1.64e+01	4.18e+00	1
IRAS 16594–4656	9.881	9.002	8.260	4.49e+01	2.98e+02	1.31e+02	3.44e+01	1,2
IRAS 17028–1004	11.198	9.177	6.996	5.05e+01	1.10e+02	1.24e+02	7.58e+01	1
IRAS 17047–5650	9.513	8.499	6.862	1.43e+02	2.57e+02	1.99e+02	9.20e+01	1,2
IRAS 17088–4221	13.208	11.891	11.328	4.27e+01	1.28e+02	1.07e+02	3.69e+01	1
IRAS 17106–3046	9.975	8.906	8.316	4.01e+00	6.24e+01	5.12e+01	1.73e+01	1
IRAS 17150–3224	11.099	10.219	9.391	5.79e+01	3.22e+02	2.68e+02	8.24e+01	1,2
IRAS 17163–3907	4.635	3.021	2.407	1.24e+03	1.15e+03	6.63e+02	5.92e+02	1
IRAS 17233–4330	10.423	9.592	8.371	1.70e+01	1.34e+01	3.67e+00	3.21e+01	1
IRAS 17243–4348	8.035	7.358	6.462	1.08e+01	8.77e+00	3.69e+00	5.41e+00	1

Table A2 – *continued*

IRAS name	<i>J</i>	<i>H</i>	<i>K_s</i>	<i>F</i> ₁₂	<i>F</i> ₂₅	<i>F</i> ₆₀	<i>F</i> ₁₀₀	MIR spectra
IRAS 17245–3951	11.234	10.375	9.716	3.36e+00	4.47e+01	3.82e+01	9.77e+01	1
IRAS 17311–4924	9.793	9.543	9.203	1.83e+01	1.51e+02	5.87e+01	1.78e+01	1,2
IRAS 17347–3139	15.097	12.932	10.302	1.90e+01	1.00e+02	1.25e+02	2.49e+02	1
IRAS 17441–2411	11.088	10.132	9.380	4.28e+01	1.91e+02	1.06e+02	2.78e+01	1,2
IRAS 17516–2525	8.695	6.850	5.082	5.16e+01	1.16e+02	1.00e+02	2.92e+02	1,2
IRAS 17530–3348	6.864	6.179	5.485	1.76e+01	1.14e+01	2.95e+00	4.68e+01	1
IRAS 17534+2603	4.998	4.239	3.632	9.75e+01	5.45e+01	1.34e+01	6.04e+00	1,2
IRAS 18043–2116	14.546	13.404	13.042	6.60e+00	6.76e+00	1.66e+01	2.37e+02	1
IRAS 18071–1727	15.889	14.149	12.713	2.37e+01	7.66e+01	8.35e+01	3.05e+02	1
IRAS 18095+2704	7.366	6.728	6.438	4.51e+01	1.26e+02	2.78e+01	5.64e+00	1,2
IRAS 18123+0511	7.974	7.399	6.729	1.07e+01	1.10e+01	4.21e+00	1.85e+00	1
IRAS 18135–1456	15.417	13.751	13.130	3.10e+01	1.24e+02	1.58e+02	4.29e+02	1
OH 12.8–0.9	17.041	15.725	11.639	1.16e+01	1.69e+01	1.39e+01	2.89e+02	
IRAS 18184–1302	8.960	7.396	5.704	3.36e+02	5.98e+02	2.53e+02	4.36e+02	1
IRAS 18184–1623	5.136	4.537	4.106	7.00e+01	3.25e+02	1.17e+02	5.84e+02	1
IRAS 18276–1431	11.670	10.810	9.450	2.26e+01	1.32e+02	1.20e+02	3.86e+01	1,2
IRAS 18286–0959	15.431	13.562	12.674	2.49e+01	2.45e+01	1.84e+01	4.05e+02	1
IRAS 18450–0148	16.115	14.794	13.219	2.37e+01	1.04e+02	2.95e+02	2.52e+03	1
IRAS 18460–0151	13.732	13.813	13.435	2.09e+01	3.27e+01	2.77e+02	2.91e+02	
IRAS 19016–2330	12.500	11.343	9.966	1.26e+01	5.75e+01	2.80e+01	9.54e+00	1
IRAS 19075+0921	16.920	15.536	14.666	1.33e+02	1.64e+02	5.49e+01	7.80e+01	
IRAS 19114+0002	5.371	4.998	4.728	3.13e+01	6.48e+02	5.16e+02	1.68e+02	1,2
IRAS 19125+0343	7.903	7.076	5.650	2.89e+01	2.65e+01	7.81e+00	2.80e+01	1
IRAS 19126–0708	1.534	0.238	–0.556	1.58e+03	6.70e+02	1.12e+02	3.60e+01	1,2
IRAS 19132–3336	5.577	5.423	5.139	7.72e+01	2.62e+01	5.43e+00	4.60e+00	1,2
IRAS 19134+2131	16.543	14.926	13.464	5.06e+00	1.56e+01	8.56e+00	3.95e+00	1
IRAS 19175–0807	5.996	3.593	1.828	3.84e+02	1.93e+02	4.79e+01	1.56e+01	1
IRAS 19192+0922	9.449	6.759	4.821	1.27e+02	1.55e+02	4.14e+02	9.78e+00	1
IRAS 19244+1115	5.466	4.544	3.612	1.35e+03	2.31e+03	7.18e+02	1.86e+02	1
IRAS 19327+3024	9.306	9.231	8.108	8.93e+01	2.34e+02	1.62e+02	7.00e+01	1,2
IRAS 19343+2926	9.908	7.929	6.209	1.75e+01	5.98e+01	1.18e+02	6.80e+01	1,2
IRAS 19374+2359	12.038	10.866	9.735	2.36e+01	9.82e+01	7.09e+01	7.68e+02	1
IRAS 19386+0155	7.951	7.069	6.011	1.74e+01	4.74e+01	1.86e+01	3.79e+00	1,2
IRAS 19454+2920	11.853	10.749	10.426	1.73e+01	8.96e+01	5.44e+01	1.47e+01	1,2
IRAS 19477+2401	12.611	10.752	9.606	1.12e+01	5.49e+01	2.71e+01	3.80e+01	1,2
IRAS 19480+2504	15.216	14.036	13.559	2.08e+01	6.79e+01	4.32e+01	2.67e+01	1,2
IRAS 19500–1709	7.228	6.970	6.858	2.78e+01	1.65e+02	7.34e+01	1.82e+01	1,2
IRAS 20004+2955	4.766	4.305	3.793	3.17e+01	3.70e+01	4.66e+00	3.35e+01	1,2
IRAS 20043+2653	17.431	14.870	10.604	1.79e+01	4.20e+01	2.03e+01	7.48e+00	1
IRAS 20077–0625	6.906	3.923	2.059	1.26e+03	1.06e+03	2.16e+02	6.37e+01	1
IRAS 20547+0247	11.561	10.132	8.405	4.55e+01	3.38e+01	1.00e+01	2.84e+00	1
IRAS 21032–0024	4.046	2.355	1.239	3.08e+02	1.16e+02	2.24e+01	8.55e+00	1,2
IRAS 21282+5050	11.504	10.709	9.551	5.10e+01	7.44e+01	3.34e+01	1.50e+01	1,2
IRAS 22196–4612	–0.715	–1.882	–2.351	9.08e+02	4.37e+02	7.73e+01	2.33e+01	1,2
IRAS 22327–1731	8.276	7.609	6.705	5.57e+00	4.66e+00	2.11e+00	1.01e+00	2
IRAS 23166+1655	17.165	15.402	10.379					1

Table A3. Observed fluxes and sizes of objects, position angle of the resolved nebula and name of the associated PSF standard.

IRAS name	λ (μm)	F (Jy)	Source		PA ($^\circ$)	PSF	
			FWHM (arcsec)	Size (arcsec \times arcsec)		FWHM (arcsec)	Name
00245–0652	8.59	73.2	0.26	Unresolved		0.24	HD 196321
	11.85	82.5	0.33	Unresolved		0.30	
	12.81	84.2	0.38	Unresolved		0.32	
00477–4900	8.59	15.9	0.31	Unresolved		0.30	HD 196321
	11.85	13.8	0.31	Unresolved		0.30	
	12.81	12.0	0.32	Unresolved		0.32	
01037+1219	8.59	501.5	0.67	Unresolved (saturated)		0.23	HD 198048
	11.85	709.2	0.63	Unresolved (saturated)		0.30	
	12.81	789.4	0.47	Unresolved (saturated)		0.32	
01246–3248	8.59	170.9	0.33	Unresolved (saturated)		0.23	HD 198048
	11.85	132.3	0.37	Unresolved (saturated)		0.30	
	12.81	78.4	0.33	Unresolved		0.33	
01438+1850	8.59	56.0	0.72	Unresolved (saturated)		0.43	HD 196321
	11.85	63.8	0.52	Unresolved (saturated)		0.30	
	12.81	53.9	0.33	Unresolved		0.32	
02270–2619	8.59	164.4	0.33	Unresolved		0.30	HD 196321
	11.85	131.5	0.37	Unresolved		0.30	
	12.81	71.9	0.33	Unresolved		0.32	
05113+1347	8.59	0.8	0.52	Unresolved		0.55	HD 31421
	11.85	3.8	0.57	Unresolved		0.49	
	12.81	4.1	0.51	Unresolved		0.44	
05341+0852	8.59	2.4	0.32	Unresolved		0.26	HD 39400
	11.85	5.0	0.34	Unresolved		0.30	
	12.81	4.8	0.36	Unresolved		0.33	
06176–1036	7.90	365.7	0.31	3.3 \times 5.9		0.22	HD 59381
	8.80	313.1	0.31	3.3 \times 5.9		0.22	
	11.60	375.7	0.36	3.3 \times 5.9		0.26	
	12.50	408.9	0.34	3.3 \times 5.9		0.28	
	18.10	251.9	0.47	3.3 \times 5.9		0.38	
06530–0213	8.59	1.4	0.35	Unresolved		0.28	HD 49293
	11.85	6.1	0.67	Unresolved		0.13	
	12.81	1.5	0.05	Unresolved		0.32	
07134+1005	8.59	4.9	0.25	4.8 \times 4.6	N/A	0.23	HD 58207
	11.85	14.6	1.19	5.0 \times 4.7	27	0.34	
	12.81	16.3	1.46	4.8 \times 4.7	23	0.37	
07284–0940	8.59	98.2	0.28	Unresolved		0.30	HD 59381
	11.85	126.7	0.33	Unresolved		0.34	
	12.81	103.4	0.36	Unresolved		0.33	
07331+0021	8.59	6.5	0.30	Unresolved		0.26	HD 61935
	11.85	16.7	0.36	Unresolved		0.35	
	12.81	17.5	0.40	Unresolved		0.39	
07399–1435	8.80	18.3	0.34	4.1 \times 6.1		0.34	Alpha CMa
	9.70	6.3	0.36	2.6 \times 4.3		0.36	
	11.60	18.2	0.54	4.3 \times 6.7		0.33	
	18.10	22.6	0.81	5.4 \times 6.7		0.41	
	8.59	3.0		Unresolved			
07430+1115	11.85	9.6	0.41	Unresolved		0.32	HD 62721
	12.81	9.7	0.42	Unresolved		0.33	
	8.59	14.0	0.28	Unresolved		0.27	
08005–2356	11.85	16.7	0.34	Unresolved		0.32	HD 67523
	12.81	17.5	0.36	Unresolved		0.33	
	8.59	97.1	0.74	4.4 \times 3.2	44	0.25	
10197–5750	11.85	181.6	0.75	4.9 \times 3.6	42	0.31	HD 91942
	12.81	215.4	0.75	4.7 \times 3.5	42	0.34	
	11.30	216.1	0.72	3.4 \times 3.3	N/A	0.42	
10215–5916	18.30	1395.33	4.01	3.4 \times 3.3	N/A	0.53	Gamma Gru
	8.59	69.3	0.28	Unresolved		0.25	
11385–5517	11.85	86.6	0.31	Unresolved		0.28	HD 102461
	12.81	87.1	0.34	Unresolved		0.33	

Table A4. Observed fluxes and sizes of objects.

11472–0800	8.59		0.30	Unresolved		0.30	HD 99167
	11.85	7.1	0.33	Unresolved		0.32	
	12.81	5.1	0.34	Unresolved		0.36	
12222–4652	8.59	23.2	0.23	Unresolved		0.23	HD 111915
	11.85	28.8	0.28	Unresolved		0.29	
	12.81	24.4	0.33	Unresolved		0.32	
12405–6219	8.59	4.9	0.54	2.3 × 2.1	128	0.23	HD 111915
	11.85	12.7	0.67	3.1 × 2.8	133	0.30	
	12.81	16.7	1.04	3.1 × 2.9	126	0.32	
12584–4837	8.59	27.4	0.26	Unresolved		0.23	HD 111915
	11.85	28.6	0.30	Unresolved		0.30	
	12.81	22.3	0.32	Unresolved		0.32	
13462–28071	8.59	1075.4	0.99	2.3 × 2.0	43	0.27	HD 124294
	11.85	1522.8	1.01	2.2 × 2.0	39	0.31	
	12.81	1527.8	0.76	1.9 × 1.8	45	0.33	
14316–3920	8.59	19.1	0.24	Unresolved		0.24	HD 111915
	11.85	12.5	0.31	Unresolved		0.30	
	12.81	11.6	0.33	Unresolved		0.33	
14429–4539	8.59	10.3	0.32	Unresolved		0.24	HD 111915
	11.85	14.6	0.36	Unresolved		0.30	
	12.81	15.2	0.40	Unresolved		0.33	
14562–5406	11.30	87.1	1.39	6.0 × 4.6	92	0.39	Alpha Cen
	18.30	246.4	1.62	5.6 × 4.4	82	0.55	
15103–5754	8.59	1.0	0.34	1.8 × 1.3	32	0.25	HD 133550
	11.85	5.6	0.52	2.5 × 2.3	32	0.31	
	12.81	13.8	0.53	3.0 × 2.0	32	0.33	
15373–5308	8.59	31.3	0.24	Unresolved		0.24	HD 133774
	11.85	33.8	0.30	Unresolved		0.30	
15445–5449	11.85	3.2	0.32	3.6 × 2.9	−3	0.32	HD 124294
	12.81	6.8	0.51	3.1 × 2.0	1	0.33	
15452–5459	8.59			Nodetection			HD 133774
15469–5311	8.59	40.3	0.24	Unresolved		0.26	HD 124294
	11.85	40.3	0.25	Unresolved		0.31	
	12.81	39.0	0.32	Unresolved		0.33	
15553–5230	11.85		0.52	3.7 × 3.6	91	0.30	HD 133774
	12.81		0.45	3.4 × 3.2	83	0.33	
16239–1218	8.59	30.7	0.25	Unresolved		0.26	HD 124294
	11.85	21.4	0.28	Unresolved		0.31	
	12.81	21.4	0.34	Unresolved		0.33	
16279–4757	8.59	20.2	0.28	6.1 × 4.0	10	0.25	HD 163376
	12.81	30.1	0.42	7.2 × 6.2	7	0.3	
16333–4807	8.59	3.6	0.30	Problem		0.25	HD 163376
	11.85	7.3	0.39	5.0 × 3.7	−7	0.31	
	12.81	13.8	0.43	5.1 × 3.4	−12	0.33	
16342–3814	11.85	7.7	0.83	4.3 × 4.2	79	0.30	HD 163376
	12.81	18.1	0.55	3.6 × 3.4	85	0.33	
16559–2957	8.59	5.2	0.33	Unresolved		0.37	HD 152980
	11.85	8.6	0.36	Unresolved		0.40	
	12.81	10.9	0.41	Unresolved		0.40	
16594–4656	8.59	16.6?	1.73	4.9 × 3.9	84	0.33	HD 124294
	11.85	46.0	1.56	5.9 × 4.5	83	0.30	
	12.81	46.0	1.65	5.2 × 4.2	82	0.32	
17028–1004	8.59	44.7	0.33	Unresolved		0.33	HD 159187
	11.85	48.4	0.36	Unresolved		0.35	
	12.81	56.9	0.38	Unresolved		0.37	
17047–5650	11.30	155.2	0.62	5.6 × 4.6	8	0.40	Eta Sgr
	18.30	179.3	1.10	4.7 × 4.1	10	0.57	
17088–4221	8.59	15.0	0.31	Unresolved		0.30	HD 155066
	11.85	27.0	0.41	Unresolved		0.36	
	12.81	59.1	0.41	Unresolved		0.36	
17106–3046	11.85	2.9	0.51	3.9 × 3.9	N/A	0.33	HD 157236
	12.81	3.7	0.56	4.2 × 3.7	N/A	0.35	

Table A5. Observed fluxes and sizes of objects.

17150–3224	8.59	18.3	0.50	3.7 × 3.5	–36	0.32	HD 159433
	11.85	50.3	0.58	4.2 × 3.6	–58	0.34	
	12.81	81.0	0.56	4.1 × 3.6	–62	0.38	
17163–3907	8.59	253	1.23	5.6 × 5.6	N/A	0.25	HD 163376
	11.85	892	1.53	5.9 × 5.8	N/A	0.30	
	12.81	910	1.52	6.0 × 5.8	N/A	0.33	
17233–4330	11.85	10.4	0.29	Unresolved		0.30	HD 163376
	12.81	10.5	0.33	Unresolved		0.33	
17243–4348	8.59	8.6	0.25	Unresolved		0.24	HD 124294
	11.85	7.8	0.29	Unresolved		0.30	
	12.81	8.6	0.31	Unresolved		0.32	
17245–3951	11.85	2.2	0.47	Unresolved		0.32	HD 161892
	12.81	2.9	0.49	Unresolved		0.35	
17311–4924	8.59	3.9	1.13	3.0 × 2.8	–90	0.24	HD 163376
	11.85	16.8	1.30	5.5 × 5.1	–92	0.30	
	12.81	19.1	1.33	3.8 × 3.6	–88	0.33	
17347–3139	8.59	7.6	0.57	4.1 × 3.5	–42	0.34	HD 159881
	11.85	17.3	0.48	3.9 × 3.1	–41	0.36	
	12.81	30.5	0.52	4.2 × 3.3	–41	0.38	
17441–2411	8.59	12.1	0.71	3.7 × 3.5	16	0.58	HD 196321
	11.85	39.5	0.76	4.2 × 3.9	40	0.30	
	12.81	48.1	0.66	4.0 × 3.6	21	0.33	
17516–2525	8.59	46.6	0.25	Unresolved		0.24	HD 163376
	11.85	42.0	0.29	Unresolved		0.30	
	12.81	42.0	0.33	Unresolved		0.33	
17530–3348	8.59	17.2	0.20	Unresolved		0.22	HD 163376
	11.85	17.0	0.30	Unresolved		0.31	
	12.81	14.3	0.33	Unresolved		0.32	
17534+2603	8.59	85.4	0.34	Unresolved		0.35	HD 163993
	11.85	87.2	0.37	Unresolved		0.42	
	12.81	77.3	0.38	Unresolved		0.39	
18043–2116	12.81	1.5	0.36	Unresolved		0.32	HD 174387
18071–1727	8.59	11.7	0.34	Unresolved		0.33	HD 167036
	11.85	22.2	0.38	Unresolved		0.35	
	12.81	41.5	0.38	Unresolved		0.38	
18095+2704	8.59	18.8	0.39	Unresolved		0.33	HD 169414
	11.85	38.7	0.41	Unresolved		0.35	
	12.81	29.0	0.39	Unresolved		0.41	
18123+0511	8.59	7.3	0.32	Unresolved		0.24	HD 163376
	11.85	8.9	0.30	Unresolved		0.30	
	12.81	8.4	0.31	Unresolved		0.33	
18135–1456	8.59	7.2	0.34	Unresolved		0.23	HD 163376
	11.85	17.9	0.37	Unresolved		0.30	
	12.81	37.0	0.42	Unresolved		0.32	
OH12.8–0.9	8.59	9.3	0.24	Unresolved		0.24	HD 163376
	11.85	9.9	0.31	Unresolved		0.31	
	12.81	19.7	0.34	Unresolved		0.33	
18184–1302	8.59	228.8	0.31	4.0 × 3.5	N/A	0.28	HD 161892
	11.85	292.1	0.09	0.4 × 0.2	N/A	0.32	
	12.81	345.0	0.07	1.2 × 0.8	N/A	0.33	
18184–1623	8.59	1.7	0.41	Unresolved		0.28	HD 168415
	11.85	0.5	0.52	Unresolved		0.31	
18276–1431	8.59	4.4	0.51	2.5 × 2.4	N/A	0.48	HD 181410
	11.85	18.9	0.51	2.7 × 2.6	N/A	0.50	
	12.81	22.3	0.51	2.5 × 2.4	N/A	0.52	
18286–0959	8.59	4.5	0.37	1.6 × 1.5	8	0.24	HD 196321
	11.85	11.9	0.48	3.5 × 2.6	9	0.30	
	12.81	17.4	0.45	2.3 × 2.0	9	0.32	
	8.59	27.0	0.30	Unresolved		0.23	
	11.85	37.0	0.31	Unresolved		0.30	
18450–0148	12.81	62.3	0.35	Unresolved		0.32	HD 161096
	11.85	21.4	0.44	4.3 × 4.1	44	0.31	
	12.81	31.1	0.49	3.7 × 3.3	32	0.32	
18460–0151	8.59	9.2	0.24	Unresolved		0.24	HD 161096
	11.85	16.7	0.31	Unresolved		0.31	
	12.81	24.6	0.28	Unresolved		0.33	

Table A6. Observed fluxes and sizes of objects.

19016–2330	8.59	8.9	0.39	2.0×1.9	N/A	0.23	HD 198048
	11.85	11.8	0.39	2.8×2.2	N/A	0.30	
	12.81	12.8	0.39	2.2×1.6	N/A	0.32	
19075+0921	8.59	92.5	0.34	Unresolved		0.32	HD 178690
	11.85	120.0	0.35	Unresolved		0.34	
	12.81	278.9	0.35	Unresolved		0.34	
19125+0343	8.59	25.2	0.26	Unresolved		0.23	HD 174387
	11.85	27.3	0.29	Unresolved		0.29	
	12.81	22.8	0.33	Unresolved		0.32	
19126–0708	8.59	644.4	0.79	Unresolved (saturated)		0.23	HD 174387
	11.85	744.3	0.64	Unresolved (saturated)		0.30	
	12.81	810.6	0.51	Unresolved (saturated)		0.32	
19114+0002	8.59	2.7	0.27	4.0×3.7	N/A	0.26	HD 178131
	11.85	17.1	0.25	5.2×4.9	N/A	0.32	
	12.81	1.7	0.40	5.2×5.1	N/A	0.33	
19132–3336	8.59	47.8	0.24	Unresolved		0.23	HD 163376
	11.85	34.4	0.33	Unresolved		0.30	
	12.81	28.8	0.32	Unresolved		0.32	
19134+2131	11.85	3.9	0.34	Unresolved		0.30	HD 196321
	12.81	6.2	0.37	Unresolved		0.33	
	8.59	309.3	0.54	Unresolved (saturated)		0.23	
19175–0807	11.85	295.9	0.42	Unresolved (saturated)		0.30	HD 163376
	12.81	298.0	0.34	Unresolved		0.34	
	8.59	150.4	0.38	Unresolved		0.31	
19192+0922	11.85	181.9	0.37	Unresolved		0.34	HD 185622
	12.81	159.9	0.38	Unresolved		0.37	
	8.59	611.6	0.51	3.3×3.2	N/A	0.31	
19244+1115	11.85	1655.1	0.52	3.8×3.6	N/A	0.33	HD 183439
	12.81	1099.0	0.54	4.0×3.7	N/A	0.36	
	8.80	53.8	1.85	7.5×6.9	84	0.23	
19327+3024	9.70	58.0	2.05	7.1×6.4	80	0.23	HR 7924
	11.60	104.0	1.03	7.5×6.2	80	0.25	
	18.10	308.0	1.97	7.6×6.7	84	0.38	
	8.59	15.2	0.31	Unresolved		0.30	
19343+2926	11.85	14.3	0.34	Unresolved		0.34	HD 186860
	12.81	16.1	0.36	Unresolved		0.35	
	8.59	18.7	0.86	3.1×2.9	9	0.36	
19374+2359	11.85	21.6	0.88	3.2×3.0	10	0.38	HD 185622
	12.81	24.5	0.91	3.0×3.0	N/A	0.40	
	8.59	14.7	0.39	2.7×2.5	116	0.48	
19386+0155	11.85	18.4	0.46	2.6×2.6	N/A	0.62	HD 185622
	12.81	22.5	0.41	2.2×2.1	113	0.45	
	8.59	4.9	0.46	2.1×1.7	105	0.33	
19454+2920	11.85	16.0	0.52	2.6×2.4	95	0.40	HD 186860
	12.81	25.5	0.49	2.4×2.1	96	0.40	
	8.59	3.3	0.47	Unresolved		0.41	
19477+2401	11.85	11.4	0.49	Unresolved		0.43	HD 186860
	12.81	15.1	0.52	Unresolved		0.45	
	8.59	5.8	0.50	Unresolved		0.62	
19480+2504	11.85	15.5	0.51	Unresolved		0.54	HD 186860
	12.81	22.8	0.51	Unresolved		0.54	
	8.59			problem			
19500–1709	11.85	29.3	1.12	3.2×2.9	85	0.31	HD 188603
	12.81	32.9	1.00	3.0×2.8	87	0.34	
	8.59	12.4	0.35	Unresolved		0.28	
20004+2955	11.85	31.5	0.38	Unresolved		0.33	HD 189577
	12.81	20.9	0.40	Unresolved		0.34	
	8.59	15.3	0.57	Unresolved		0.48	
20043+2653	11.85	12.9	0.53	Unresolved		0.48	HD 189577
	12.81	19.7	0.51	Unresolved		0.48	
	8.59	314.8	0.33	Unresolved		0.38	
20077–0625	11.85	410.3	0.36	Unresolved		0.37	HD 192947
	12.81	405.4	0.36	Unresolved		0.36	
	8.59						

Table A7. Observed fluxes and sizes of objects.

20547+0247	8.59	21.3	0.25	Unresolved		0.23	HD 174387
	11.85	35.7	0.34	Unresolved		0.30	
	12.81	41.7	0.33	Unresolved		0.32	
21032−0024	8.59	230.9	0.42	Unresolved (saturated)		0.24	HD 196321
	11.85	194.9	0.33	Unresolved		0.30	
	12.81	142.8	0.34	Unresolved		0.33	
21282+5050	8.80	30.8	1.84	7.4 × 7.1	−16	0.24	HR 8538
	9.70	31.0	1.77	6.3 × 4.8	−13	0.25	
	11.60	92.3	1.80	7.3 × 5.6	−18	0.27	
	18.10	165.2	1.87	6.3 × 5.1	−20	0.39	
22196−4612	8.59	316.7	0.74	Unresolved (saturated)		0.24	HD 196321
22327−1731	8.59	9.4	0.25	Unresolved		0.23	HD 198048
	11.85	7.5	0.30	Unresolved		0.30	
23166+1655	8.59	433.0	0.57	Unresolved (saturated)		0.37	HD 220009
	11.85	856.7	0.62	Unresolved (saturated)		0.39	
	12.81	942.4	0.56	Unresolved (saturated)		0.40	

Table A8. Morphologies of the resolved targets, dust properties (C = carbon-rich, O = oxygen-rich, C/O = dual dust chemistry).

IRAS name	Other names	MIR morpho	C/O	Type
IRAS 06176−1036	Red Rectangle	Core/bipolar	C/O	PPN
IRAS 07134+1005		Elliptical	C	PPN
IRAS 07399−1435	OH 231.8 +4.2	Core/bipolar	O	PPN
IRAS 10197−5750	Roberts 22	Core/multipolar	C/O	PPN
IRAS 10215−5916	AFGL 4106	Detached shell	C/O	PRSG
IRAS 12405−6219		Asymmetrical		H II
IRAS 14562−5406	Hen 2−113	Tore/elliptical	C/O	PN
IRAS 15103−5754	GLMP 405	Core/bipolar	O	WF
IRAS 15445−5449		Dark lane/bipolar	O	WF
IRAS 15553−5230	GLMP 440	Marginally resolved		PPN
IRAS 16279−4757		Core/multipolar	C/O	PAGB
IRAS 16333−4807		Core/multipolar	O	WF
IRAS 16342−3814	Water fountain nebula	Dark lane/bipolar	O	WF
IRAS 16594−4656	Water-Lily nebula	Core/bipolar	C	PPN
IRAS 17047−5650	CPD-56°8032	Core/bipolar	C/O	PN
IRAS 17106−3046		Marginally resolved	O	PPN
IRAS 17150−3224	Cotton Candy nebula	Core/bipolar	O	PPN
IRAS 17163−3907	Hen 3−1379	Detached shell/spherical	O	PRSG
IRAS 17311−4924	LSE 76	Core/bipolar	C	PPN
IRAS 17347−3139	GLMP 591	Core/multipolar	O	PN
IRAS 17441−2411	Silkworm nebula	Core/multipolar	O	PPN
IRAS 18184−1302	MWC 922	Square		Be
IRAS 18276−1431	V* V445 Sct	Marginally resolved	O	PPN
IRAS 18450−0148	W43A	Core/bipolar	O	WF
IRAS 19016−2330		Marginally resolved		PPN
IRAS 19114+0002	AFGL2343	Detached shell	O	MES
IRAS 19244+1115	IRC +10420	Core/extended	O	MES
IRAS 19327+3024	BD+30°3639	Elliptical		PN
IRAS 19374+2359		Detached shell	O	PPN
IRAS 19386+0155	V1648 Aql	Core/extended		PPN
IRAS 19454+2920		Core/extended	C	PPN
IRAS 19500−1709	V5112 Sgr	Detached shell, no central star	C	PPN
IRAS 20043+2653	GLMP 972	Core/extended		PPN
IRAS 21282+5050		Toroidal	C	PN

APPENDIX B: IMAGES

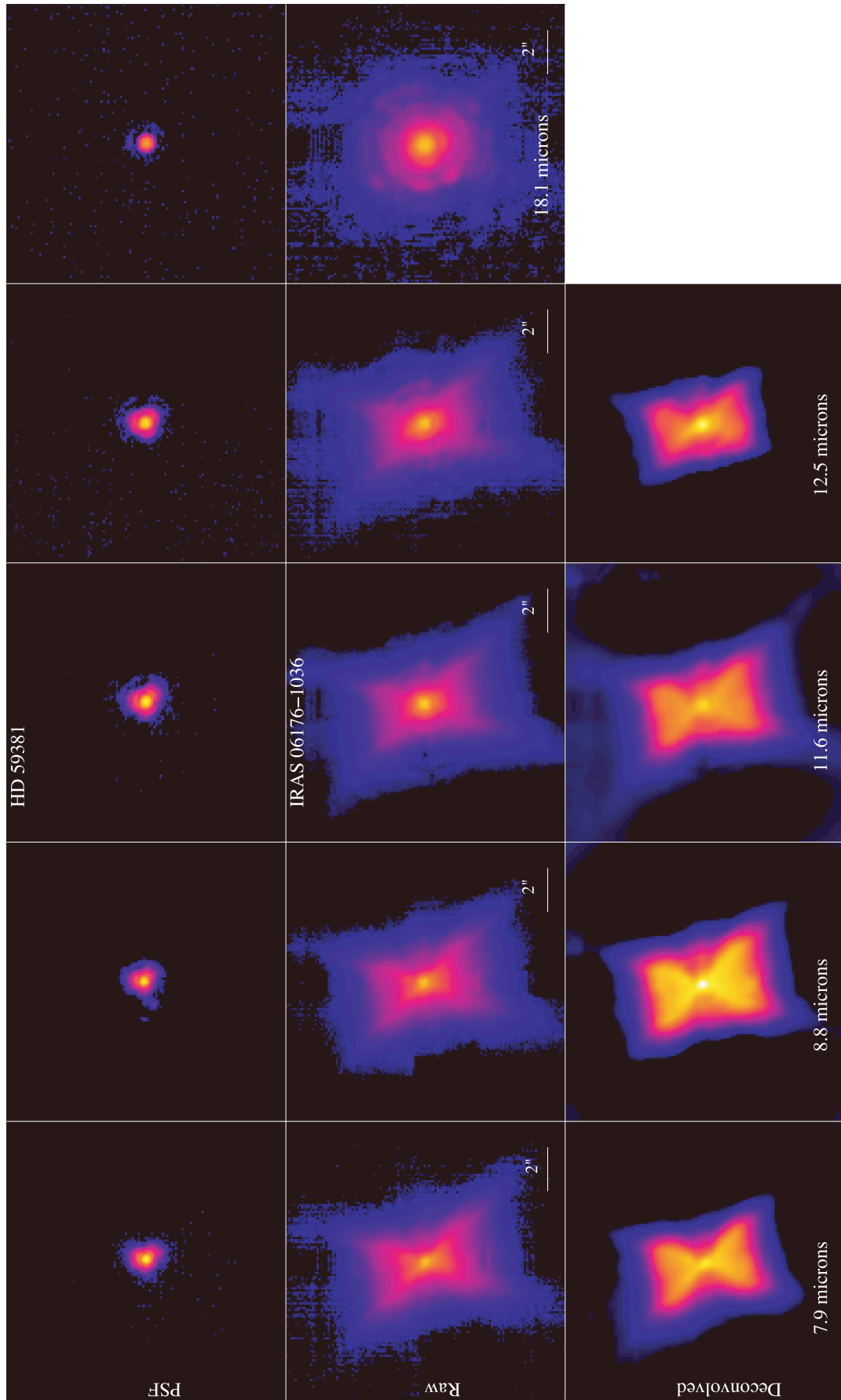


Figure B1. Michelle/Gemini-North images of IRAS 06176 (The Red Rectangle). North is up and east left.

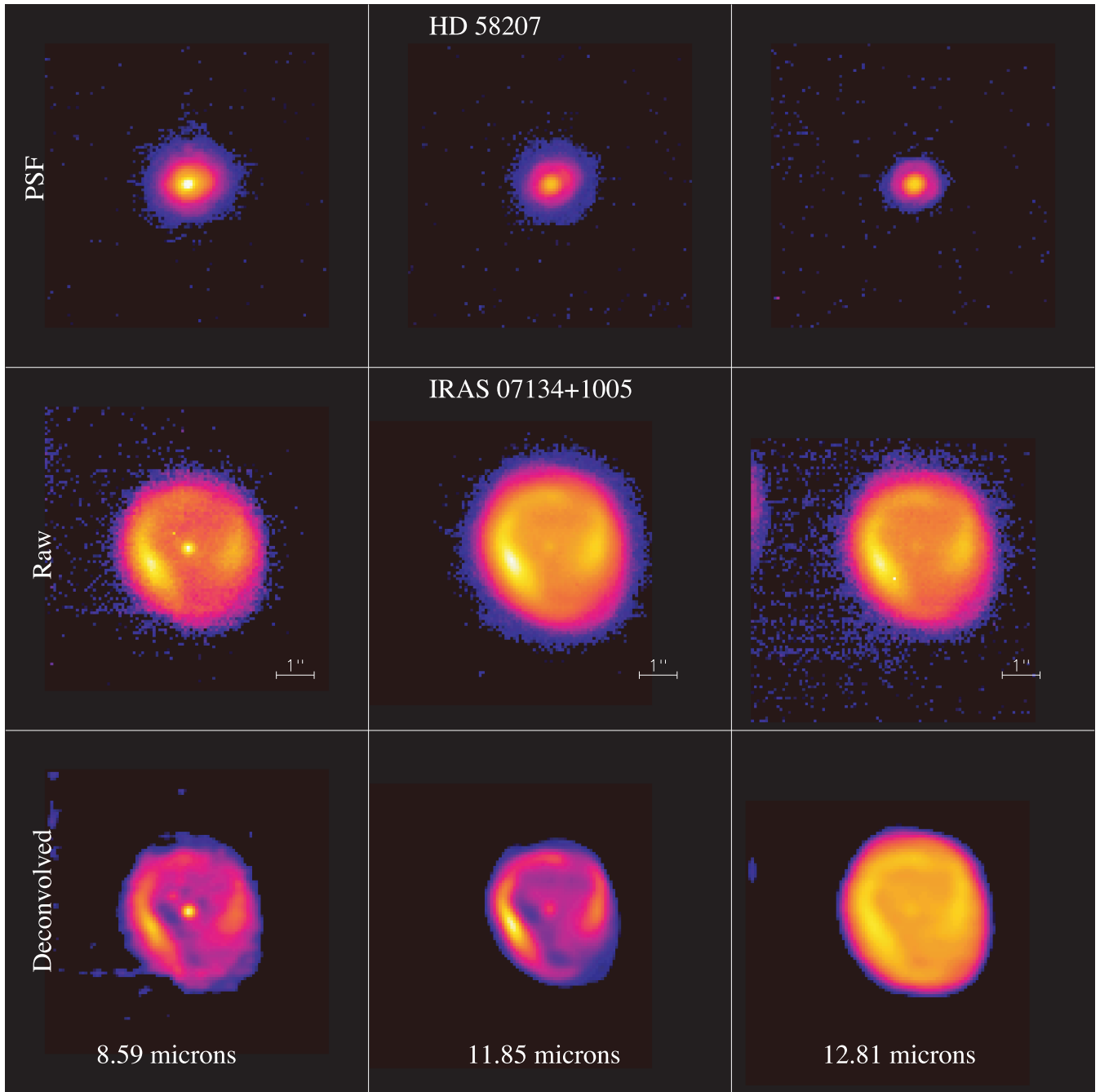


Figure B2. VISIR images of IRAS 07134 (HD 56126).

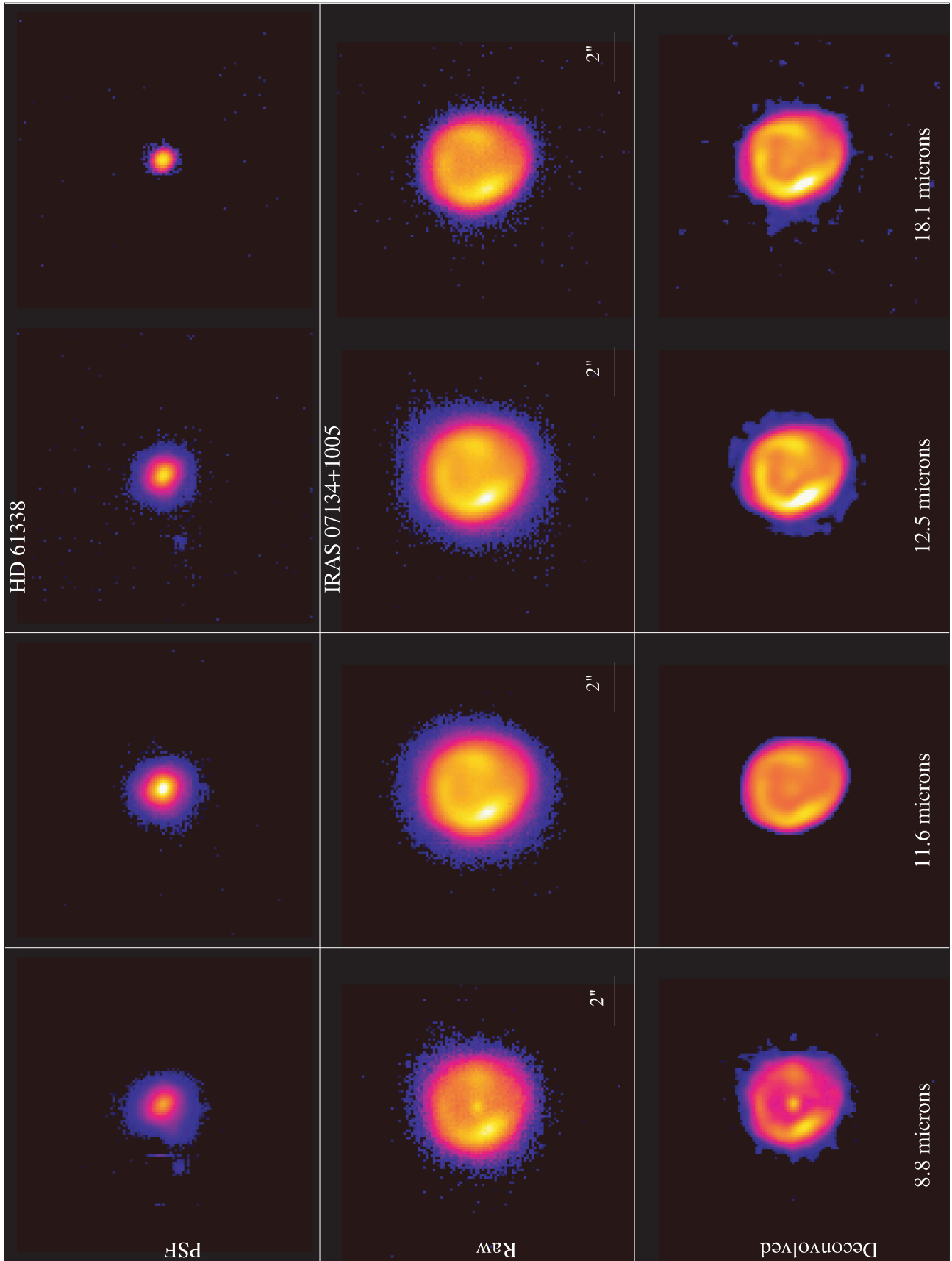


Figure B3. Michelle/Gemini-North images of IRAS 07134 (HD 56126).

Downloaded from <https://academic.oup.com/mnras/article/417/1/32/978996> by CNRS - ISTO user on 30 November 2021

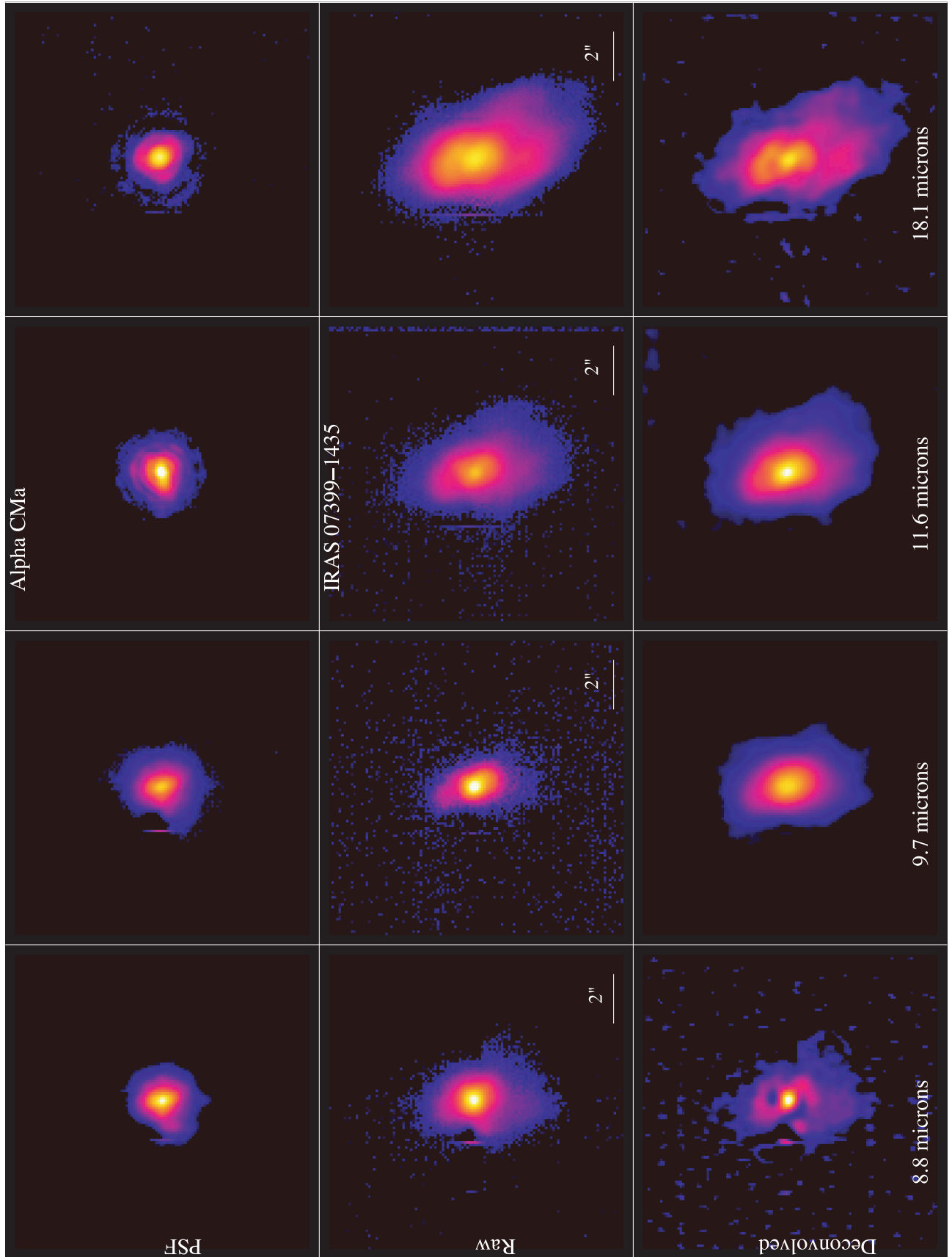


Figure B4. *Michelle/Gemini-North* images of IRAS 07399 (OH 231.8+4.2).

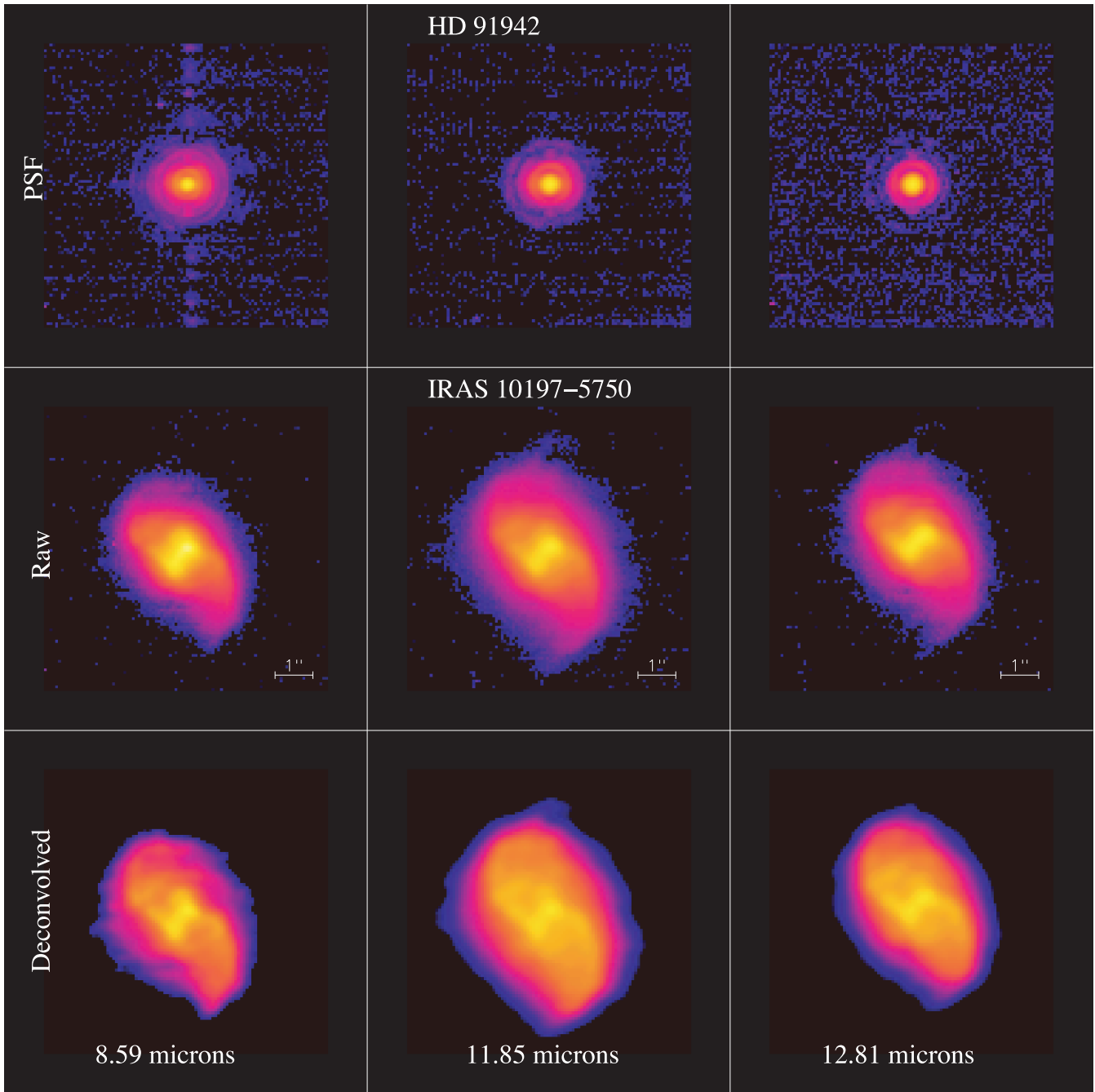


Figure B5. VISIR images of IRAS 10197 (Roberts 22).

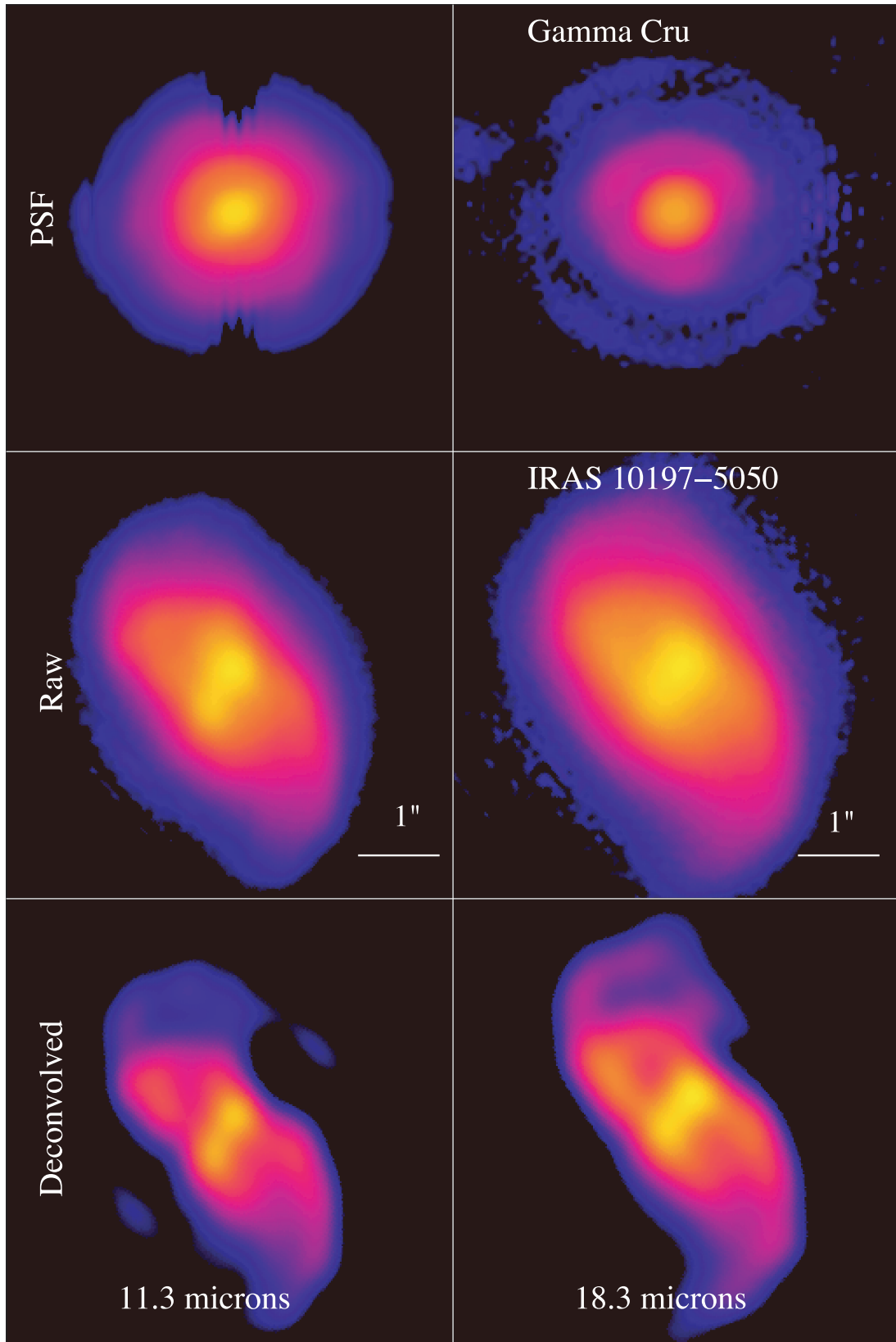


Figure B6. T-Recs images of IRAS 10197(Roberts 22).

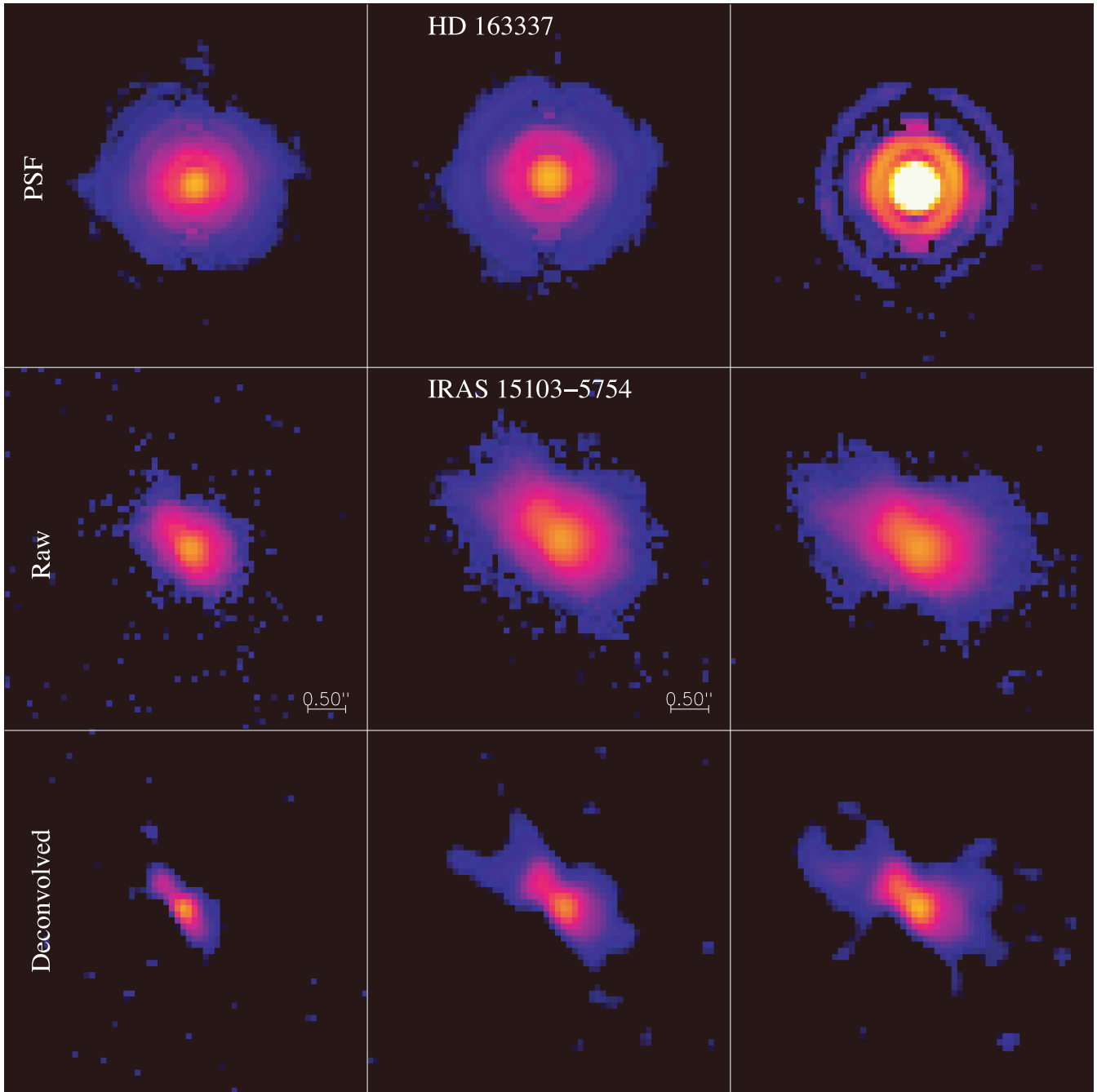


Figure B7. VISIR burst mode images of IRAS 15103.

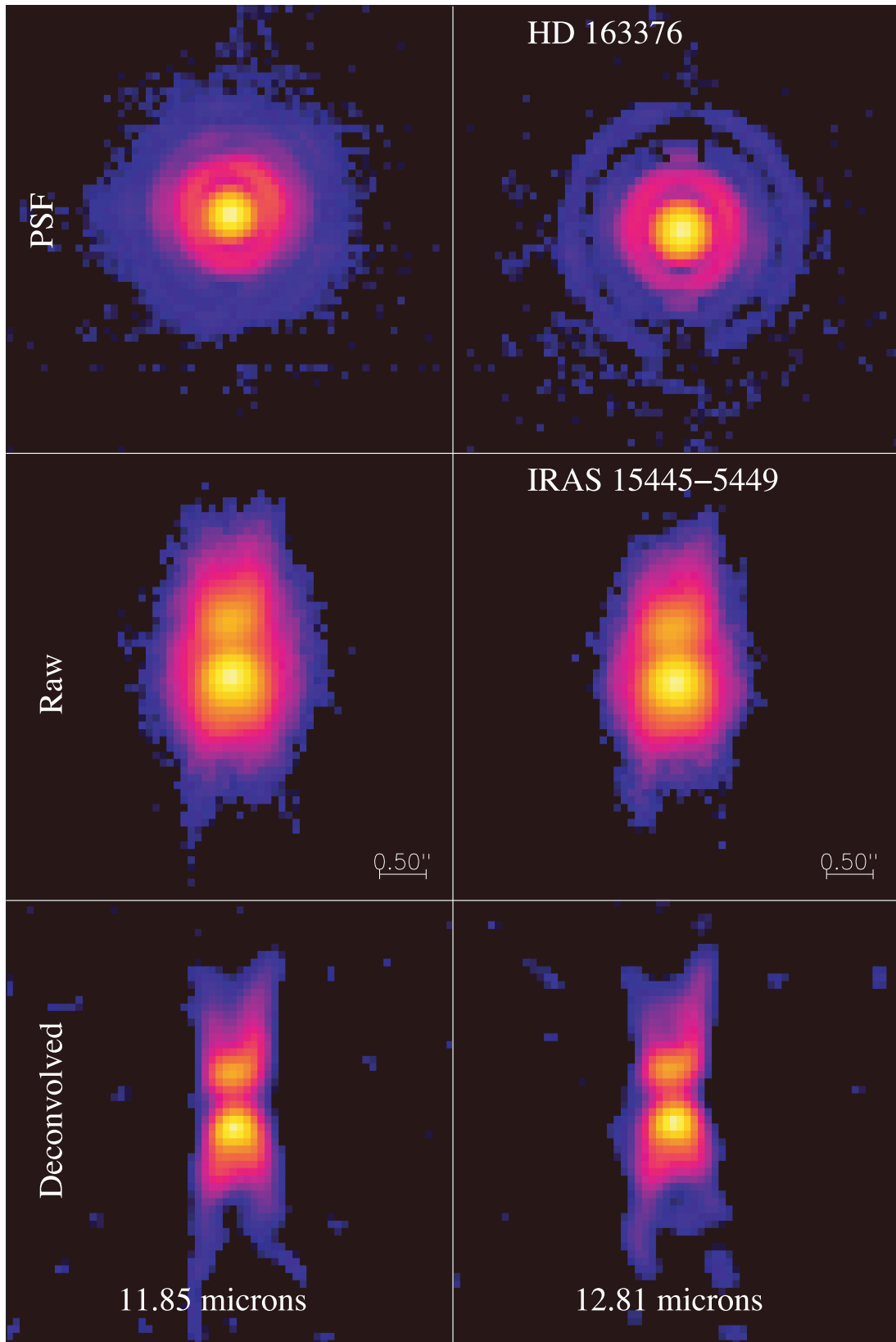


Figure B8. VISIR burst mode images of IRAS 15445.

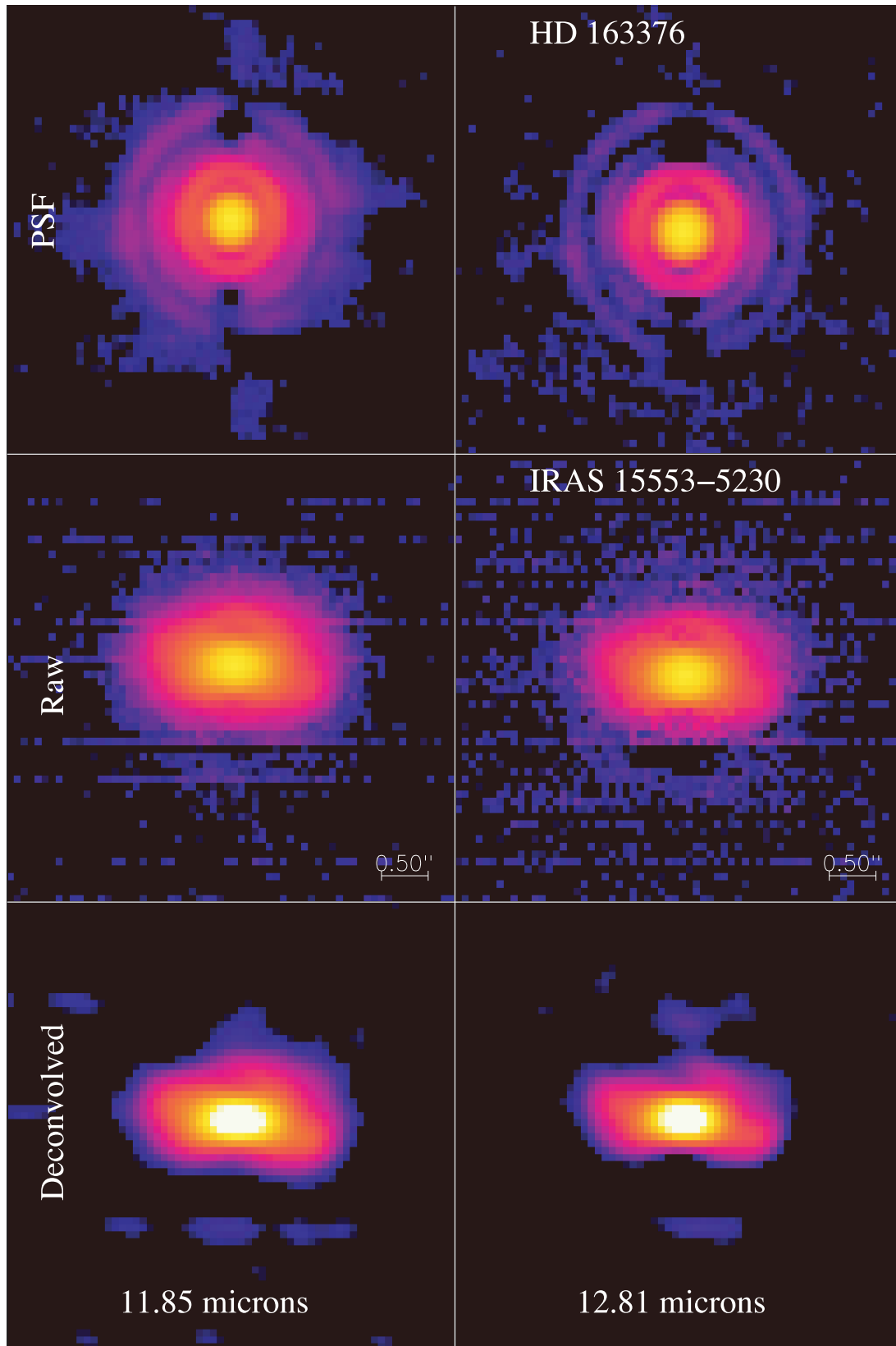


Figure B9. VISIR burst mode images of IRAS 15553.

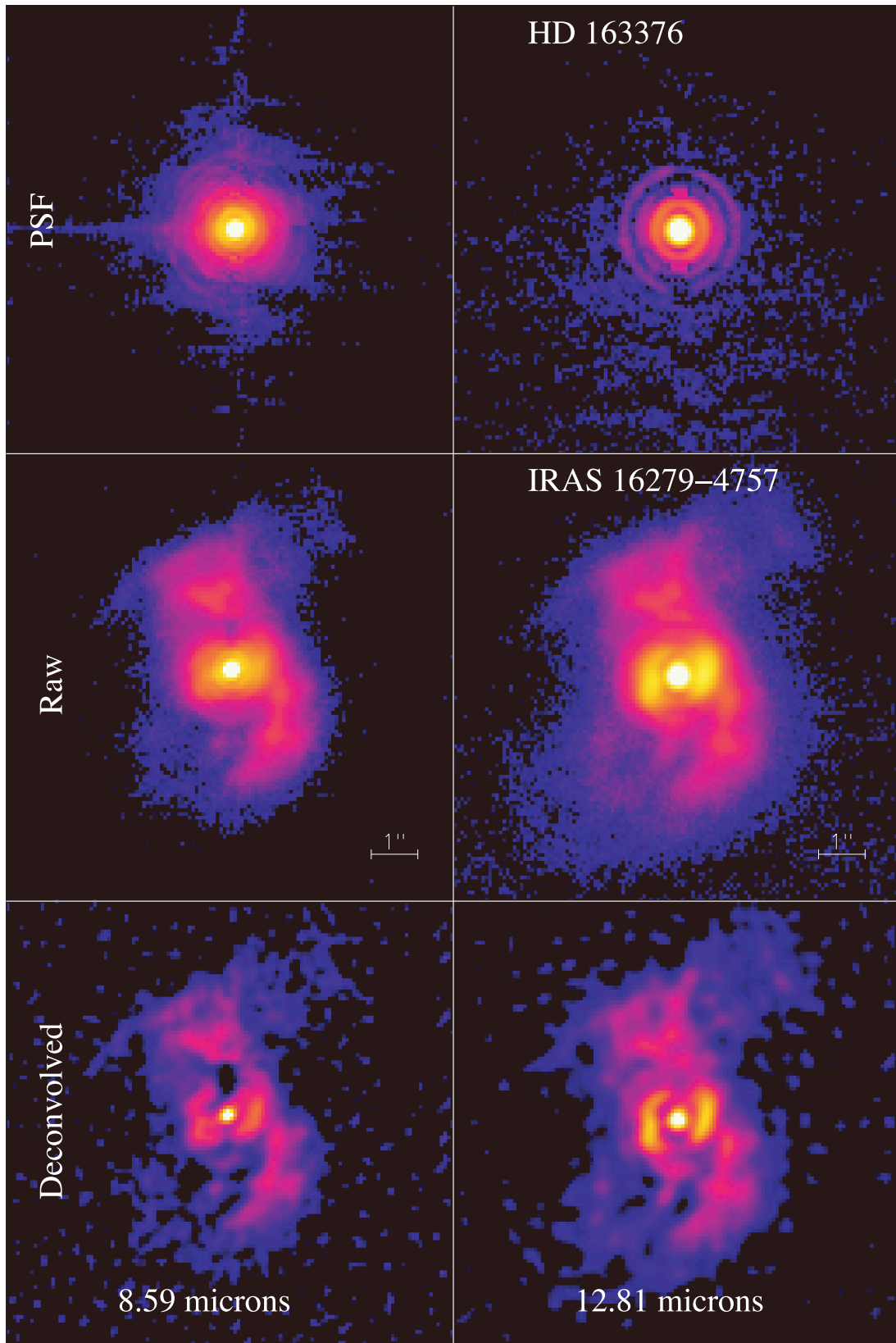


Figure B10. VISIR burst mode images of IRAS 16279.

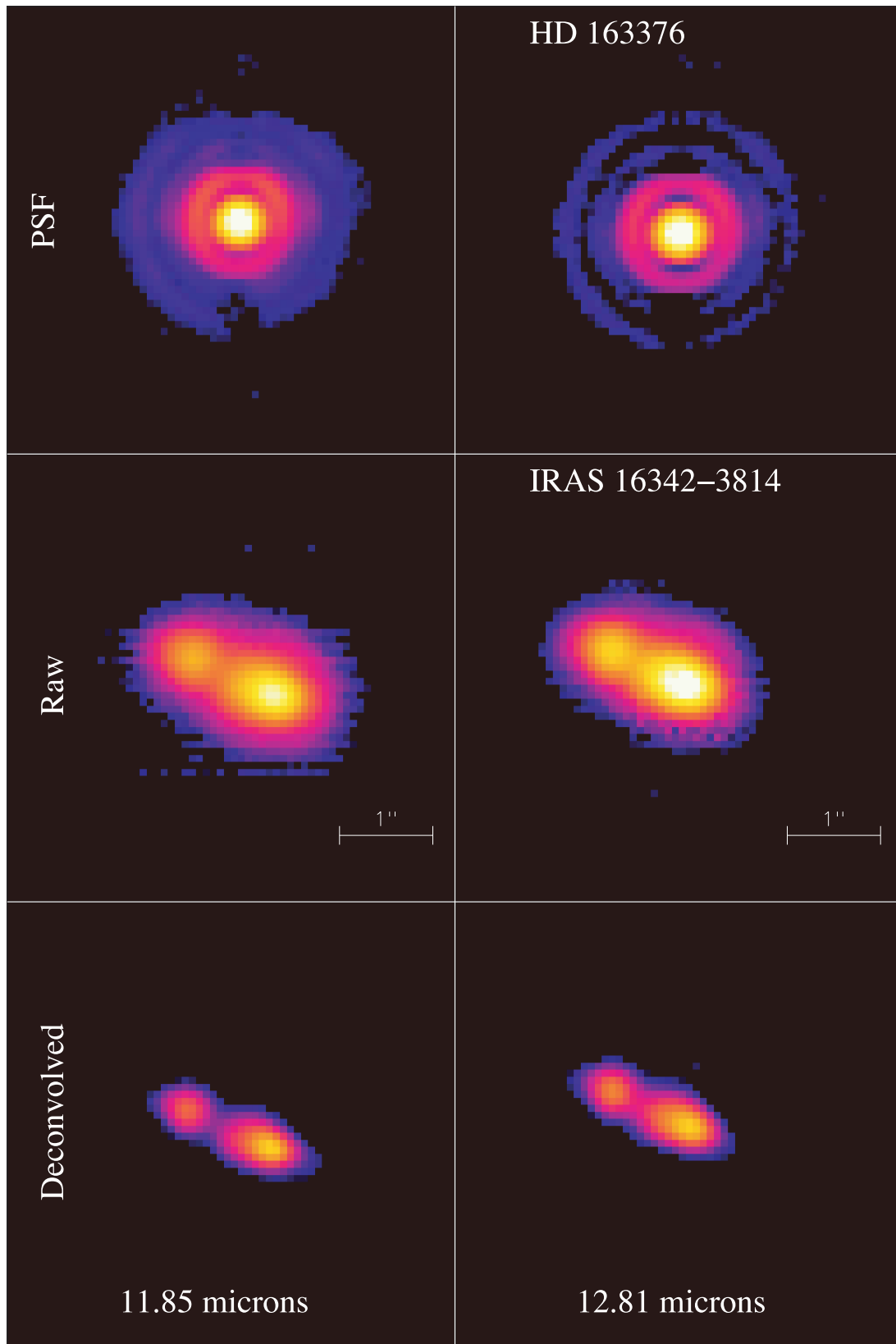


Figure B11. VISIR burst mode images of IRAS 16342 (The water fountain).

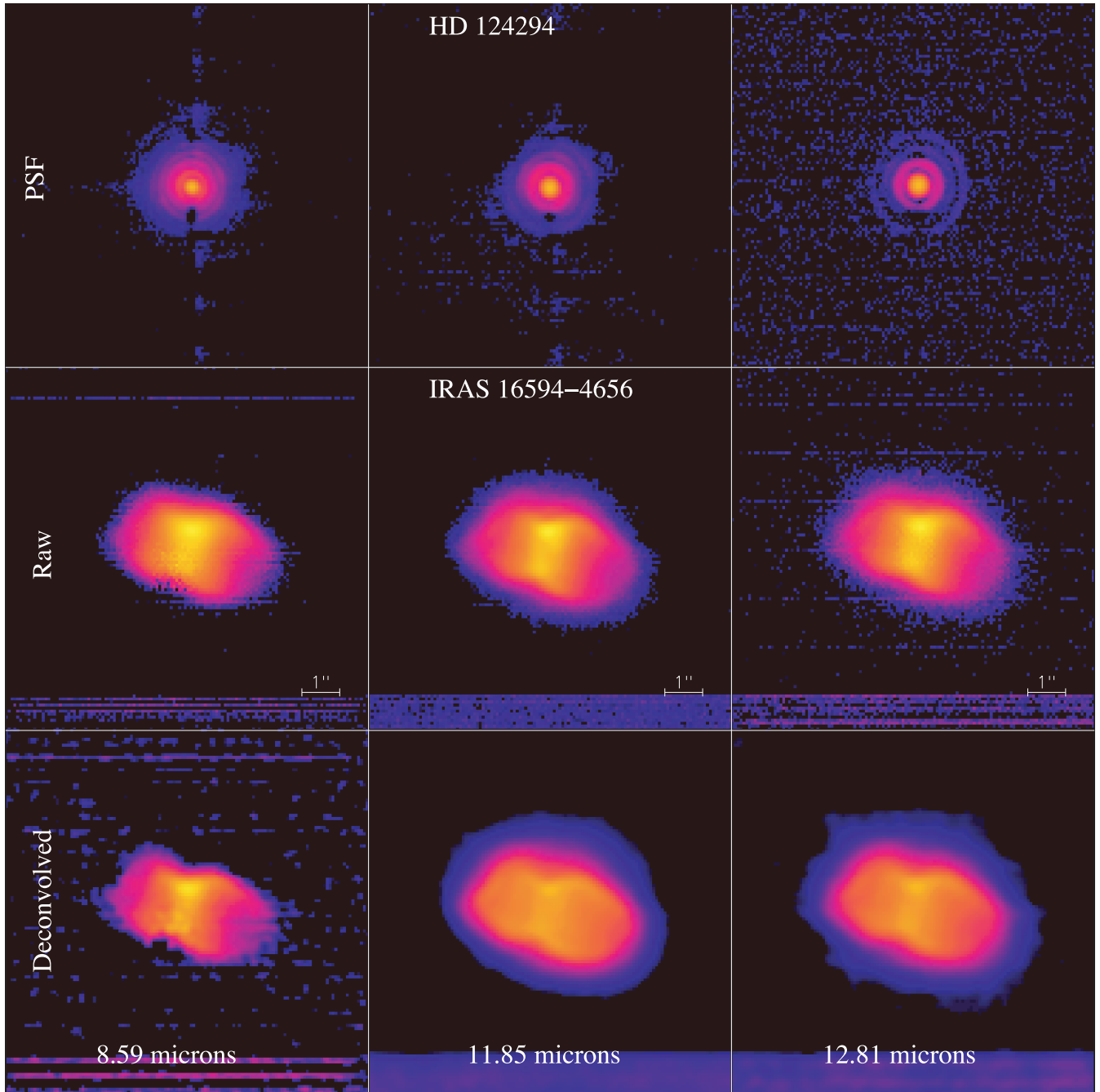


Figure B12. VISIR burst mode images of IRAS 16594 (the Water-Lily nebula).

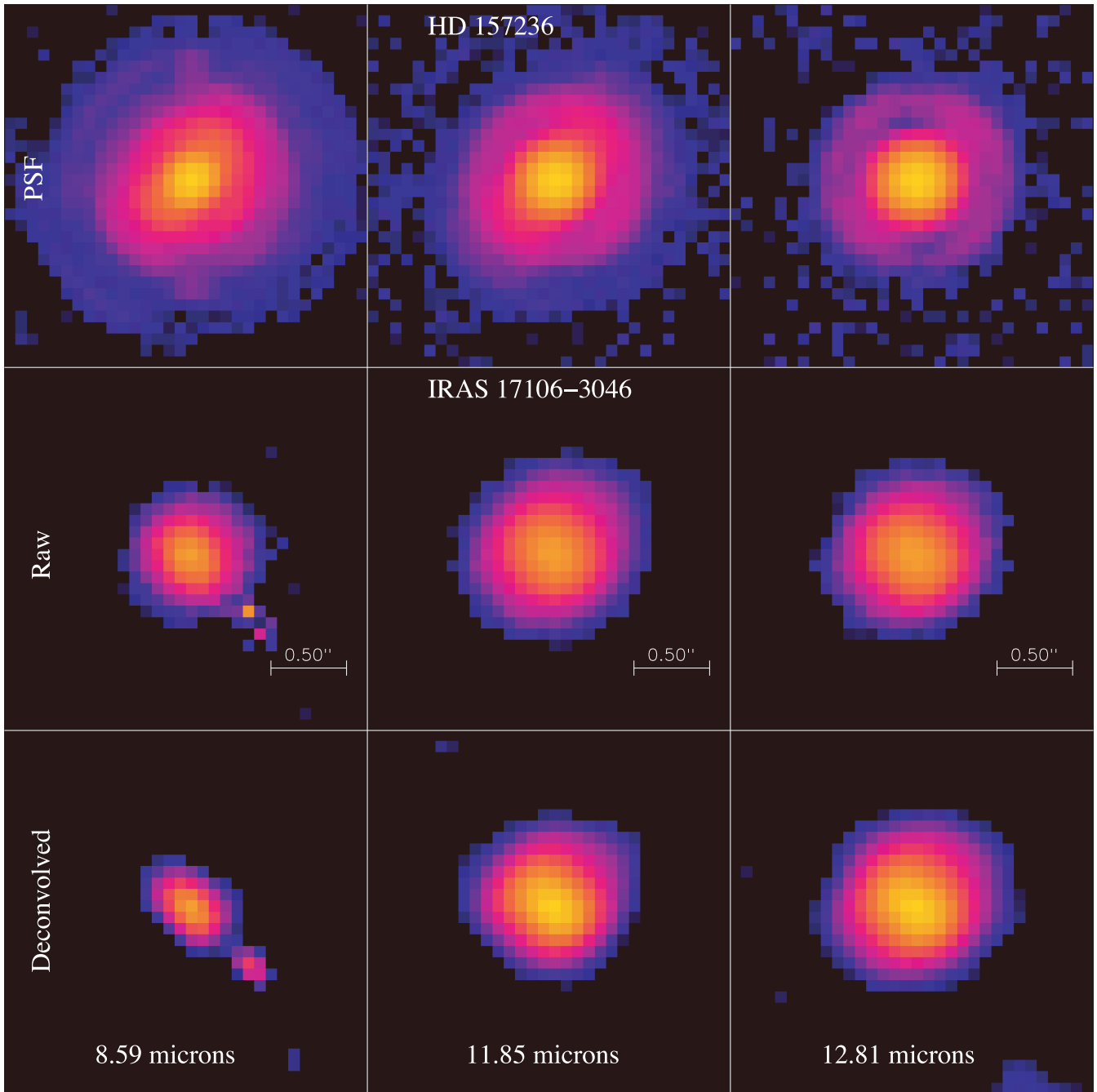


Figure B13. VISIR burst mode images of IRAS 17106.

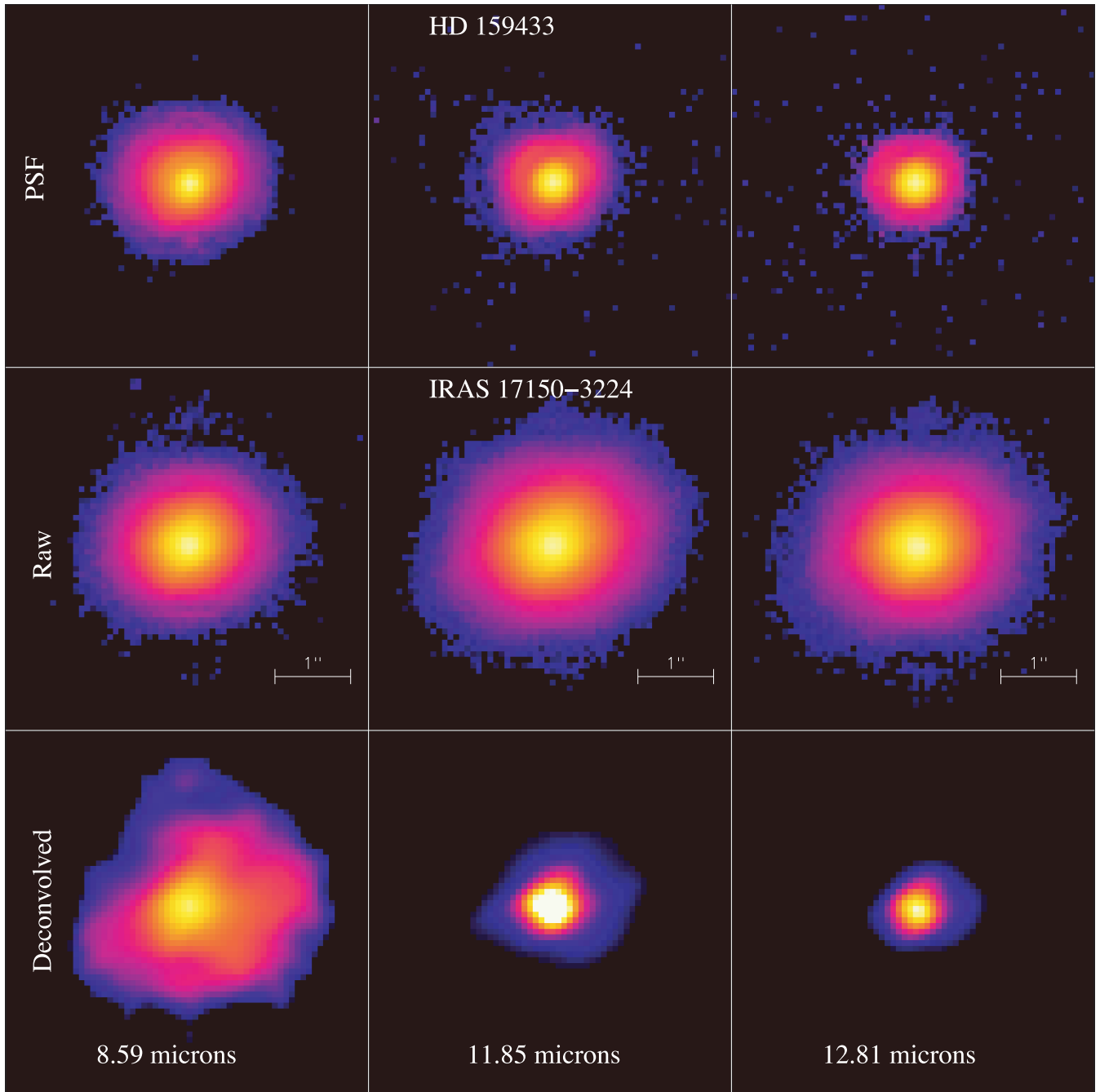


Figure B14. VISIR burst mode images of IRAS 17150.

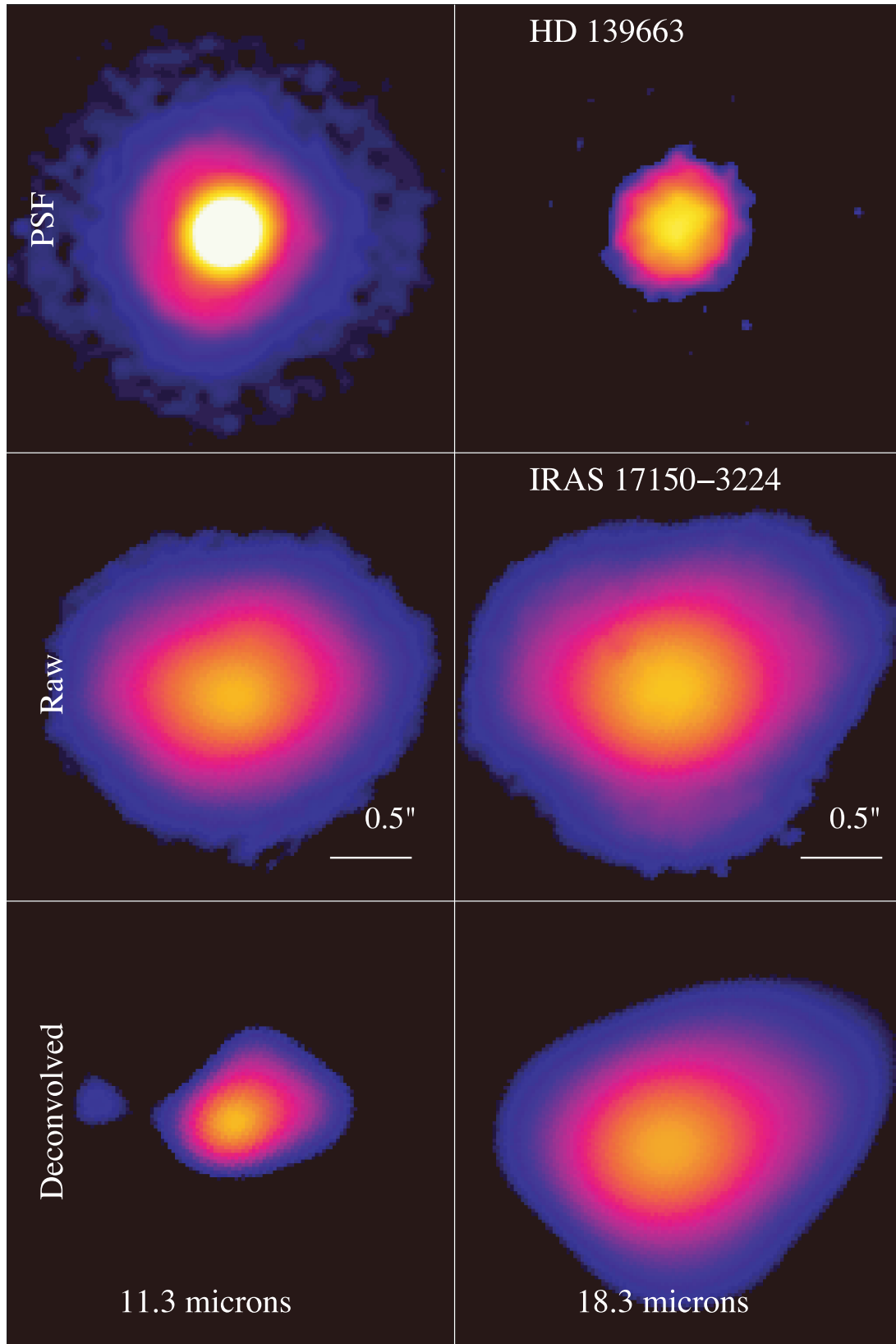


Figure B15. T-Recs/*Gemini* images of IRAS 17150 (The Cotton Candy nebula).

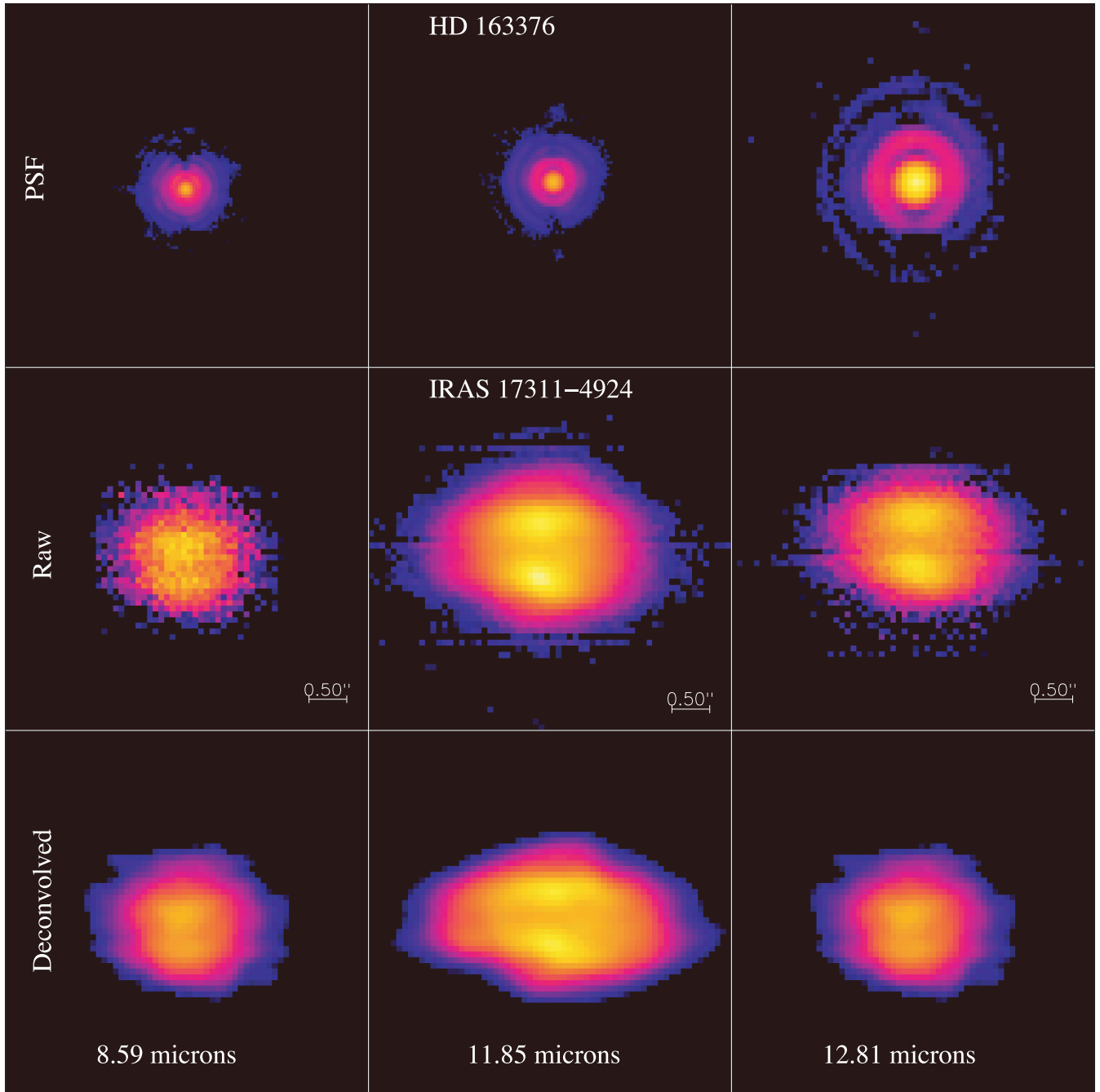


Figure B16. VISIR burst mode images of IRAS 17311.

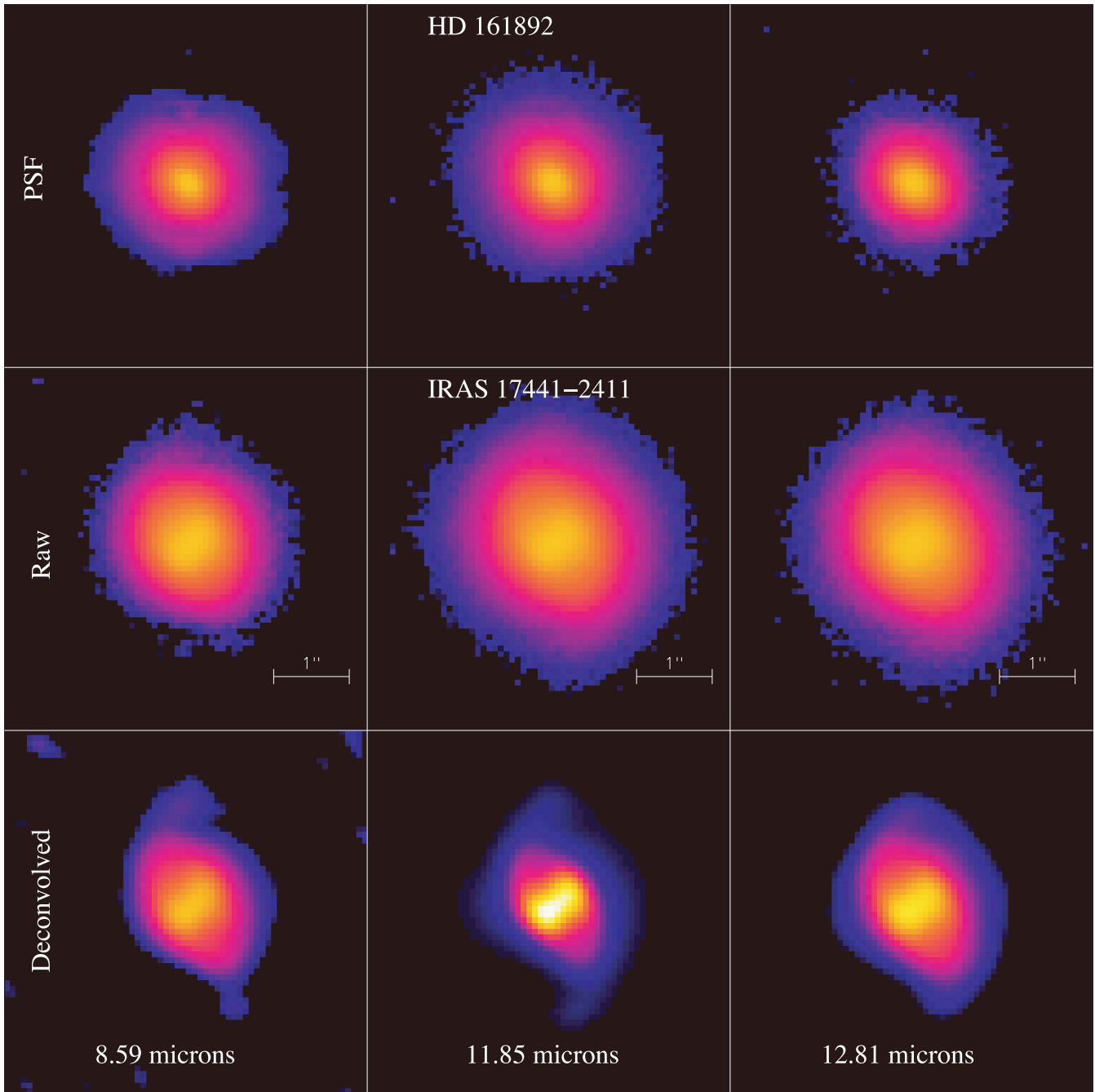


Figure B17. VISIR burst mode images of IRAS 17441.

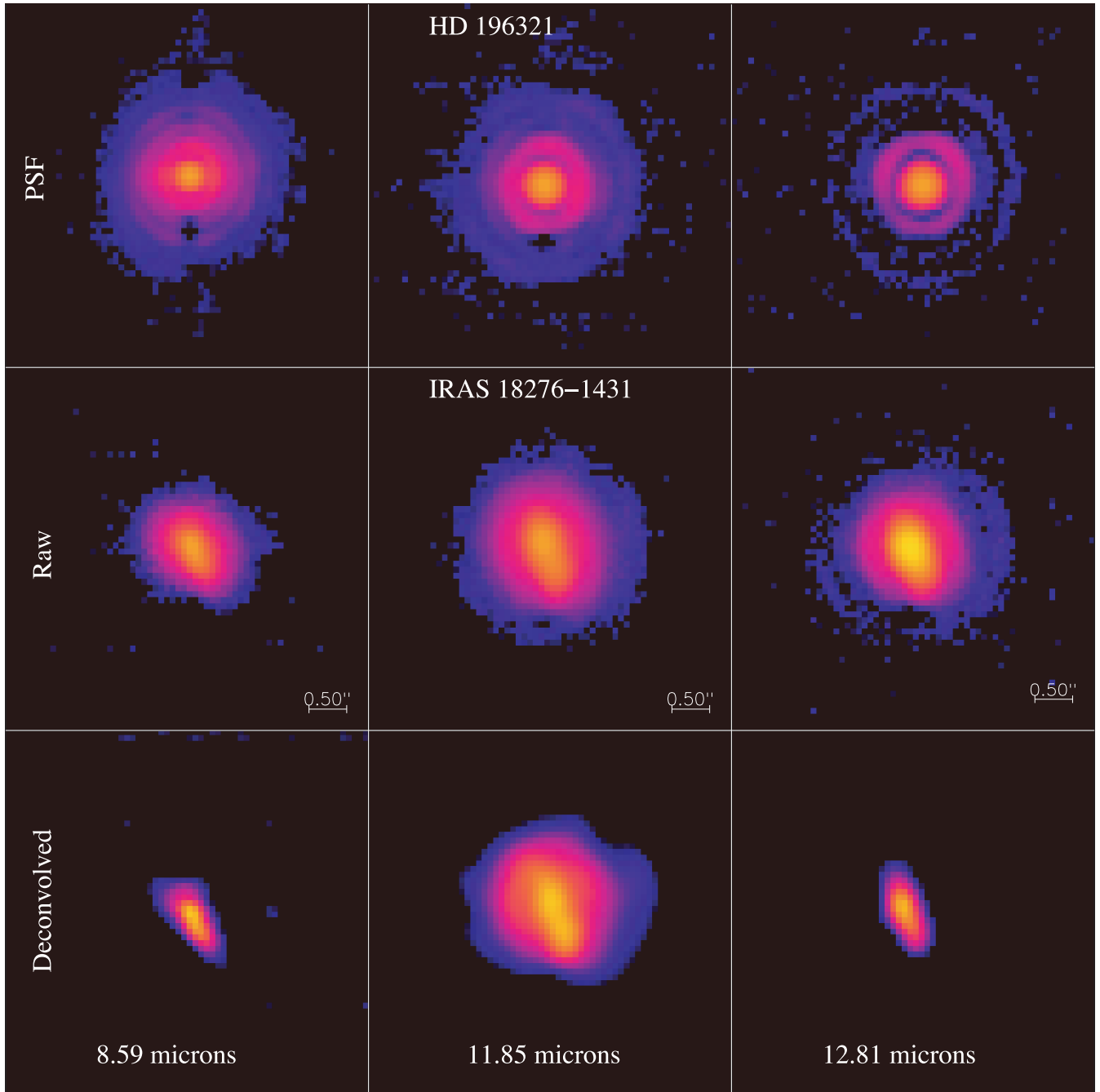


Figure B18. VISIR burst mode images of IRAS 18276.

Downloaded from <https://academic.oup.com/mnras/article/417/1/32/978996> by CNRS - ISTO user on 30 November 2021

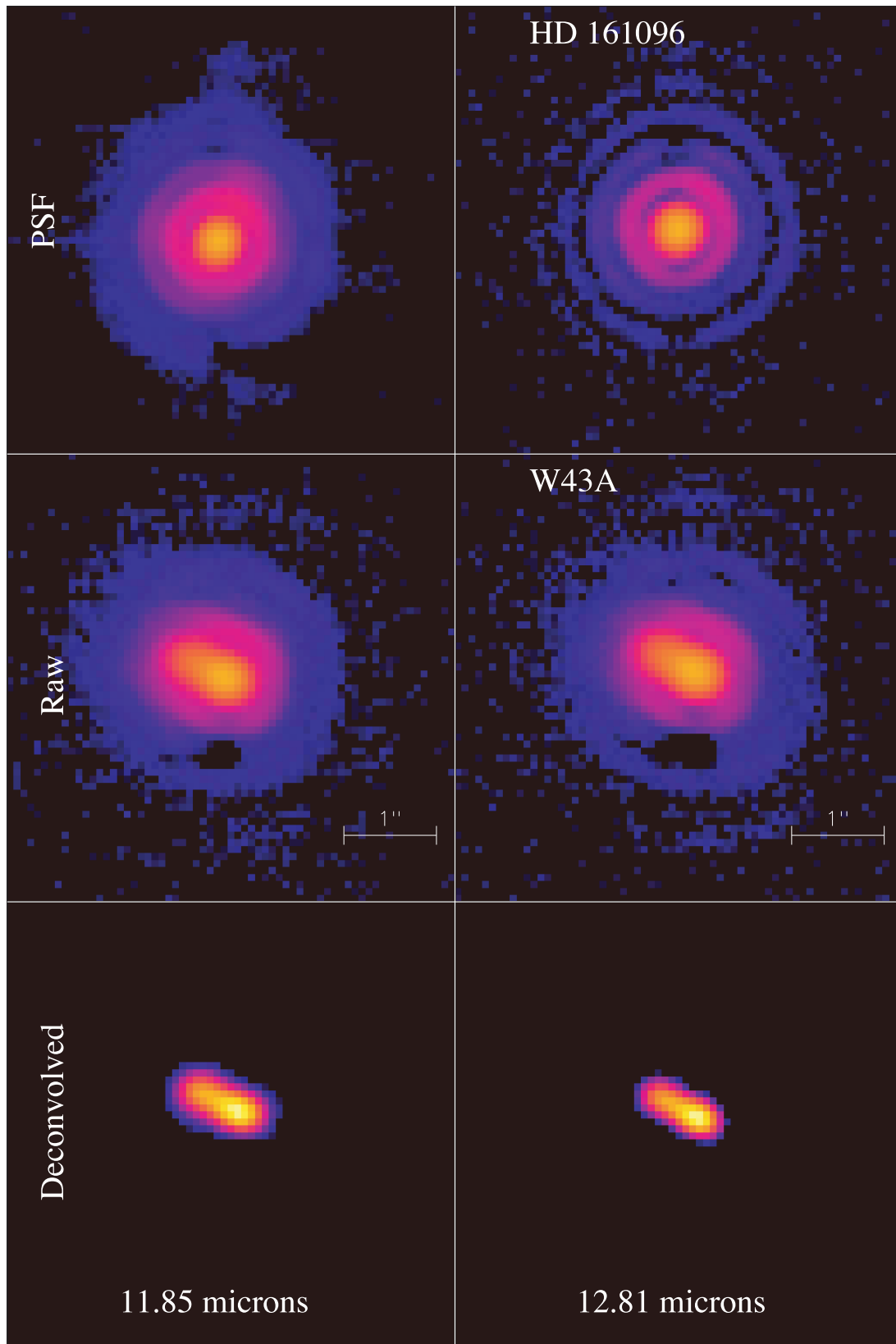


Figure B19. VISIR burst mode images of W43A.

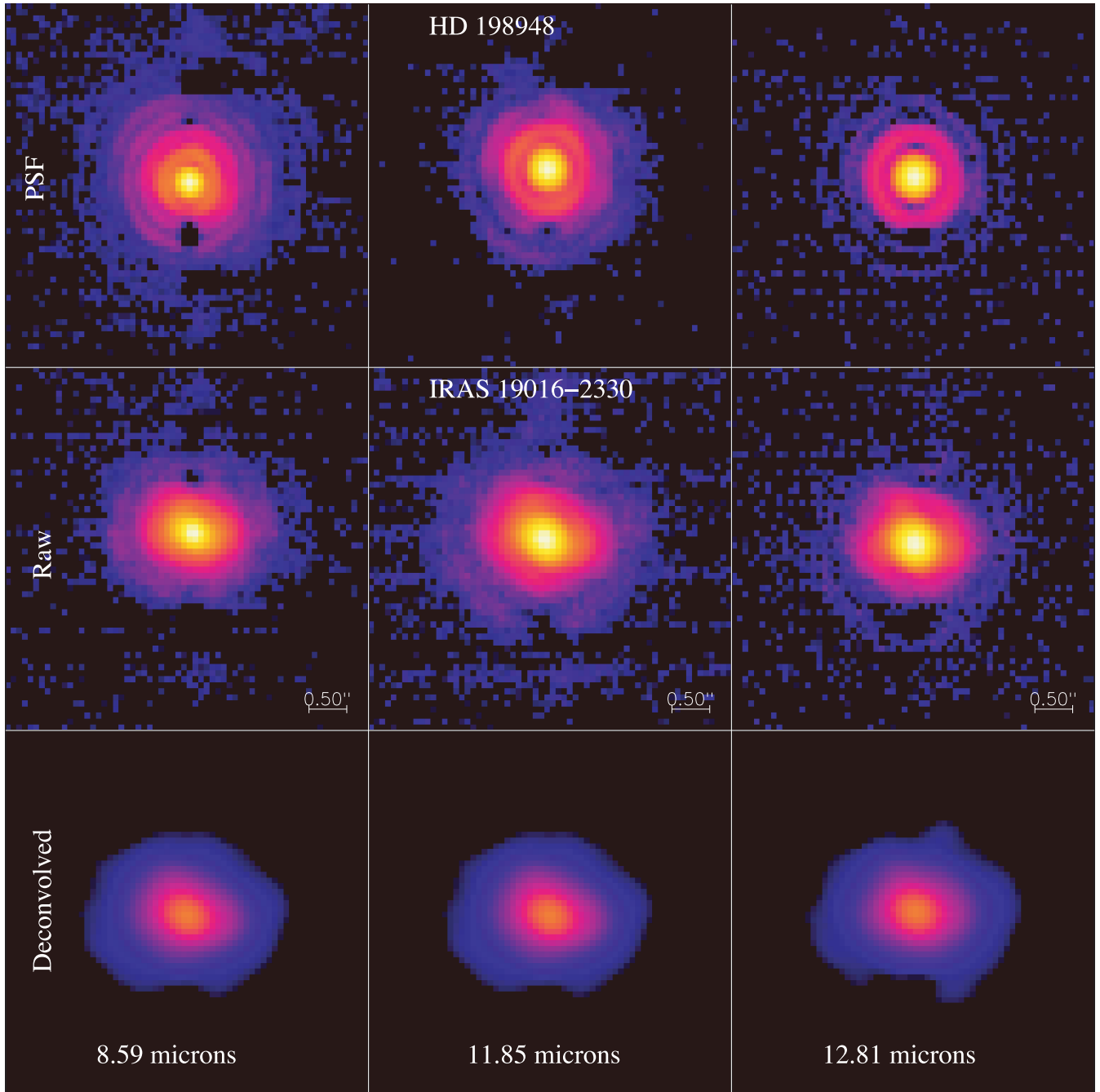


Figure B20. VISIR burst mode images of IRAS 19016.

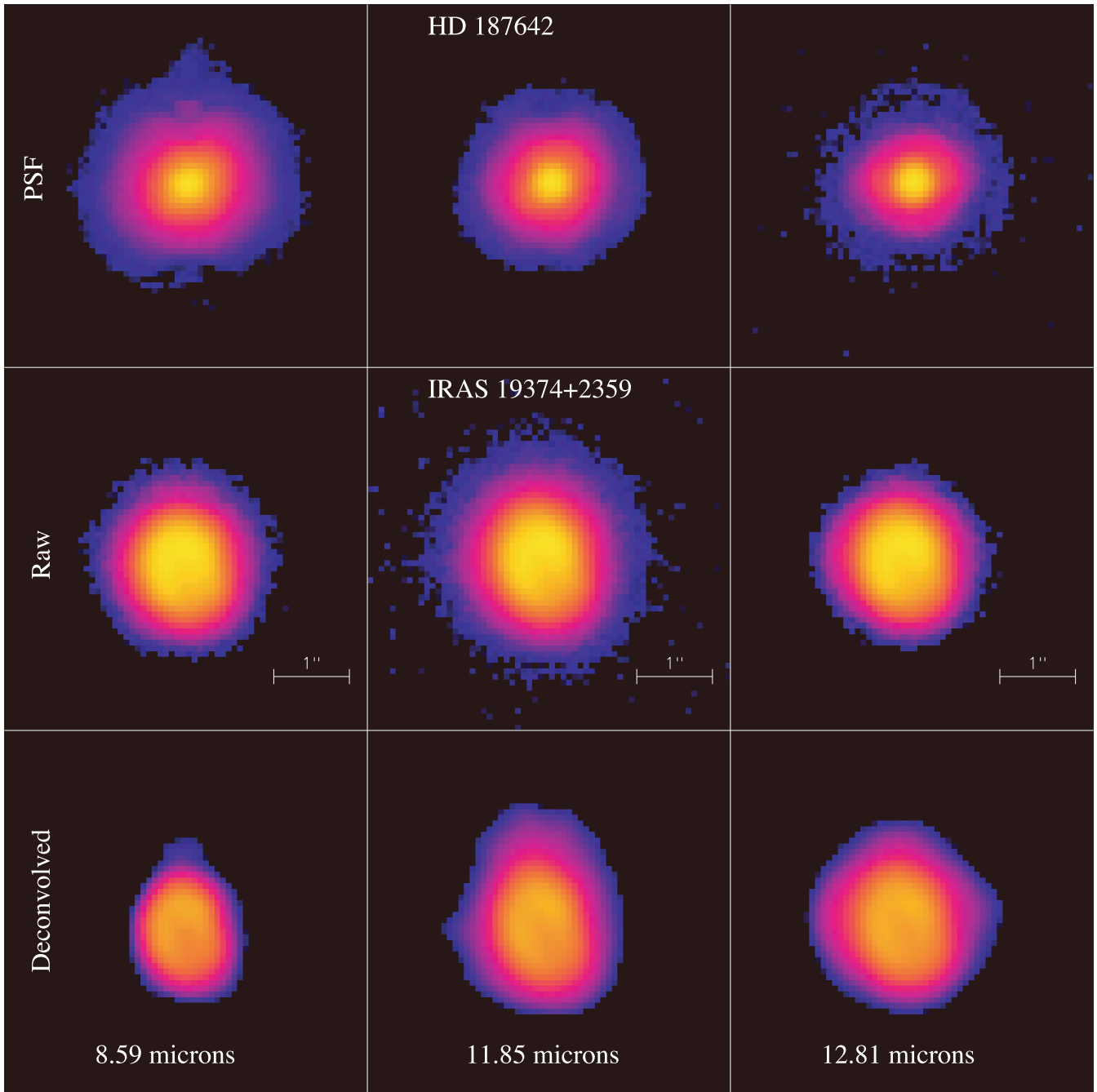


Figure B21. VISIR images of IRAS 19347.

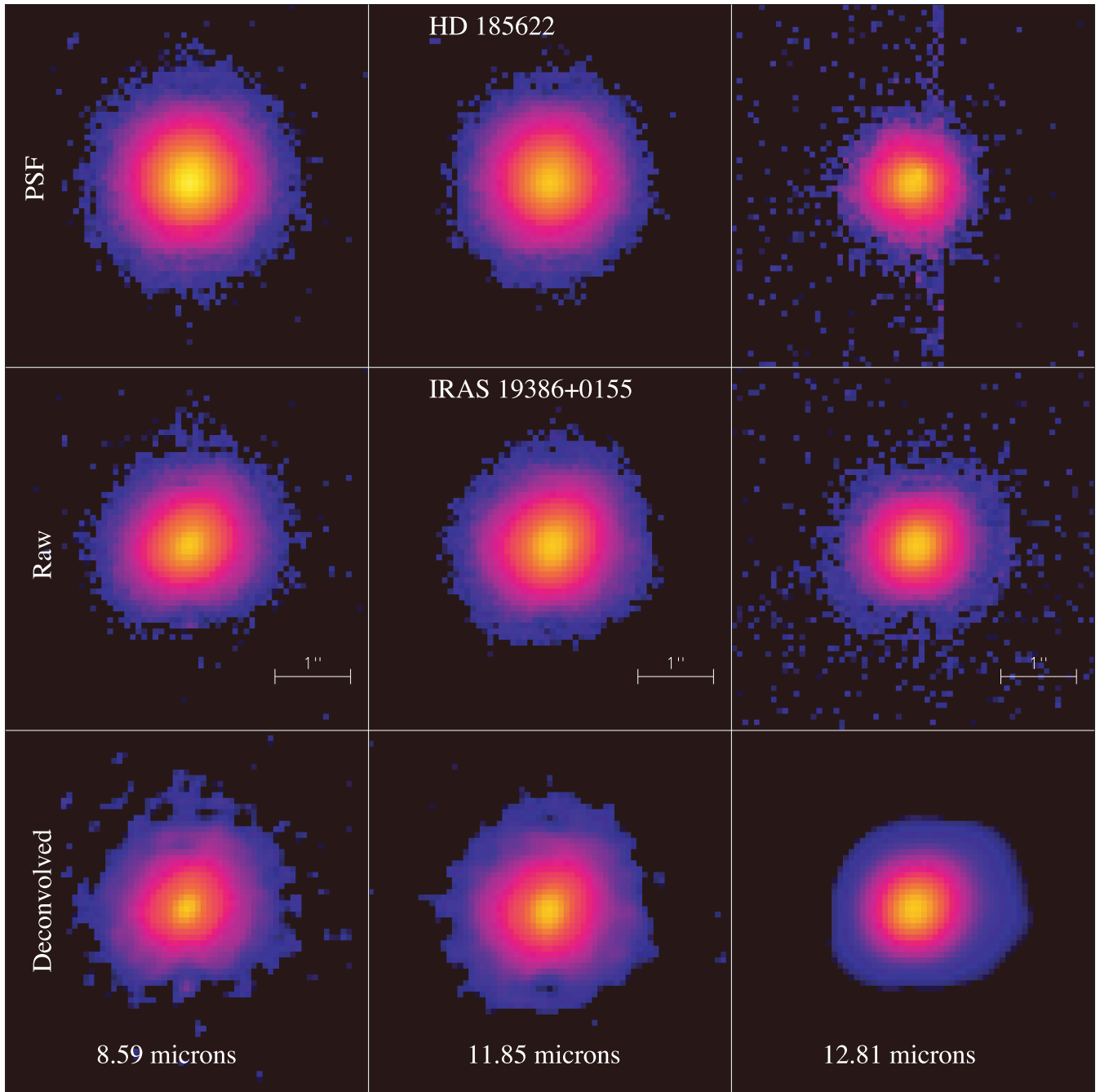


Figure B22. VISIR burst mode images of IRAS 19386.

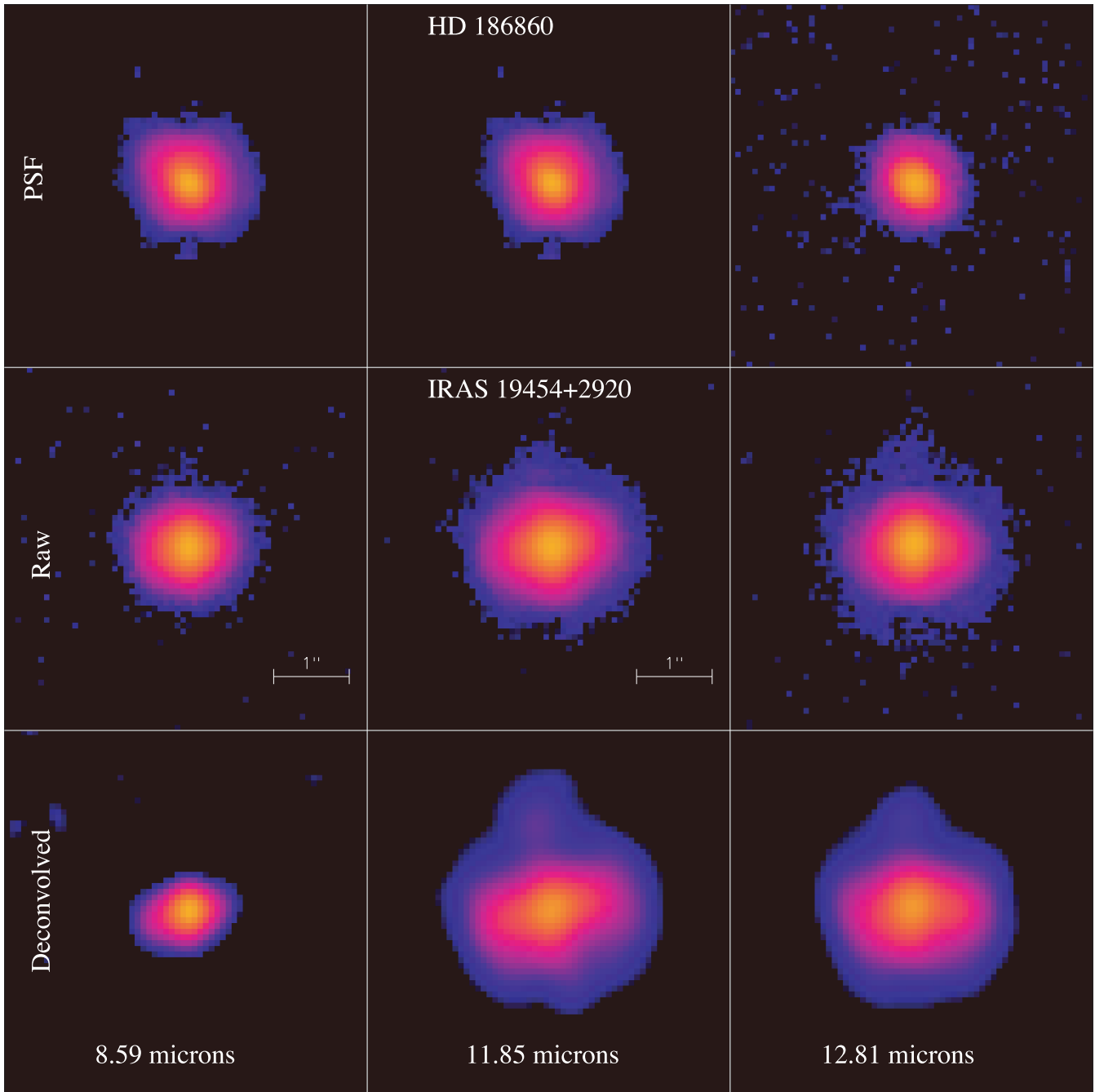


Figure B23. VISIR burst mode images of IRAS 10197.

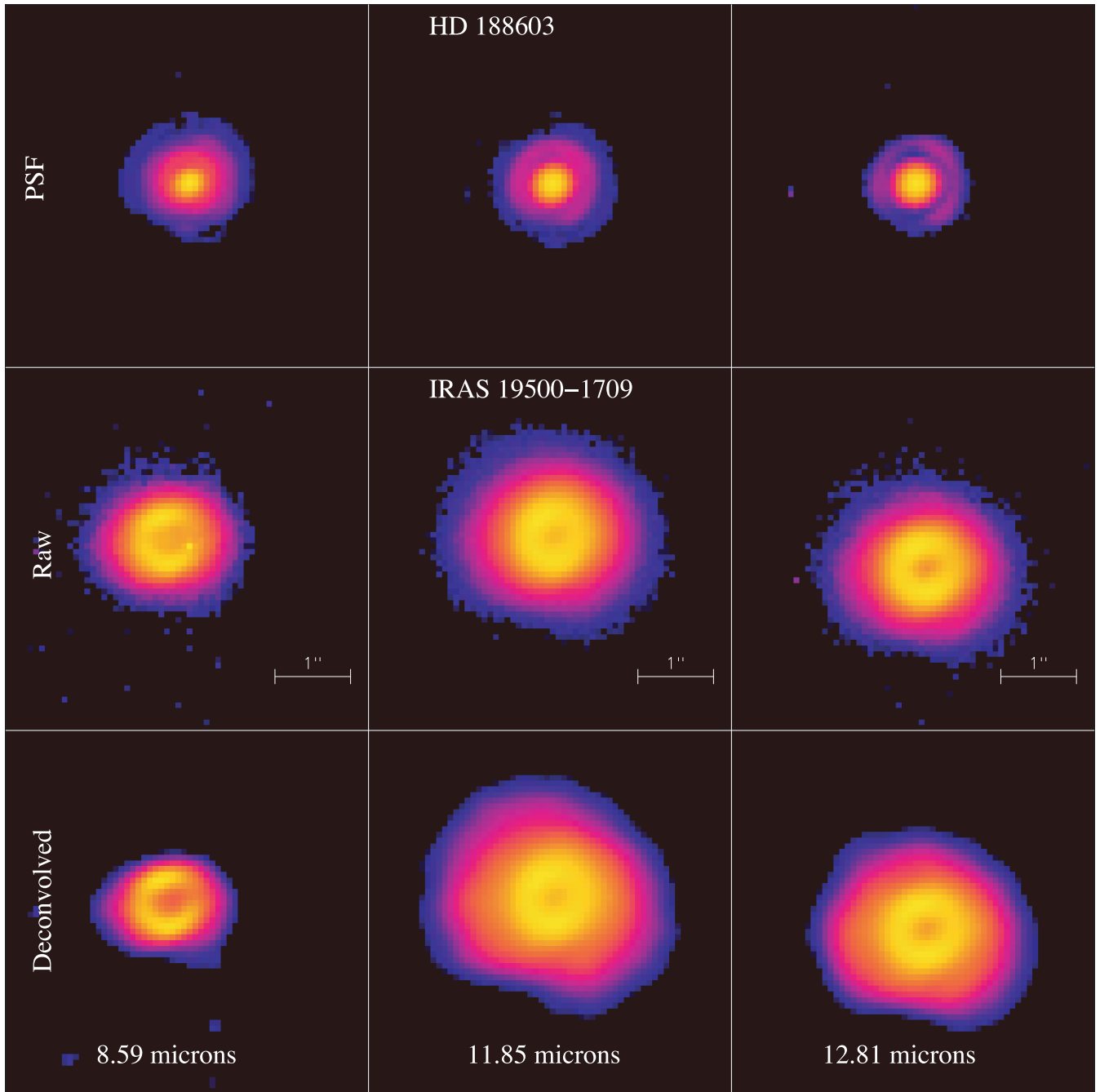


Figure B24. VISIR images of IRAS 19500.

Downloaded from <https://academic.oup.com/mnras/article/417/1/32/978996> by CNRS - ISTO user on 30 November 2021

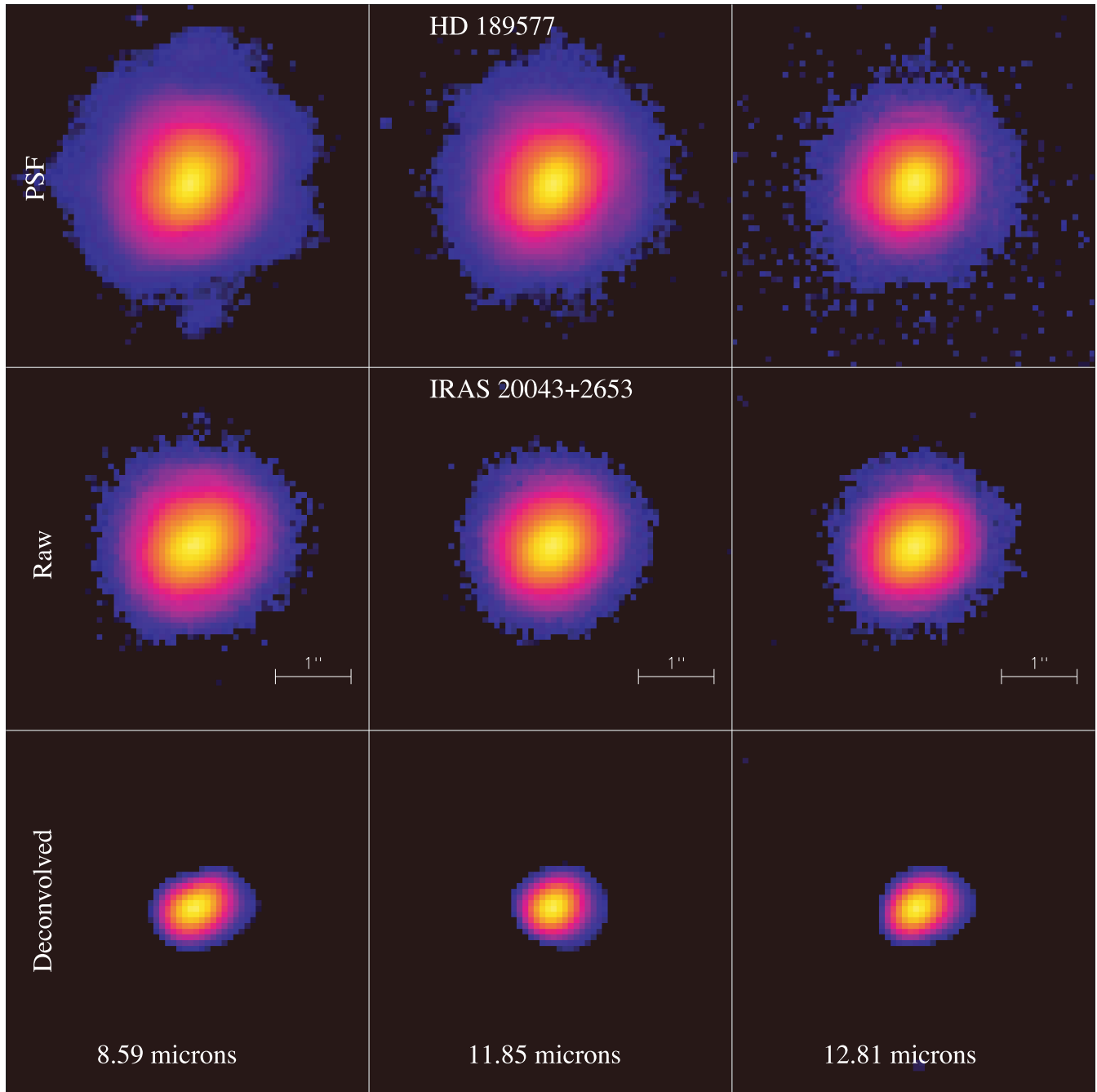


Figure B25. VISIR burst mode images of IRAS 20043.

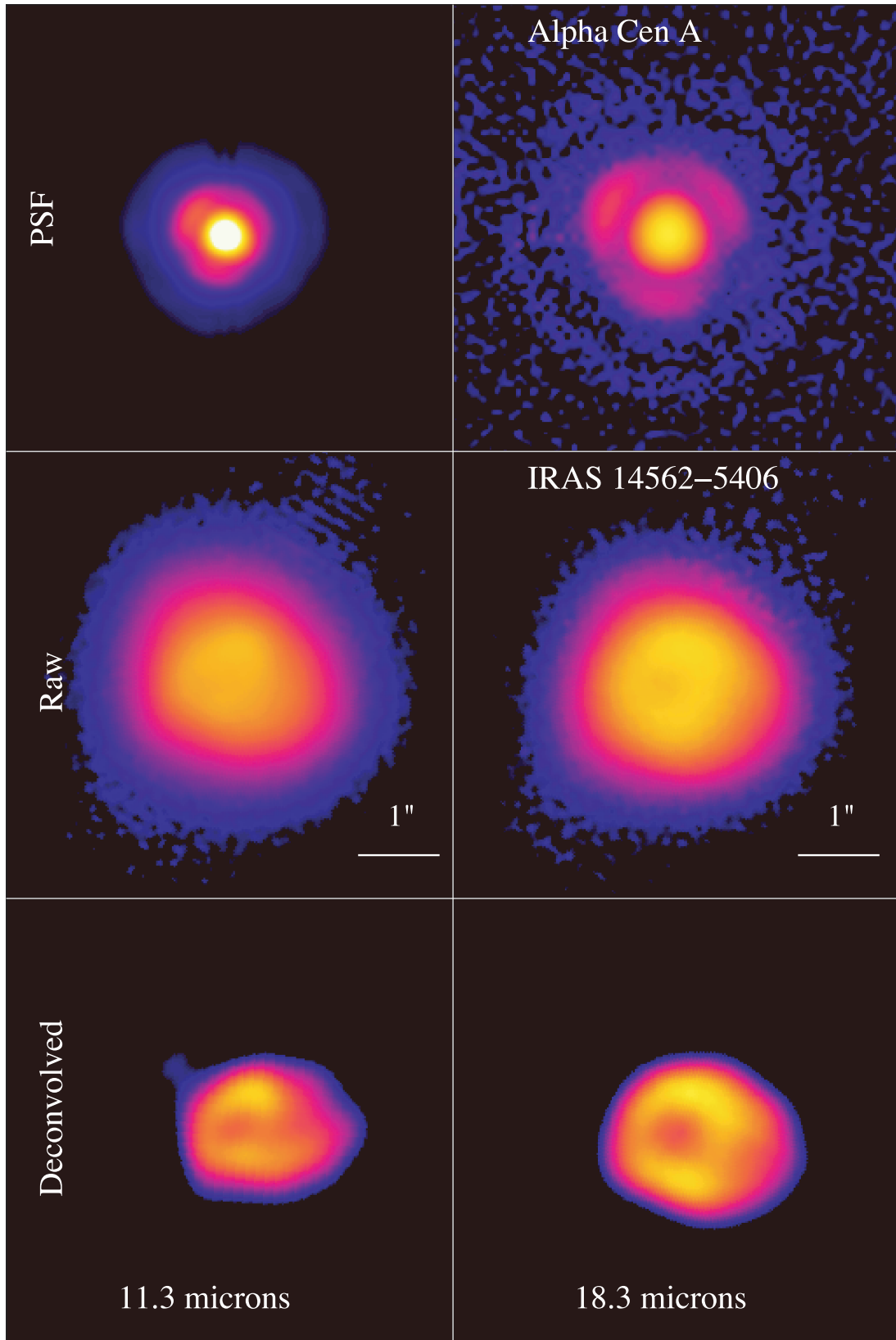


Figure B26. T-Recs images of IRAS 14562 (Hen 2-113).

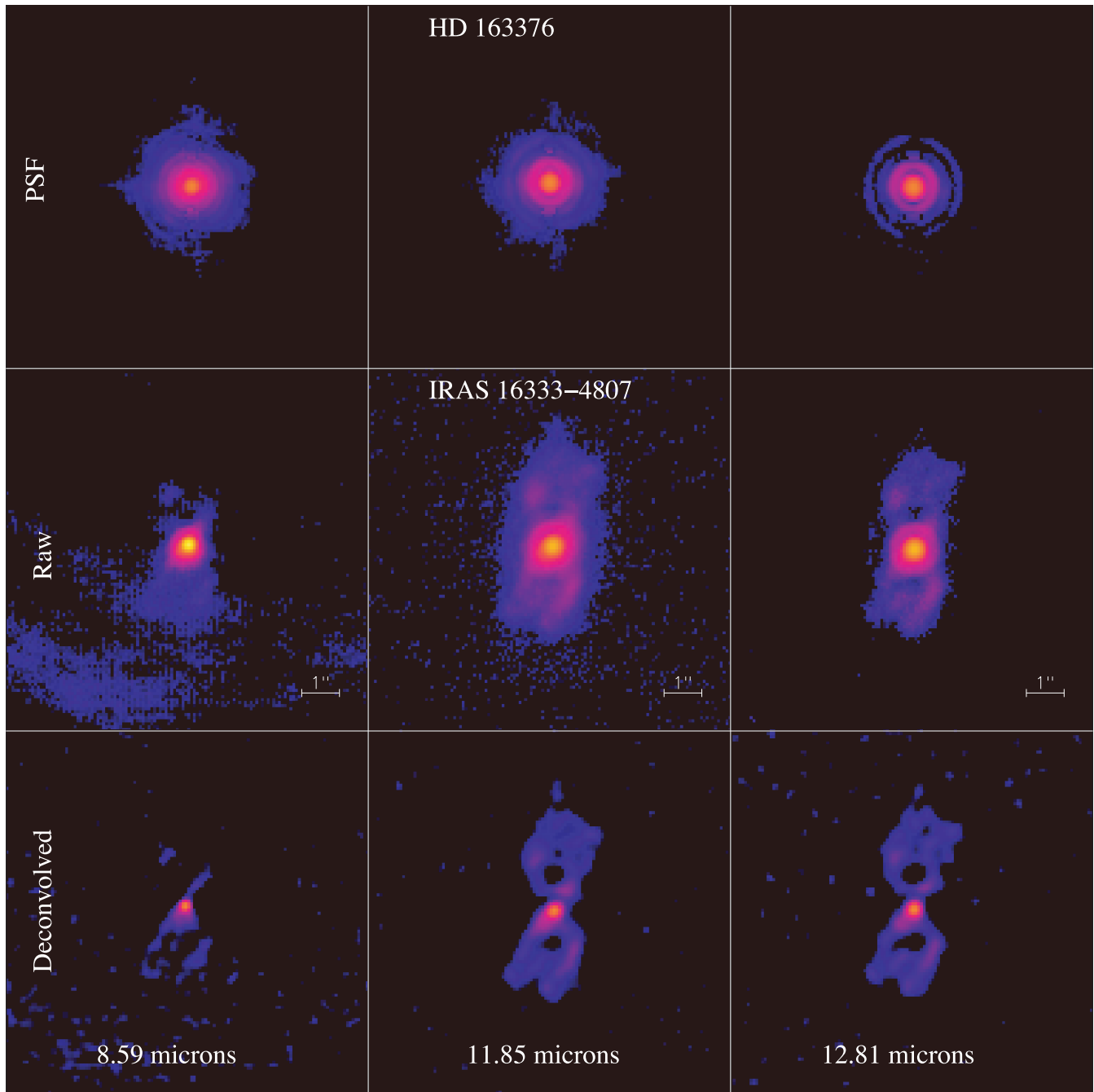


Figure B27. VISIR burst mode images of IRAS 16333.

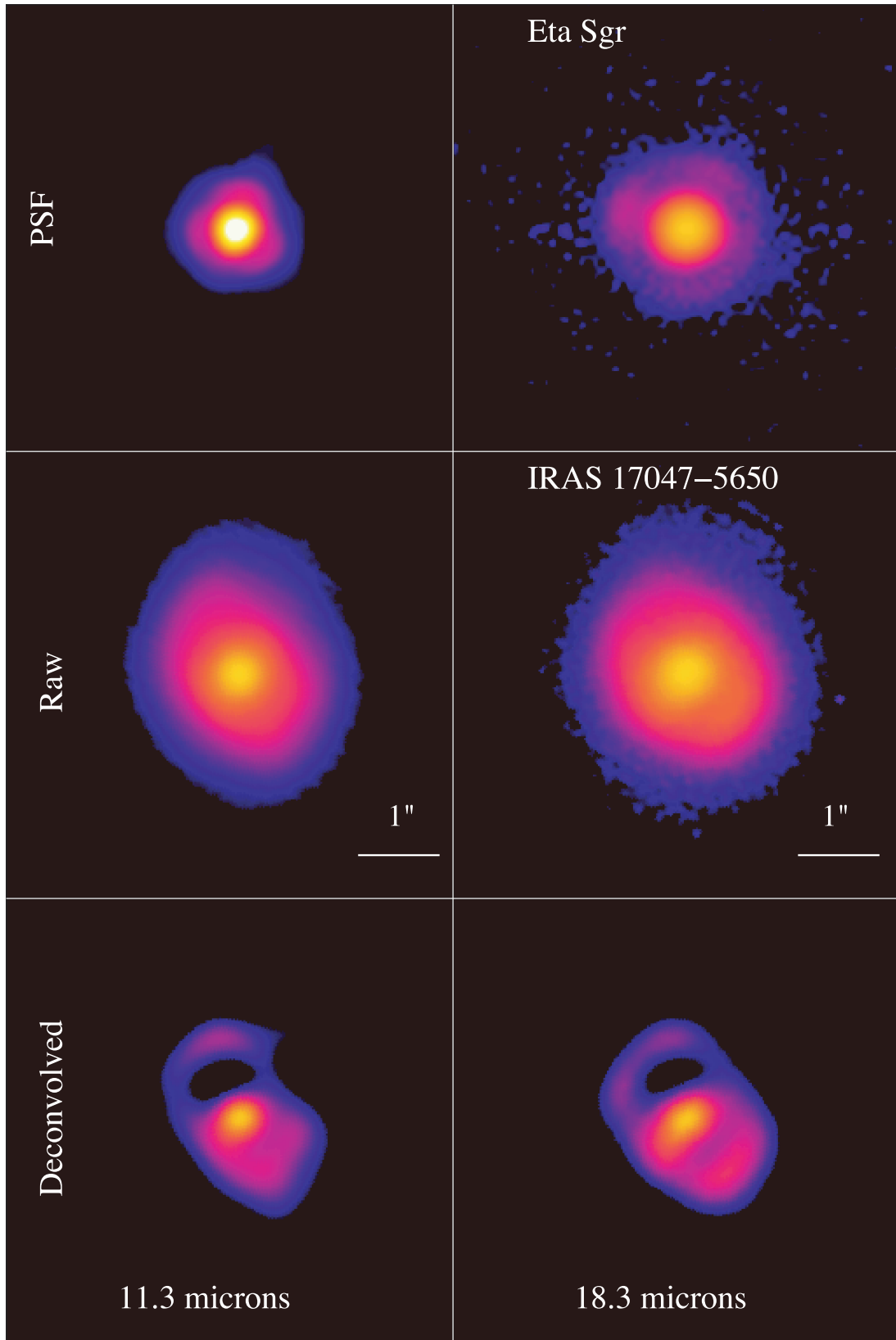


Figure B28. T-Recs/Gemini images of IRAS 17047 (CPD 56°8032).

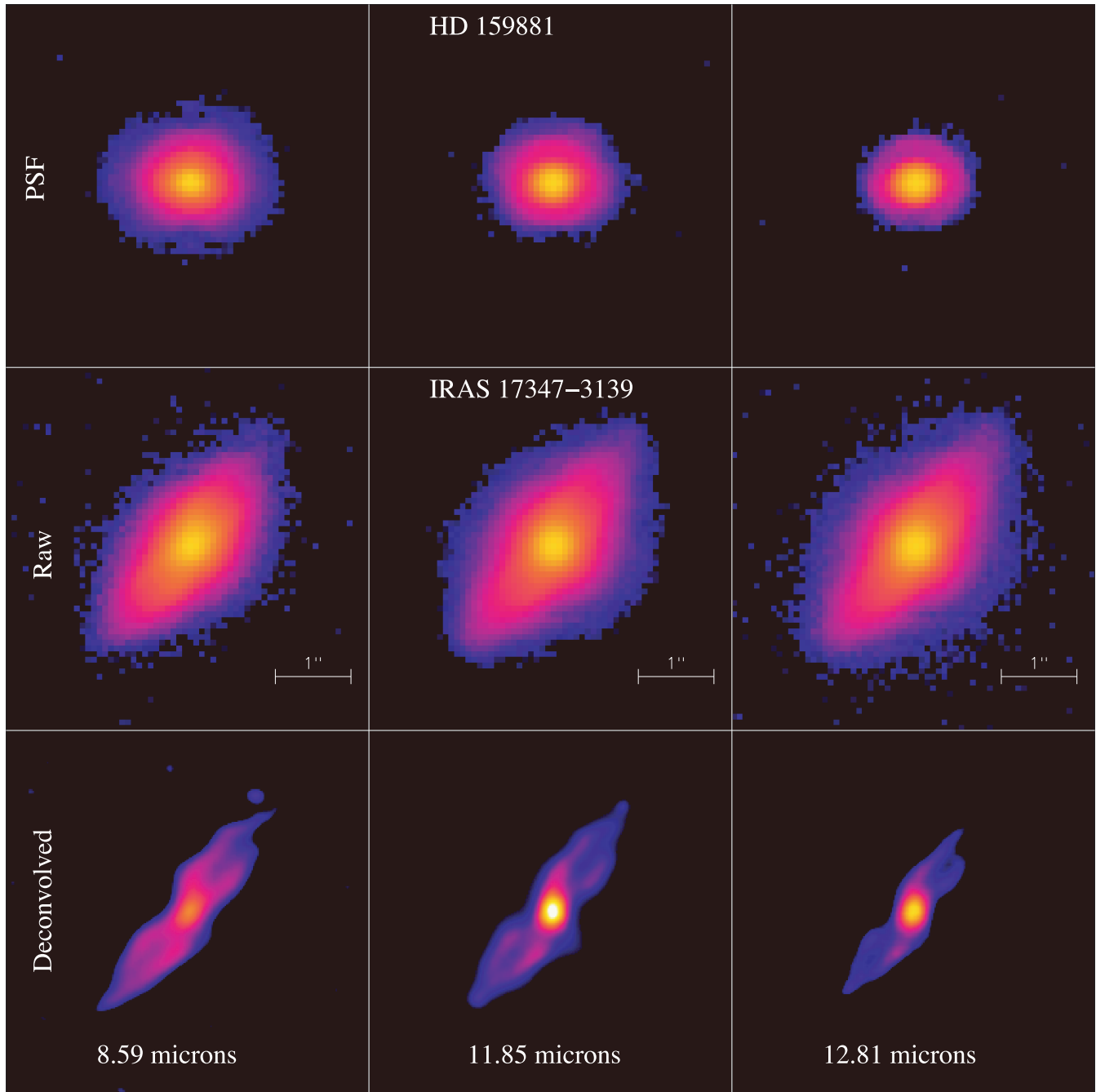


Figure B29. VISIR images of IRAS 17347.

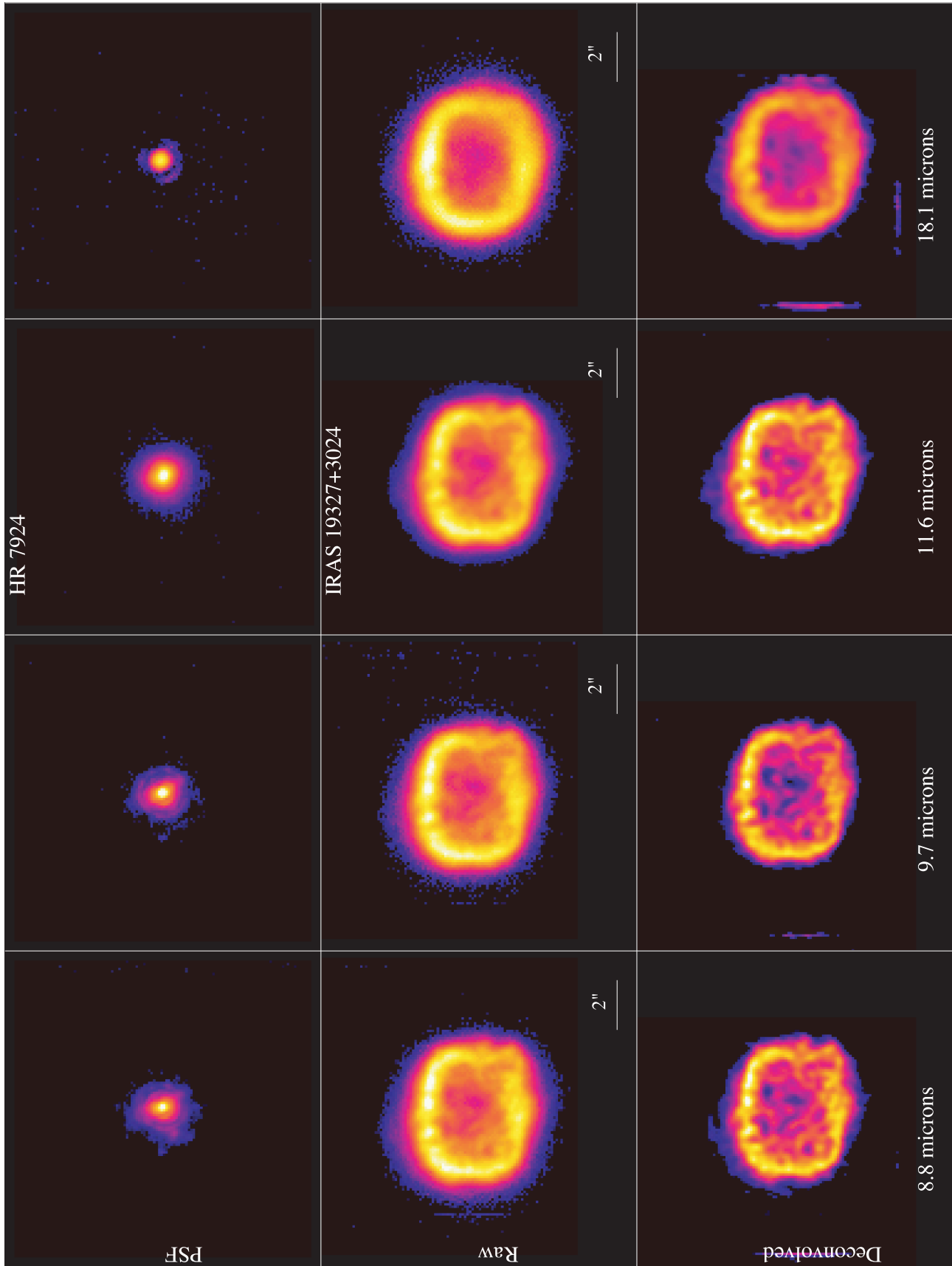


Figure B30. T-Recs/Gemini-South images of IRAS 19327 (BD+30° 3639).

Downloaded from <https://academic.oup.com/mnras/article/417/1/32/978996> by CNRS - ISTO user on 30 November 2021

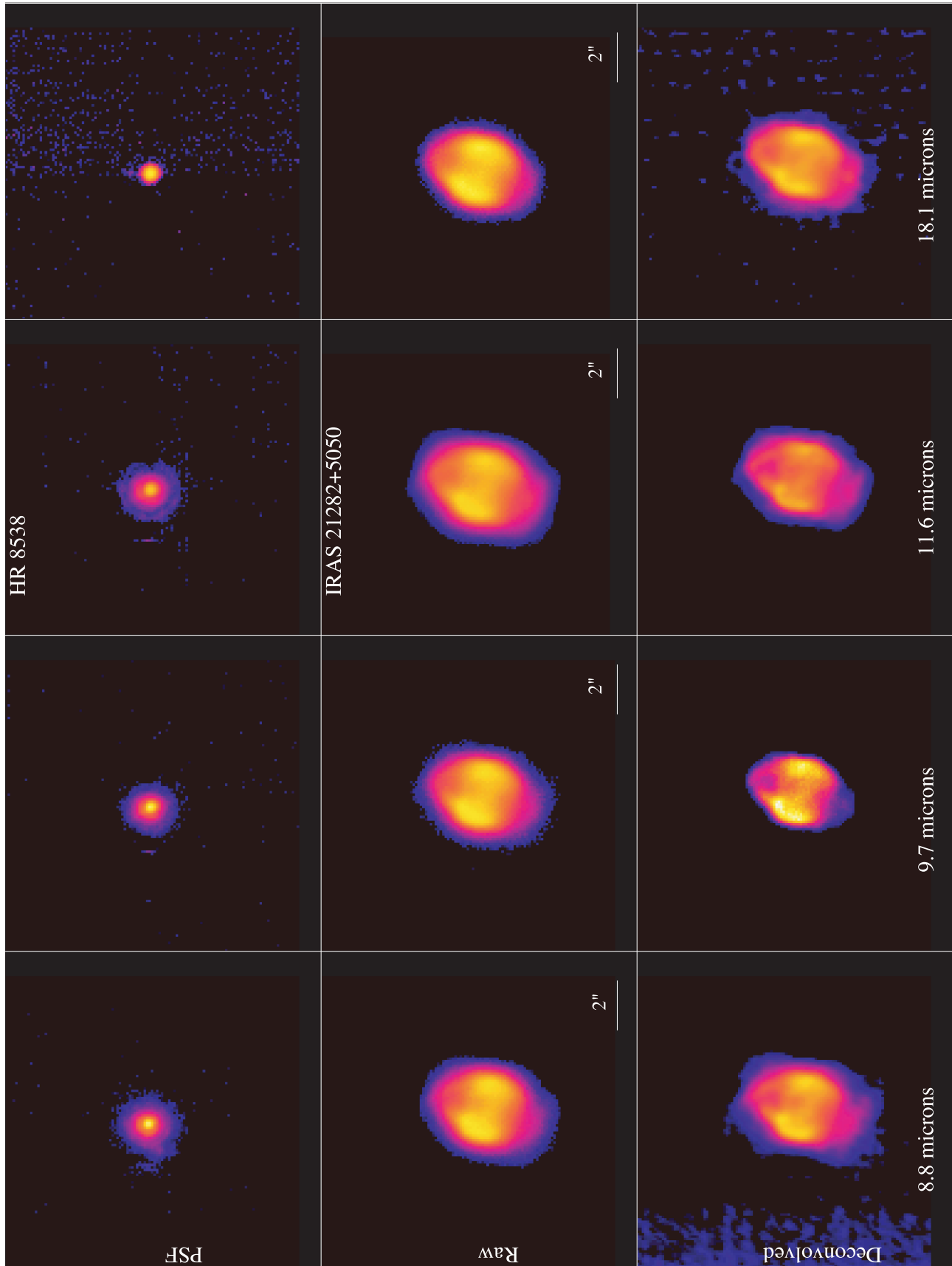


Figure B31. Michelle/Gemini-North burst mode images of IRAS 21282.

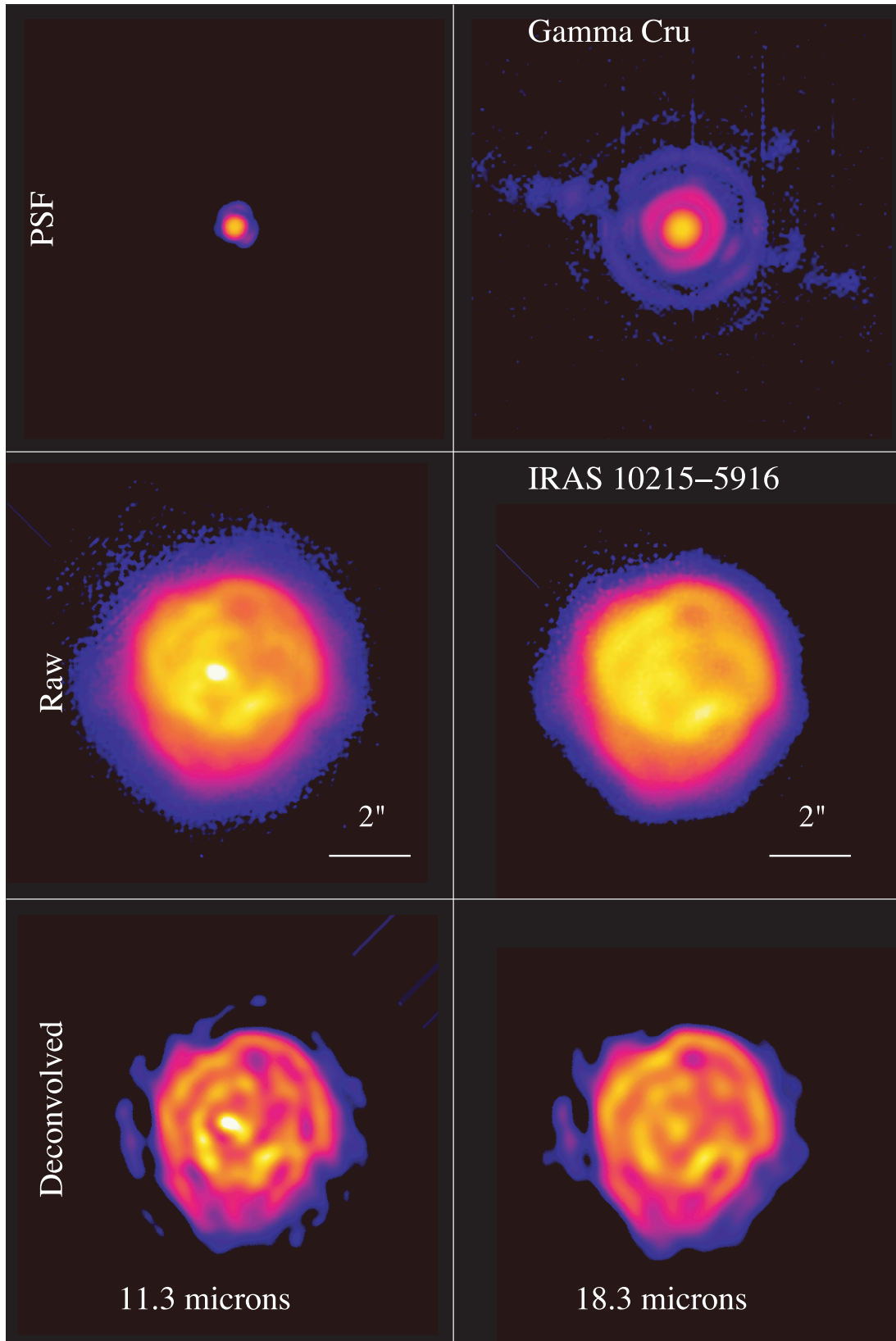


Figure B32. T-Recs mode images of IRAS 10215 (AFGL 4106).

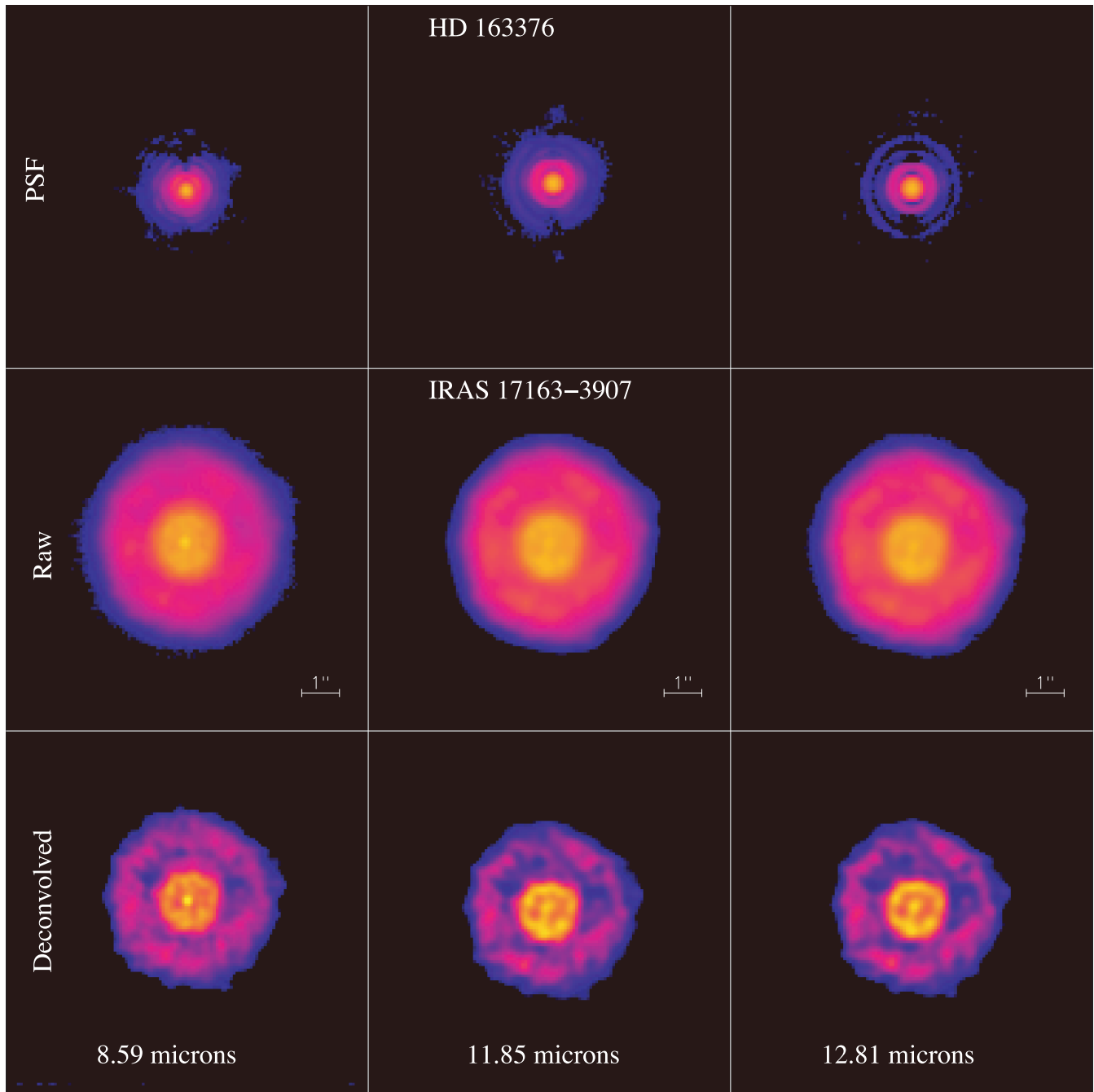


Figure B33. VISIR burst mode images of IRAS 17163.

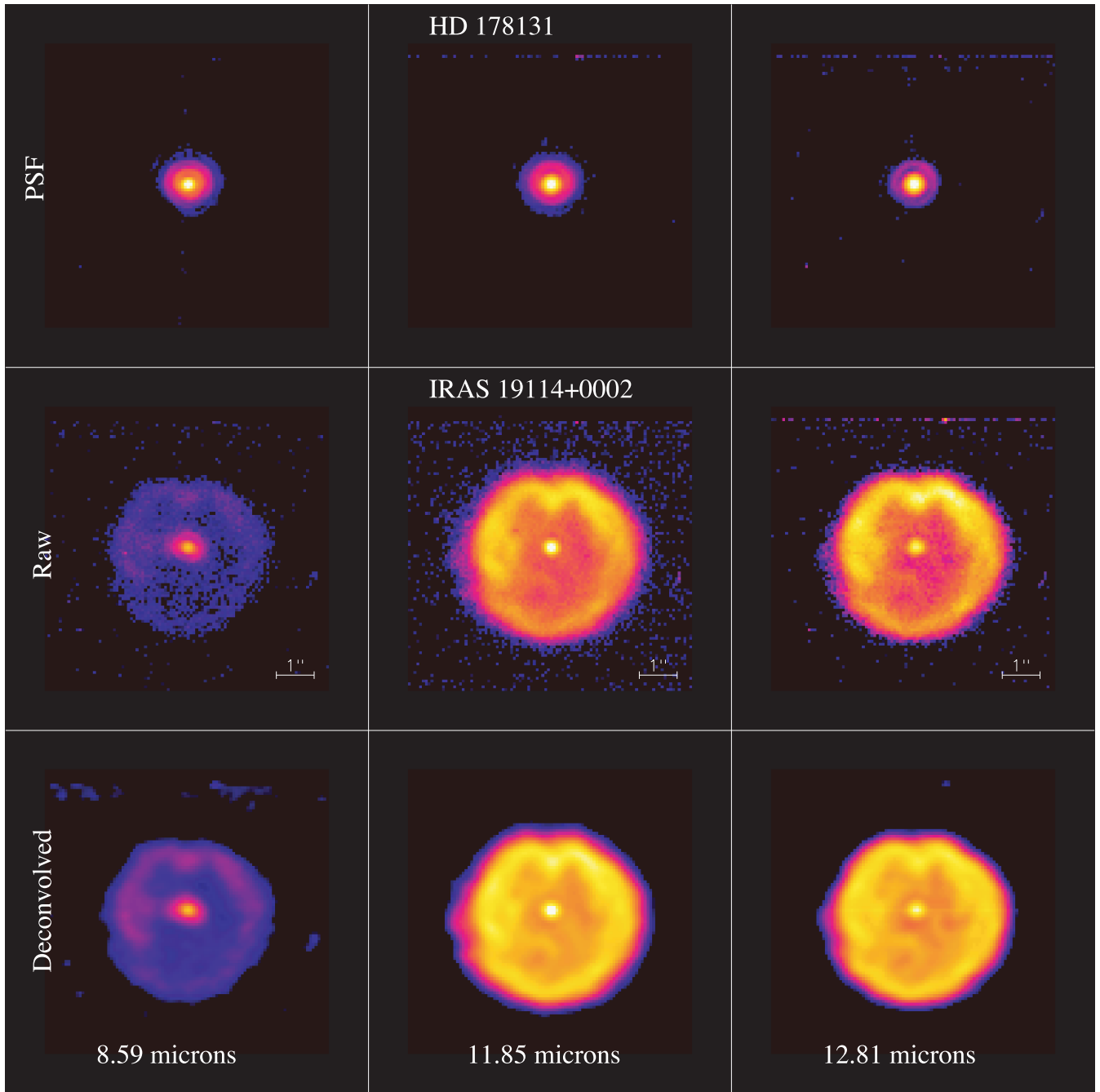


Figure B34. VISIR images of IRAS 19114.

Downloaded from <https://academic.oup.com/mnras/article/417/1/32/978996> by CNRS - ISTO user on 30 November 2021

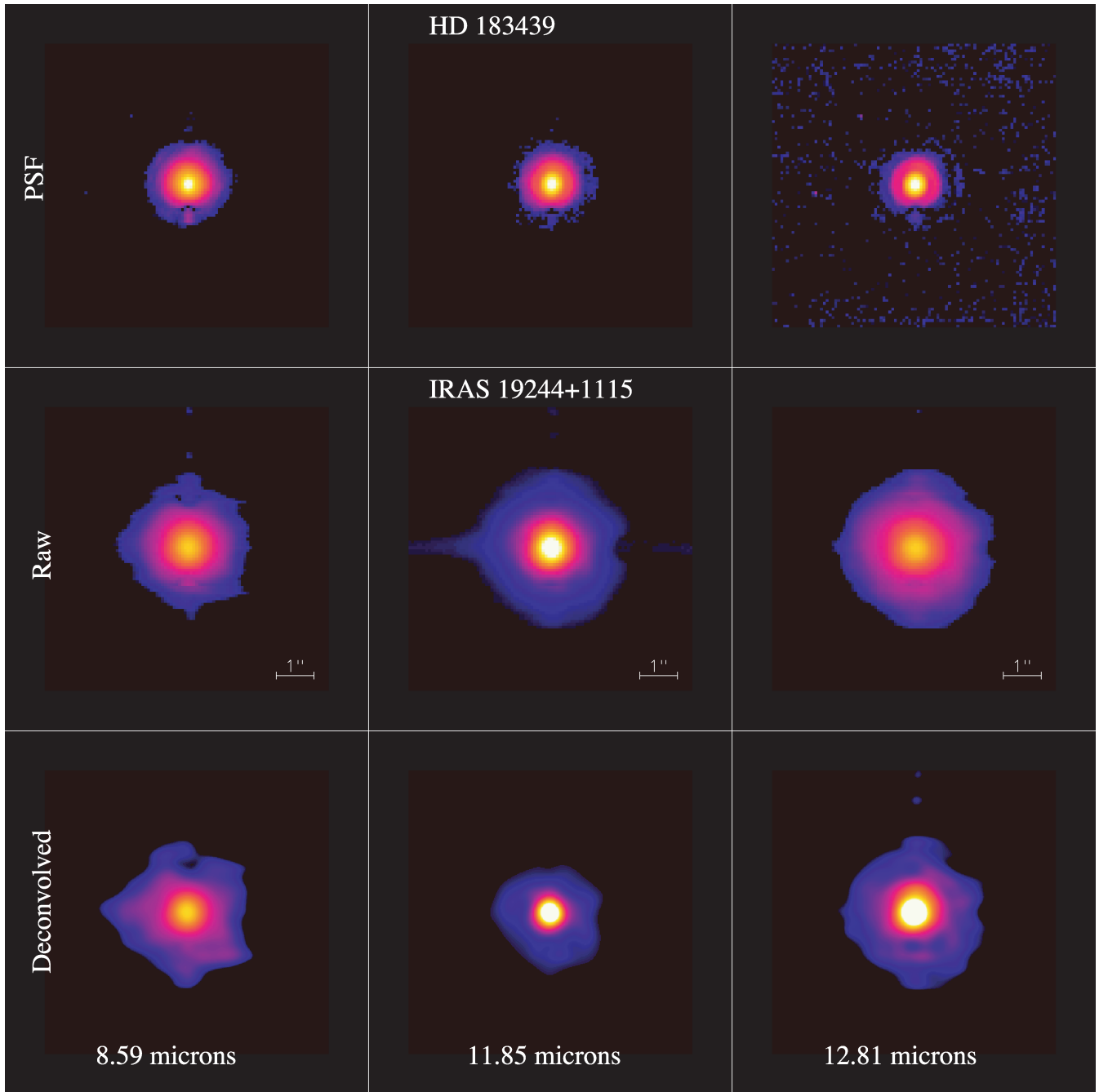


Figure B35. VISIR burst mode images of IRAS 19244 (IRC+10420).

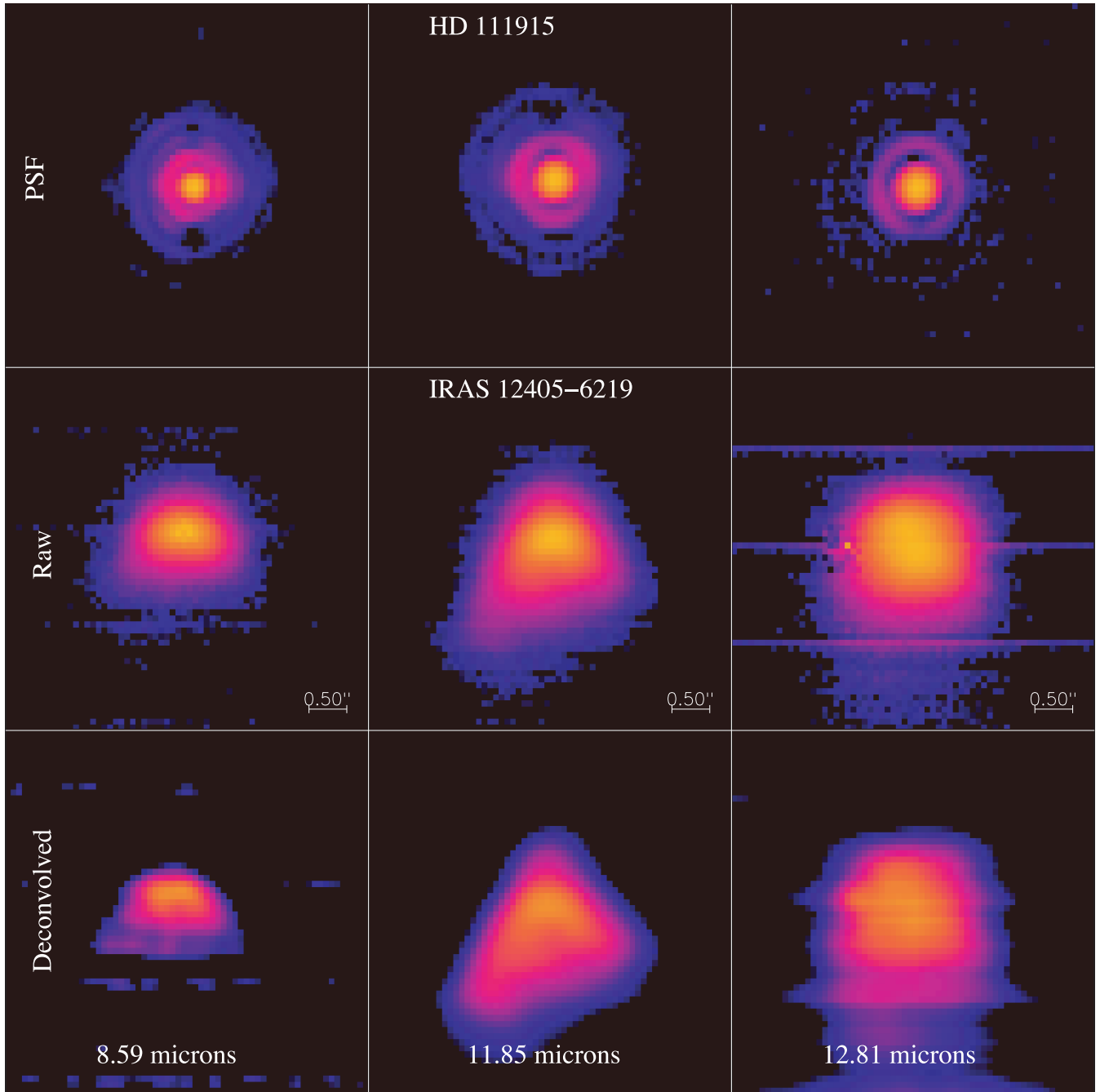


Figure B36. VISIR burst mode images of IRAS 12405.

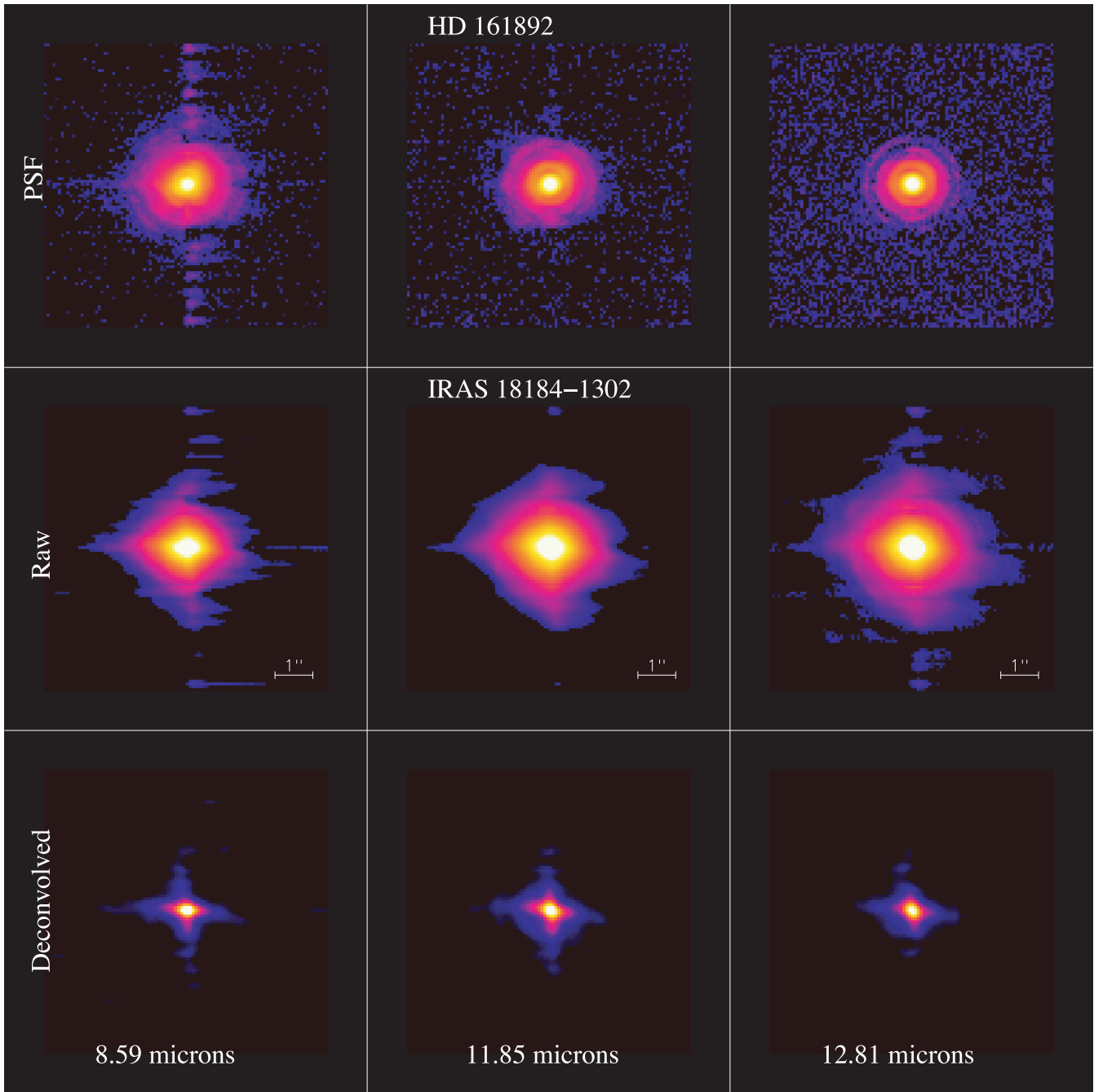


Figure B37. VISIR images of IRAS 18184 (the Red Square nebula).

This paper has been typeset from a $\text{\TeX}/\text{\LaTeX}$ file prepared by the author.